STUDY OF PASSIVATION BEHAVIOR FOR TITANIUM ALUMINIDES

Wei Su

B.S. Beijing University of Science and Technology, 1991

A thesis presented to the faculty of the
Oregon Graduate Institute of Science and Technology
in partial fulfillment of the
requirements for the degree
Doctor of Philosophy
in
Materials Science and Engineering

June 1998

The dissertation "Study of Passivation Behavior for Titanium Aluminides" by Wei Su has been examined and approved by the following Examination Committee:

Margaret Ziomek-Moroz, Thesis Advisor
Associate Professor
Department of Materials Science and Engineering
Oregon Graduate Institute of Science and Technology

William E. Wood
Professor
Department of Materials Science and Engineering
Oregon Graduate Institute of Science and Technology

Lemmy L. Meekisho
Associate Professor
Department of Materials Science and Engineering
Oregon Graduate Institute of Science and Technology

Dr. Jeffrey A. Hawk
Albany Research Center
Department of Energy

Dr. David E. Alman
Albany Research Center
Department of Energy

ACKNOWLEDGMENTS

First of all, I would like to thank my thesis advisor, Dr. Ziomek-Moroz, for providing financial support, and her guidance during the course of this research.

I am also very grateful to Dr. Jeffrey Hawk, Dr. David Alman, Dr. Steve Cramer, Mr. Covino, and Ms. Bullard, from Albany Research Center, Department of Energy for providing the titanium aluminides used in this study, and for providing access to the instruments for the X-ray Photoelectron Spectroscopy (XPS) and Electrochemical Impedance Spectroscopy (EIS) experiments, and their very helpful suggestions.

To my other committee members, Dr. Bill Wood, Dr. Lemmy Meekisho from Materials Science and Engineering Department at OGI, for their time and effort in reviewing the manuscript. Also thanks to my friends in Materials Science and Engineering Department at OGI, Jim Van Winkle, Kristen Terry, Jinhong Yang, Leo Chen, Graham Tewksbury. Without them, my study at OGI would not be such a pleasant experience.

To National Science Foundation (NSF/DMR-9423294), and Tektronix Inc. for providing financial support during the course of this research.

Special thanks to my wife Shujing who make this world a much better place.

TABLE OF CONTENTS

LIST OF FIGURES

LIST OF TABLES

ABSTRACT

Study of Passivation Behavior for Titanium Aluminides

Wei Su

Supervising Professor: Margaret Ziomek-Moroz

The general corrosion behavior of titanium aluminides in acidic, neutral and alkaline solutions was investigated using electrochemical techniques. Results showed that titanium aluminides passivated in all experimental solutions. In solutions containing NO_3^- ions, titanium aluminides showed susceptibility to pitting corrosion. The pitting potential increased as Ti content increases in the investigated intermetallics.

Passive film formation and dissolution behavior of titanium aluminides were studied using electrochemical and surface analysis techniques. The passive film dissolution rates were found to be pH dependent. The lowest dissolution rate was found in neutral solutions. In acidic solutions, the dissolution rate increased with the increase of Al content in the materials. In alkaline solutions, the dissolution rate was not sensitive to the solution pH. The results of X-ray Photoelectron Spectroscopy (XPS) showed that the compositions of the passive films formed on the surface of the investigated materials differed in acidic and alkaline solutions. In the acidic solutions, the ratios of Ti vs. Al in the passive films were similar to that of the bulk materials. In the alkaline solution, no detectable Al was present in the topmost layer of the passive films.

The electronic properties of passive films formed on titanium aluminides were examined using Electrochemical Impedance Spectroscopy (EIS). The passive films were found to have n-type semiconductor properties and the donor density of the passive films were calculated. It was found that the passive films on titanium aluminides had non-homogenous donor distribution. A modified Mott-Schottky relation was developed based on a linearly-graded donor distribution model.

Based on both the electrochemical measurements and surface analysis results, it was found that the passive behavior of titanium aluminides was closely related to their passive film composition and the semiconductor properties of the passive films. A modified point defect model was developed to explain the passivation behavior of titanium aluminides in acidic and alkaline solutions.

1. INTRODUCTION

Titanium aluminide based alloys have received much attention due to their excellent performance at high temperature and under severe environmental conditions. It appears that gamma titanium aluminide alloys will be the first of the titanium aluminide based intermetallics to see commercial service. Both GE Aircraft Engines and General Motors are testing the second generation of TiAl alloys in prototype applications[1].

The second generation of TiAl alloys is being considered for a variety of applications in both the civilian and military sectors. Among many parts under consideration are high and low pressure compressor blades, stator, vanes and cases, combustor components (diffuser case, swirler, etc.), nozzle components, flaps, outer skins, tubing, automobile turbocharger rotors, and exhaust valves[2,3]. GE Aircraft Engines is in the process of testing a number of the above-mentioned turbine components in actual engines and General Motors is road testing gamma TiAl exhaust valves[1].

Like other intermetallic materials, titanium aluminides get their superior mechanical properties by forming long-range ordered atomic structures. These structures cause difficulty in dislocation motion, thus provide the materials with attractive elevated temperature properties such as high strength, stiffness, and environmental resistance. However, the reduced mobility of dislocations also causes intermetallic materials to have adverse ambient temperature properties, such as poor ductility and fracture toughness. This results in limited applicability of conventional machining for these materials. To solve this problem and reduce the manufacturing costs, non-conventional machining methods are being investigated, such as electrochemical machining (ECM) and chemical milling (CHM)[1,4,5]. Electrochemical machining is the controlled removal of metal by anodic dissolution in an electrolytic cell in which the workpiece is the anode and the tool is the cathode[6]. During the ECM process, surface generation occurs with a very little or insignificant amount of mechanical interaction between the processing tool and the work-piece surface. Therefore, ECM can be successfully applied for shaping, finishing, and improving the quality of the surface for brittle materials, such as titanium aluminide-based alloys at ambient temperature.

During ECM, different anodic reactions may take place at high current densities depending on the metal-electrolyte combination and operating conditions. The rate of these reactions depends to a great extent on the ability of the system to remove the corrosion products as soon as they are formed. An understanding of the kinetics and stoichiometry of anodic reactions and their dependence on mass transport conditions is therefore essential in order to optimize relevant ECM parameters. According to the literature, titanium aluminides may form very protective passive films in aqueous solutions, which results in very low dissolution rates[7]. Such passive films may breakdown in solutions containing activating anions such as Cl^-, Br^- etc., resulting in pitting corrosion[8-11]. Therefore, the understanding of the passivation behavior of titanium aluminides is important for the development of an ECM process.

There are few literature data available on the corrosion behavior of titanium aluminides. Therefore, the objective of this research is to increase the understanding of the passivation behavior of titanium aluminides in different aqueous solutions such as H_2SO_4, NaOH and HNO_3, and establish a passivity model to describes their passivation mechanisms. Specimens used in this study include Ti_3Al, TiAl, $TiAl_3$, Ti_3Al+TiAl(minor), Ti_3Al(minor)+TiAl. Pure Ti and Al are also used as reference materials.

The investigation was focused on the factors that affect the dissolution rate of passive films, such as solution pH, applied potentials, electrolyte corrosivity, and passive film composition. A series of experiments were performed including electrochemical experiment and surface analysis. Potentiodynamic experiments were performed to determine the general corrosion behavior of the investigated materials. Passive regions were determined in the potentiodynamic experiments, which were used to select the potentials for potentiostatic experiments. The potentiostatic experiments were performed to determine the steady state dissolution rate of the passive films. These results give information about the protectiveness of the passive films. The passive films formed at the potentiostatic conditions were further examined using Electrochemical Impedance Spectroscopy (EIS) to study the electronic properties of the passive films. The donor densities of the passive films were calculated based on the Mott-Schottky relation[12]. The passive film compositions were measured by X-ray Photoelectron Spectroscopy (XPS). The oxidation states of different elements in the passive films were further analyzed using curve-fitting methods. Based on both the electrochemical measurements and surface analysis results, a model was developed to explain the passivation behavior of titanium aluminides in the investigated solutions.

2. LITERATURE REVIEW

2.1 Background

Titanium aluminide-based alloys are considered as future replacements for nickel-based superalloys due to their high strength-to-density ratios, good high temperature properties, and excellent resistance to corrosive environments[13]. Table 2-1[14,15] shows a comparison for the mechanical properties of titanium aluminide based-alloys with superalloys.

Titanium aluminides are intermetallic compounds, which can be defined as an ordered alloy phase formed by two or more metallic elements. By definition, an alloy phase is ordered if two or more sublattices are required to describe its atomic structure[14]. According to the binary Ti-Al phase diagram[16], there are intermetallic phases such as $Ti_3Al(\alpha_2)$, $TiAl(\gamma)$, $TiAl_2$, and $TiAl_3$, as well as α(Ti), β(Ti), and α(Al) terminal solid solutions[17] as shown in Figure 2-1. Figure 2-2 shows the crystal structures of Ti_3Al and TiAl as examples of ordered structures. Ti_3Al, called α_2, has an ordered hexagonal structure, whereas TiAl, called γ, has an ordered $L1_0$ structure.

Because there are few literature data for corrosion behavior of titanium aluminides, data for aluminum, titanium and titanium based alloys are used as references. According to the literature, excellent corrosion resistance of titanium based alloys results from the formation of a very stable, continuous, highly adherent, and protective oxide film on the metal surface[13]. Because titanium itself is highly reactive and has an extremely high affinity to oxygen, these oxide films form spontaneously after exposure to air or moisture. The nature, composition, and thickness of the protective surface oxides that form on titanium alloys depend on environmental conditions. TiO_2 is a typical product. Other oxides including Ti_2O_3 and TiO also exist[18]. High-temperature oxidation tends to promote the formation of the highly crystalline form of TiO_2 known as rutile which is chemically resistant. Lower temperatures often generate anatase which is a more amorphous form of TiO_2, or a mixture of rutile and anatase. These naturally formed films are typically less than 10nm thick[19]. TiO_2 is highly chemically resistant and is attacked by only a few substances, such as hot concentrated HCl, H_2SO_4, NaOH, and HF[13].

Titanium alloys may also be subjected to localized attack in tight crevices exposed to hot chloride, bromide, iodide, fluoride, or sulfate-containing solutions. In hot, very pure solutions or vapor condensates of nitric acid, significant uniform corrosion may occur. In 20-70 wt% HNO_3 solutions, semi-protective oxide films will form which do not fully retard continued oxidation of the metal surface[20]. Hydrofluoric acid solutions can aggressively attack titanium alloys over the full range of concentrations and temperatures. Additions of oxidizing species, such as HNO_3, tend to reduce corrosion and retard hydrogen uptake in HF solutions. For NaBr solutions, additions of various oxidizing anions may inhibit pitting by significantly raising anodic pitting potential. Critical concentrations of these inhibitive anions have been determined, and the relative efficiency of inhibition decreases in the order $SO_4^{2-} > NO_3^- > CrO_4^{2-} > PO_4^{3-} > CO_3^{2-}$. Titanium alloys are also very resistant to alkaline media, including solutions of NaOH, KOH, $Ca(OH)_2$, $Mg(OH)_2$, and NH_4OH[21].

Pure titanium exhibits a very high pitting potential due to its protective oxide film. The pitting potential of Ti may exceed +80V versus the saturated calomel electrode (SCE) in sulfate and phosphate solutions. In solutions containing chlorides, the typical pitting potential value ranges from +5 to +10 V[22]. The anodic pitting potential of titanium depends on alloy content, environment chemistry, temperature, potential scan rate and especially, surface condition.

The thermodynamic stability of titanium is illustrated in Figure 2-3. It is assumed that the oxide film consists of rutile TiO_2. As we can see, titanium could passivate in a large pH range[23].

According to the literature, the TiO_2 passive film behaves like an n-type semiconductor[24]. As an anode, very high resistance to anodic current flow through the passive oxide film can be expected in most aqueous solutions. The nature of the oxide films on titanium alloys basically remains unaltered in the presence of minor alloying constituents such as Fe[20].

Aluminum, another component of titanium aluminides, is also a thermodynamically reactive element. It shows good corrosion resistance by forming a stable oxide film on the surface. According to the Pourbaix diagram[23], aluminum is passive in the pH range of about 4 to 8.5. Beyond the limits of its passive range, aluminum corrodes in aqueous solutions. Its oxides are soluble in many acids and bases, yielding Al^{3+} ions in the former and AlO_2^- ions in the later[25]. The thermodynamic stability of aluminum is illustrated in Figure 2-4.

2.2 Formation and Dissolution of Passive Films for Ti-Based Alloys

The electrochemical behavior of TiAl, Ti_3Al, and $TiAl_3$ intermetallics in sulfate solutions is very similar to that of pure titanium[4,7,11]. In the presence of aggressive ions such as chloride, however, the intermetallics are susceptible to pitting corrosion and the pitting potential increases in the following order: $TiAl_3 < TiAl < Ti_3Al$[11]. The passive current increases with increasing scan rate[7,11]. Similar behavior has also been found for iron-aluminide intermetallic alloys[26].

Due to the similar electrochemical properties of titanium aluminides to that of titanium, data for titanium are used as references[4]. Electrochemical behavior of titanium has been widely studied. It exhibits typical passive behavior. The anodic oxide film on titanium consists mainly of TiO_2, which co-exists with the suboxides Ti_2O_3 and TiO close to the oxide/substrate interface[27,28].

The structure and composition of anodic oxides formed on Ti are strongly dependent on temperature and potential. In H_2SO_4 solutions, at temperatures higher than 333 K or at potentials more noble than 6V, film crystallization occurs. After the film crystallization, the film growth rate increases significantly. During the anodic film growth, the electric field within the film is of the order of 10^6 Vcm^{-1}[29]. This electric field yields high internal compressive stresses in the film.

The amount of bound water present in the film increases markedly above 343K, which plays an important role in stabilizing the passive film[30]. Also, it was found that all allotropes of TiO_2, i.e. rutile, anatase, and brookite could be present in boiling H_2SO_4, HCl and HNO_3[31]. For the anodic oxide films formed in H_2SO_4 and H_3PO_4, in the potential range of 0-100V, the anodizing ratio was estimated to be 2.5 nmV^{-1}[32].

The potentiostatic experiments performed in 0.5M H_2SO_4 for Ti show that during the early film growth stage, the current efficiency approaches unity, and the film growth follows a logarithmic rate law. Beyond this stage, the rate of the film dissolution becomes significant and increases with temperature. The film growth rate also increases with temperature[29].

In alkaline solutions, the thickness, inhomogeneity and porosity of open circuit film formation increase with the increase of solution concentrations. The chemical composition of the passive films revealed the presence of $Ti(OH)_3$ and $TiO_2.H_2O$[33]. Three reactions for the formation of passive film were suggested.

$Ti + 2H_2O \dashrightarrow TiO_2 + 4H^+ + 4e^-$ [2-2-1]

$Ti + 3OH^- \dashrightarrow Ti(OH)_3 + 3e^-$ [2-2-2]

$Ti(OH)_3 \Longleftrightarrow TiO_2 \cdot H_2O + 1/2H_2$ [2-2-3]

Reaction[2-2-1] is the dominant reaction for the film formation and repassivation[34]. Reaction [2-2-2] occurs on the sites where the natural oxide film dissolved, or due to migration of OH^- ions through the structural defects present in the thinnest parts of the existing oxide film. Following reaction [2-2-2], further transformation will lead to reaction [2-2-3]. By conversion of $Ti(OH)_3$ into $TiO_2 \cdot H_2O$, the surface film thickness grows and dynamic equilibrium is established between $Ti(OH)_3$ and $TiO_2 \cdot H_2O$. This equilibrium depends only upon the physical properties of the solution (concentration and temperature). The conversion of $Ti(OH)_3$ to $TiO_2 \cdot H_2O$ is closely related to the bonding number of OH^- ions[33].

Duin and Kolotyrkin proposed that the dissolution reaction of natural oxide film in 1M KOH solution was[33]:

$TiO_2 + OH^- = HTiO_3^-$ [2-2-4]

It has been confirmed that this dissolution reaction is possible only at the potential values more positive than -0.5 V(SCE) in dilute KOH solution. Also, the dissolution of TiO_2 occurs at potential values greater than -0.8 V(SCE) in concentrated KOH[33].

In acidic sulfate solutions, the anodic oxide film reductively dissolves into the solution as the Ti^{3+} ion according to reaction [2-2-5].

$TiO_2 + 4H^+ + e^- \dashrightarrow Ti^{3+} + 2\,H_2O$ [2-2-5]

Ohtsuka et al.[35] suggested that reaction [2-2-5] causes the thinning of the passive film in the cathodic reaction.

2.3 Segregation of Alloying Elements Into Passive Films

The literature data show that for intermetallic alloys, it is not unusual that one element in the alloy dominates the electrochemical behavior of the intermetallics[26,36,37].

This phenomenon is closely related to the segregation of alloying elements into the passive films.

Research on passivation behavior of Ni-xAl, Ni-xTi, and Ni-xMo alloys (x = 0.1-8 weight percent) shows that the alloying elements segregate into the inner barrier of the film in the following order: Al < Ti < Mo. This order appears to be related to the excess charge on the alloying element cation over the host cation. The extent of segregation decreases with increasing voltage of film formation potential, and the extent of segregation does not strongly depend on the composition of the binary alloy. The thickness of the film varies in the reverse order Mo < Ti < Al. This observed order in the film thickness is consistent with the notion that more protective films are thinner[36]. A similar behavior was also found for Ti-15Mo-3Nb-3Al β-titanium alloy in aqueous chloride solutions. Mo and Nb alloying additions are being incorporated into the oxide in amounts less than those found in the alloy[38].

Segregation of alloying elements into the passive film may change the electronic structure of a passive film. Kloppers et al.[39] reported that in the Fe-Cr system, segregation of Cr^{4+} and Cr^{6+} into the passive film acts as n-type doping. It decreases the number of oxygen vacancies in the Fe-Cr passive film, thus increasing the corrosion resistance of the materials.

2.4 Breakdown of Passive Films

The breakdown of passive films occurs in the presence of electrolyte anions, particularly aggressive anions such as halides. Three types of film breakdown may occur[40]: mechanical breakdown, electronic breakdown, and ionic breakdown.

The mechanical breakdown operates by introducing microscopic cracks into the film caused by large internal stresses associated with the film[41]. The electronic breakdown is caused by an electronic avalanche current[40], and presumably occurs within thick oxide films. For thin oxide films, ionic breakdown usually occurs. The ionic film breakdown starts with the competition for adsorption at the film/electrolyte interface between hydroxyl ions and aggressive anions such as chloride ions[40]. The ionic film breakdown in aqueous electrolytes is usually followed by either repassivation or local pitting dissolution at the breakdown sites.

Studies of the pitting behavior of titanium in 1N NaBr solution[42] show that the distribution of pitting potentials obeys a normal probability distribution with the maximum pit formation around 6.0V (SCE). The pit generation process occurs by the parallel birth and death process according to the stochastic model and depends on the film formation potential, i.e. the film thickness and properties. A similar study using scanning electrochemical microscopy (SECM)[43] also shows that: (1) The microscopic sites at which the breakdown occurs are electrochemically active. Therefore, the electrical conductivity of the oxide must be higher than that of the surrounding film; (2)The oxide breakdown potential increases with increasing average oxide film thickness. (3) The oxide breakdown occurs at significantly lower potential values in Br^- solutions ($E_P <= 5V_{SCE}$) than that in Cl^- solutions ($E_P \geq 10V_{SCE}$). The lower breakdown potentials in Br^- solutions indicate a strong chemical interaction between the TiO_2 surface and Br^-[43].

2.5 Models for Passivation Phenomenon

Passivation occurs when certain metals and alloys form very thin, oxidized, protective films on their surfaces in corrosive solutions[44]. The phenomenon of passivity has been investigated by researchers for over a century since Faraday originated the experiment in the 1840s[40,44]. The phenomenon is still difficult to define because of its complex nature and the specific conditions under which it occurs.

The literature show that the passive film can be either two-dimensional, about one monolayer thick, or three-dimensional, depending on the metal-solution system. Also, a transition from one to another may occur in the same metal/solution system, depending on the potential applied. For example, Frankenthal and Pickering found that passive films formed on iron surfaces at low potentials from passive region in borate buffered dilute NaOH, and yielded Fe_3O_4 or γ-Fe_2O_3 films less than a unit-cell thick[45,46]. At higher potentials, the film thickness exceeded the unit cell dimension for the ferric oxide, γ-Fe_2O_3, implying a three-dimensional film. In the following section, we will review several passivation models which might be used to explain the passivity of titanium aluminides.

Mott-Cabrera model: This model was proposed to explain kinetics of passive film growth. It was proposed by Mott in 1947 and was later extended by Cabrera and Mott in 1948 [47]. This model assumes:

(1) Film growth is due to the transport of metal cations across the oxide film to the film/solution interface where they react with the electrolyte.

(2) The penetration of cations through passive film is assisted by the high electric field strength which is assumed to exist within the oxide.
(3) The field strength is constant throughout the film.
(4) Total potential drop across the film is a constant and independent of film thickness.
(5) The rate-limiting step for film growth is the emission of metal cations from metal into the film at the metal/film interface.

These assumptions lead to the following rate law for film growth:

$$dL/dt = N\Omega v \exp\left[\frac{-W + qa\phi_f/2L}{kT}\right] \qquad [2\text{-}2\text{-}6]$$

where N is the number of mobile cations per unit surface area, Ω is the molecular volume per cation, γ is the vibration frequency, W is the activation energy for the rate-controlling step, q is the charge that the cation carries, a is the jump distance, and kT is the thermal energy. An approximate solution to equation [2-2-6] yields an inverse logarithmic rate law:

$$1/L = C - D\ln(t) \qquad [2\text{-}2\text{-}7]$$

where C and D are constants which depend on the material properties and electrolyte. The following requirements must be met for equation [2-2-7] to be valid:

(1) The film must grow under constant electric field rather than constant voltage.
(2) The oxide must rearrange with time so that the value of W also increases.

The first condition could be met when the increase in electric field across the oxide causes cation movement to occur through the oxide before the maximum value of voltage is attained. The second one implies that the kinetics of low-temperature oxidation depends on the structure of the oxide[48].

The inverse logarithmic growth law has also been observed for Fe in low pH solutions[49], where passive film dissolution is significant. The Mott-Cabrera model, however, does not take this phenomenon into consideration. Studies performed at the Chalk River Nuclear Laboratories using radioactive markers to identify mobile species in anodic films of Al, Nb, Ta, W, Zr, Hf, U, and Si. Their studies show that, for all the metals investigated , anion transportation is largely, if not exclusively, responsible for film growth[50]. This observation tends to discredit the Mott-Cabrera model, which assumes that metal cation diffusion is responsible for film growth.

Sato and Cohen's model[47,50]: Sato and Cohen studied the passivity of iron in the pH 8.4 borate buffer solution. They found that the relationship among external current i, the applied potential V_{app}, and the accumulated charge in the oxide film Q_T can be expressed by the following empirical equation:

$$i = k' \exp(mV_{app} - Q_T/n) \qquad [2\text{-}2\text{-}8]$$

where k', m, and n are constants. The authors suggested a "place-exchange" mechanism as shown in Figure 2-5. According to this model, a layer of oxygen is adsorbed onto the surface which then exchanges places, possibly by rotation, with underlying metal atoms. A second layer of oxygen is then adsorbed and the two M-O pairs rotate simultaneously. This process repeats and results in oxide film thickening. Under potentiostatic conditions, this mechanism results in the logarithmic law:

$$L = A + B\ln(t + t_0) \qquad [2\text{-}2\text{-}9]$$

where L is the film thickness; t is the time, t_0 is incubation time, and A, B are constants.

Fehlner and Mott's model[47,50]: The "place-exchange" mechanism proposed by Sato and Cohen does not provide a very convincing description of the growth of a film whose thickness is more than one of two monolayers. Therefore, Fehlner and Mott suggested an alternative mechanism. The modifications of Sato and Cohen's model involve the following assumptions:

(1) Anion diffusion is responsible for film growth.
(2) The rate-limiting step is the emission of an anion from the environment into the film at the film/environment interface.
(3) The field strength in the film does not depend upon the film thickness.
(4) The activation energy, W, of the rate-limiting step increases linearly with thickness.

Based on these new assumptions, Fehlner and Mott derived the following equation:

$$\frac{dL}{dt} = N\Omega\nu\exp\left[\frac{-W^0 - \mu L + {}^{qa\varepsilon}\!/_{2}}{kT}\right] \qquad [2\text{-}2\text{-}10]$$

where L is the film thickness, N is the number of mobile cations per unit surface area, Ω is the molecular volume per cation, ν is the vibration frequency, q is the charge that the cation carries, a is the jump distance, and kT is the thermal energy, W^0 and μ are constants.
This yields another logarithmic law :

$$L = A' + B'\ln(t + t_0) \qquad [2\text{-}2\text{-}11]$$

where t is the time, t_0 is incubation time, and A', B' are constants. Transient phenomena resulting from sudden changes of the applied potential or the pH of the solution were investigated[51]. The results show that the reaction [2-2-12] taking place at the film/solution interface, is established rapidly, and cannot be considered as a rate-limiting step. This observation contradicts the Fehlner-Mott model which assumes that the rate-limiting reaction occurs at the film/solution interface[50].

$$O(\text{oxide}) + 2H^+_{(aq)} + 2e^- = H_2O \qquad [2\text{-}2\text{-}12]$$

Point Defect Model: Macdonald et al. modeled the growth of the passive film in terms of diffusion of point defects(in a concentration gradient) and under the influence of the electric field[50,52-55]. Macdonald et al. raise two very important questions: (1) What are the point defects present in the passive films? (2) Which defect species are the mobile species?

Chao suggests that diffusion of metal vacancies contributes to corrosion only, while the diffusion of oxygen vacancies is associated with the growth of the passive film. Thus, the growth rate of the passive film is equal to the diffusion flux of oxygen vacancies in the electrochemical potential gradient that exists in the passive film. Therefore, the passive film is considered to be protective if it functions as a barrier against metal vacancy diffusion[39]. The point defect model will be further discussed in Chapter 5.

2.6 Semiconductor Properties of Passive Films

Thin anodic passive oxide films are generally not crystalline. They become partially crystalline as their thickness increases which is probably caused by internal compressive stresses created in the film during their growth[56]. In general, the presence of a crystalline structures in the passive film may impair the electronic properties and therefore, corrosion resistance of the passive film[40].

The electrochemical stability of passivated metals and alloys depends not only on the chemical property but also on the electronic property of the passive films. Therefore, not only the ion flux, but also the electron transport through a passive film can be rate determining factors. Hence, it is of great importance to determine the electronic properties of passive films[57].

According to the theory of semiconductor physics, electrons in semiconductors fall into two regions: the valence band or the conduction band. Figure 2-6 illustrates the energy gap between the conduction band and the valence band of a semiconductor. The energy difference between the two bands is called band gap energy(E_g). The introduction of defects to a perfect crystal may narrow the band gap. Figure 2-6 also illustrates the donor and acceptor states of such defects. If the defect contributes electrons to the conduction band, it is referred to as an n-type defect. If the defect accepts electrons from the valence band, it is called a p-type defect. Passive films can be either p-type or n-type depending on the predominant defect in the film[24].

Passive films are either insulators or semiconductors. Most of the passive oxide films behave as n-type semiconductors such as ZnO, TiO_2, TiN, Fe_2O_3[24]. Their donor concentration can vary from 10^{19} to $10^{21}cm^{-3}$[40,57]. There are also p-type semiconductors such as FeO, CuS, Cr_2O_3, MnO[24] and insulators such as Al_2O_3[40].

The metal/film/solution system develops a potential and electric charge distribution. Figure 2-7 illustrates the charge distribution and potential change across the film and the film/solution interface. The charge distribution in the film is called space-charge layer. Equilibrium at film/solution interface is attained through a redistribution of electrons and holes in the space-charge region of the film and solvated ions and dipoles in the electric double-layer region in the solution. This charge redistribution causes the energy bands to bend either up or down, depending on the prevailing sign of the Outer Helmholtz Plane (OHP). The electron energy (potential) inside the semiconductor film away from this bending is called the flatband potential E_{fb}[24]. This is the potential where electrons and holes are in equilibrium. The total capacitance of the film/solution system is the electrical series of space-charge capacitance and Helmholtz capacitance:

$$1/C = 1/C_{SC} + 1/C_H \qquad [2\text{-}2\text{-}13]$$

where C is the total capacitance, C_{SC} is the space-charge capacitance, and C_H is the Helmholtz capacitance. The Helmholtz capacitance is typically much greater than the space-charge capacitance, therefore, the space-charge capacitance can be approximated by the total capacitance.

Various techniques are used to investigate the semiconducting properties. Photoelectrochemical studies have allowed us to obtain the flatband potential E_{fb}, the band gap energy E_g, and the donor or acceptor concentrations of the passive oxide films grown on metals and alloys in different electrolytes. It appears that thin amorphous oxide films on metals differ in their electronic properties from the corresponding crystalline bulk oxides. In many cases the band gap energy of passive oxide films can deviate from that of bulk oxides by up to 10%[40].

Some other models are more sophisticated than a simple semiconductor model discussed above. A p-n junction model shown in Figure 2-8, assumes a bilayered structure consisting of an n-type semiconductor layer on the metal side and a p-type layer on the electrolyte side[58]. The p-n junction model further extends into a p-i-n (p-type - intrinsic - n-type) junction model which assumes a three-layered structure with an intrinsic semiconductor layer between an inner n-type layer and an outer p-type layer[59]. A chemiconductor model is similar to the p-i-n junction model. It assumed the presence of an insulating dielectric layer of stoichiometric oxide sandwiched between the semiconducting non-stoichiometric regions associated with excess metal ions or lower valent metal ions on the metal side and metal ion vacancies or high valent metal ions on the electrolyte side[60-63].

Experimentally, the most direct and most frequently used technique to measure capacitance values and, hence, characterize the electronic properties of the oxide is AC-impedance measurement. These measurements are performed at high frequencies which are sufficiently high to measure only electronic contributions and suppress ionic contributions. In the case of passive films, these capacitance measurements are usually performed in situ in the electrolyte in which they are formed. For example, the electrolyte is used as front contact to the layer of interest.

One question regarding the validity of the semiconductor model is that the doping concentration is so high (10^{20}-10^{21} cm^{-3})[57], whereas for conventional semiconductors, this doping level leads to degeneration[64]. In contrast to ideal semiconductors, the doping species in passive film are not fixed. For example, the natural passive film on iron can be described as either Fe_2O_3 heavily doped with Fe^{2+} or as partially oxidized Fe_3O_4. Also, unlike ideal semiconductors, the doping concentration in passive film depends on the passivation conditions i.e. potential[57].

Mott and Schottky developed an equation relating capacitance of the corrosion film to potential, assuming that the films were semiconductors. If semiconductivity is present, Mott-Schottky plot will give a straight line for the $1/C_{SC}^2$ versus V_m plot, where C_{SC} is the space-charge capacitance and V_m is the measurement potential[65]. The Mott-Schottky equation that relates the space-charge capacitance C_{SC} to the potential, V_m, is[24,65]:

$$\frac{1}{C_{SC}^2}=\frac{2}{e\cdot N_D\varepsilon\varepsilon_0}(V_m-V_{FB}-kT/e) \qquad [2\text{-}2\text{-}14]$$

where C_{SC} is space-charge capacitance, e is the charge of electron, ε_0 is the permittivity of the free space, ε is the dielectric constant, N_D is the donor density, V_m is the imposed potential, V_{FB} is the flatband potential, K is the Boltzman constant and T is the absolute temperature. De Gryse et al. further developed this concept and introduced the effect of the Helmholtz capacitance in the equation [2-2-14][12]. The new equation is:

$$\frac{1}{C^2}=\frac{1}{C_H^2}+\frac{2}{e\cdot N_D\varepsilon\varepsilon_0}(V_m-V_{FB}-kT/e) \qquad [2\text{-}2\text{-}15]$$

where C_H is the Helmholtz capacitance, C is the total capacitance. In many systems, such as NiO and TiO_2, a discrepancy between the predicted and observed Mott-Schottky slopes was reported[12,66,67]. Some authors claim that for TiO_2, the discrepancy comes from the requirement $C_{SC}<<C_H$ does not hold[66]. However, based on equation [2-2-14], De Gryse et al.[12] proposed that the nonlinearity of the Mott-Schottky plot is not attributable to the fact that the condition $C_{SC} << C_H$ is not fulfilled. Therefore, they suggested the alternative reason which is the nonhomogenous donor distribution.

Semiconductor properties of Ti passive film has been widely studied using different techniques. Leitner et al.[68] investigated titanium electrode using photoelectrochemical technique. They found that thick films have similar properties to bulk TiO_2 electrodes. Films of intermediate thickness show all features of crystalline semiconductors, however, quantum efficiencies are considerable lower and this suggests the existence of surface states which facilitate surface recombination processes. Thin films are found to be amorphous in character.

Van de Krol et al.[69] used electron-beam evaporation technique to obtain a smooth nanometer-scale films of anatase TiO_2 on indium-tin oxide substrates (ITO). They found that at the potential at which the depletion layer reaches the TiO_2/ITO interface, the Mott-Schottky plot changed abruptly. From the position of the change point, a dielectric constant of 55 is calculated for polycrystalline anatase. Since the dielectric constants for titanium aluminides can not be found in literature, in this paper, the value of pure titanium are used as an approximation in our later calculations.

Table 2-1. Comparison of Ti based alloys with super alloys[15,17,70]

Properties	Ti_3Al-base	TiAl-base	Superalloy
Density(gcm^{-3})	4.1-4.7	3.7-3.9	8.3
Yield strength(MPa)	700-990	400-650	800-1200
Creep limit (°C)	760	1000	1090
Oxidation limit (°C)	650	900	1090
Ductility@ HT	10-20	10-60	10-20
Ductility@ RT	2-10	1-4	3-5
Tensile Strength (MPa)	800-1140	450-800	1100-1300
Structure	$D0_{19}$	$L1_0$	fcc/$L1_2$

RT: Room temperature

HT: High temperature

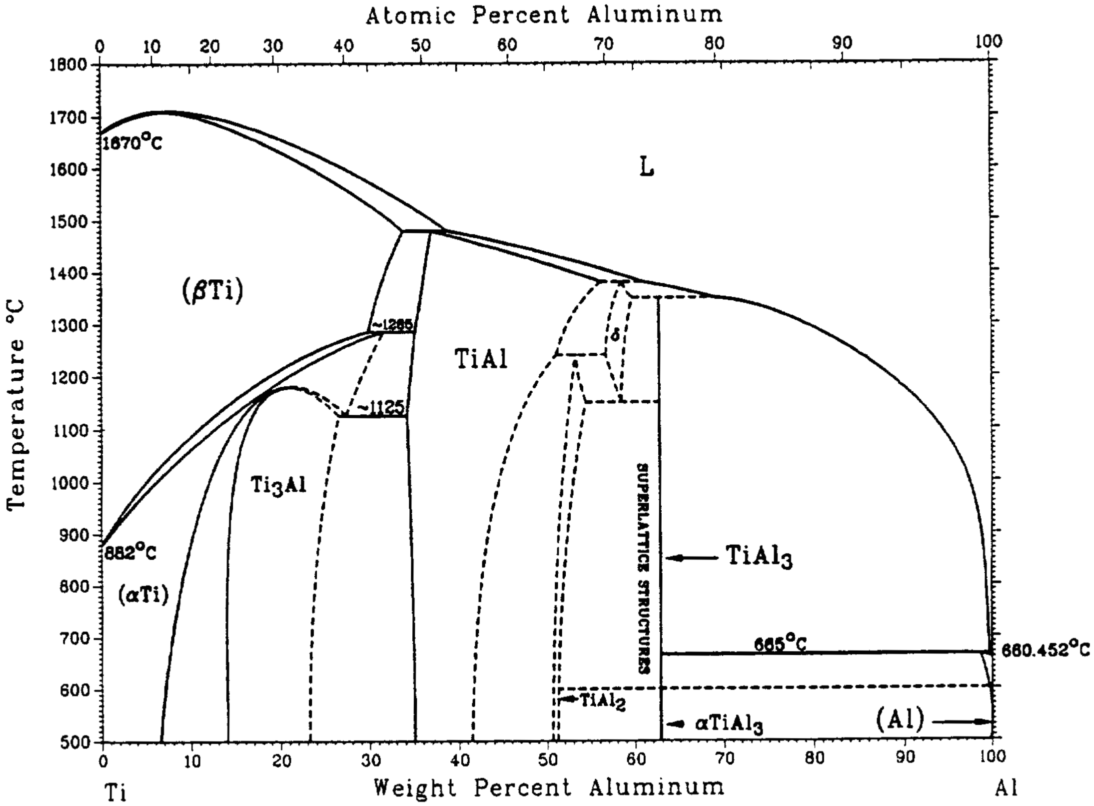

Figure 2-1. Binary alloy phase diagram for Ti-Al[16].
(Reprinted by permission, ASM International)

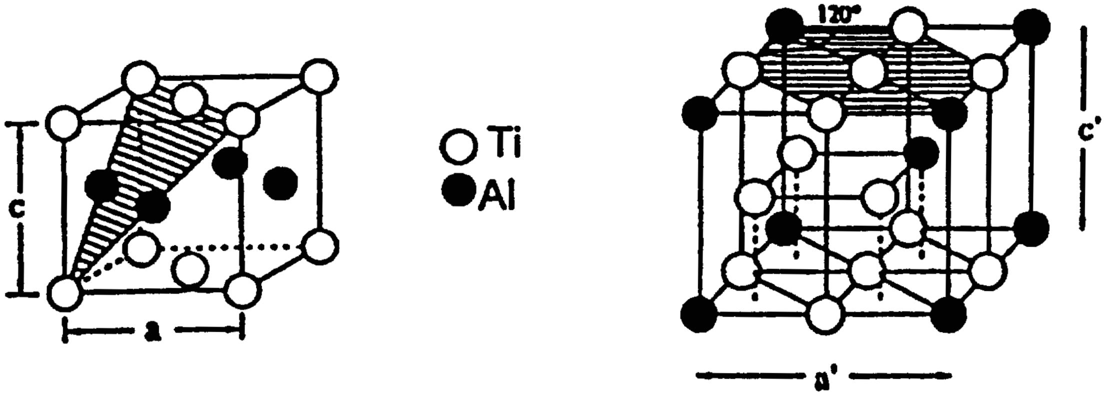

Figure 2-2. Crystallographic structures of (A) TiAl-γ and (B) Ti_3Al-α_2[17].

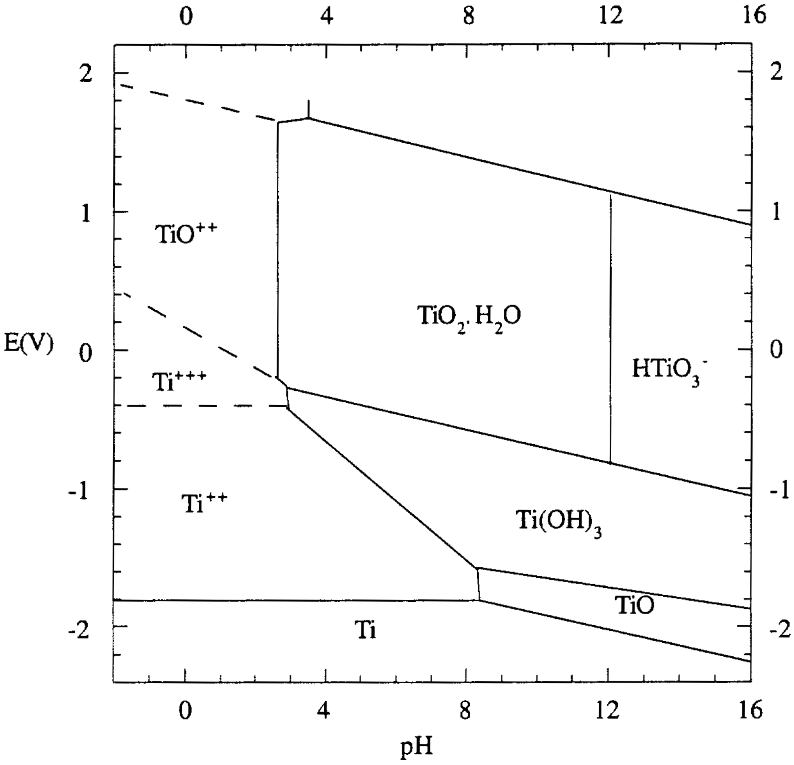

Figure 2-3. Potential - pH diagram for Ti.

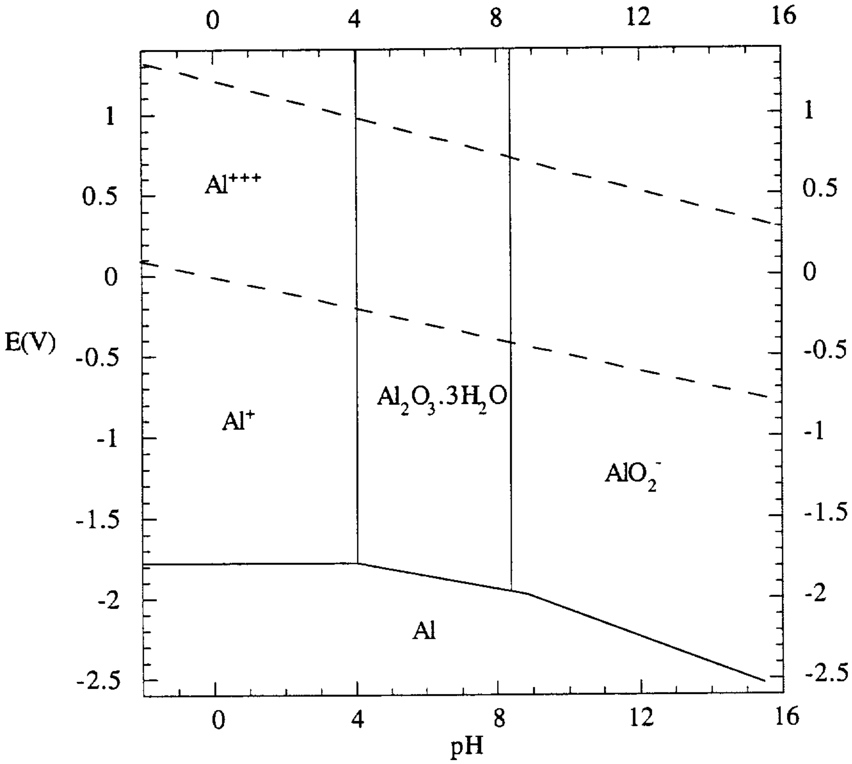

Figure 2-4. Potential - pH diagram for Al.

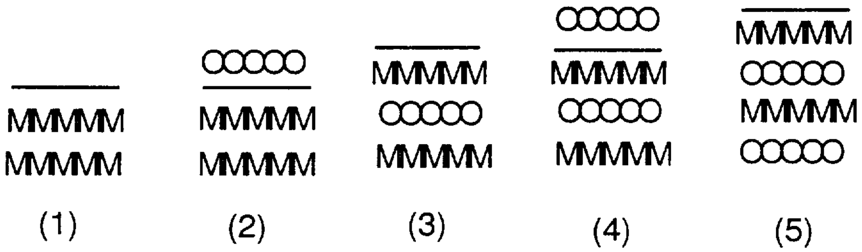

Figure 2-5. Oxide film growth by the place-exchange mechanism. M and O represent metal and oxygen atoms respectively.

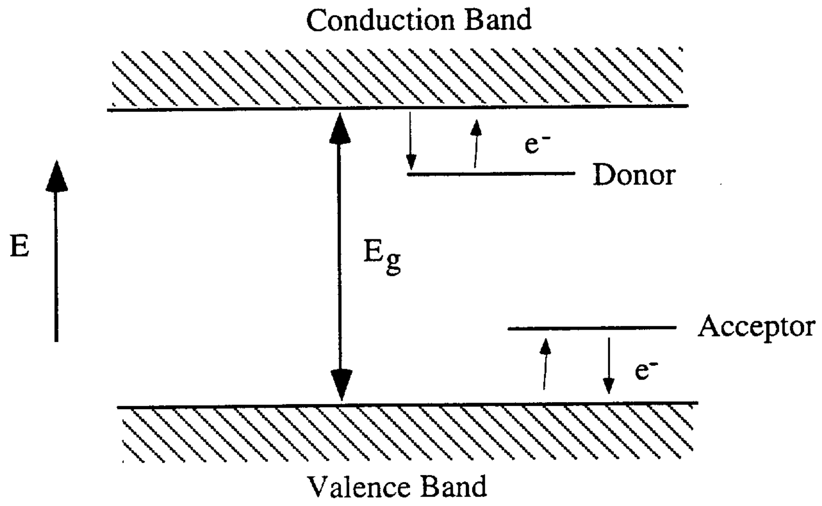

Figure 2-6. Illustration of band gap structure and electron transport across the band gap.

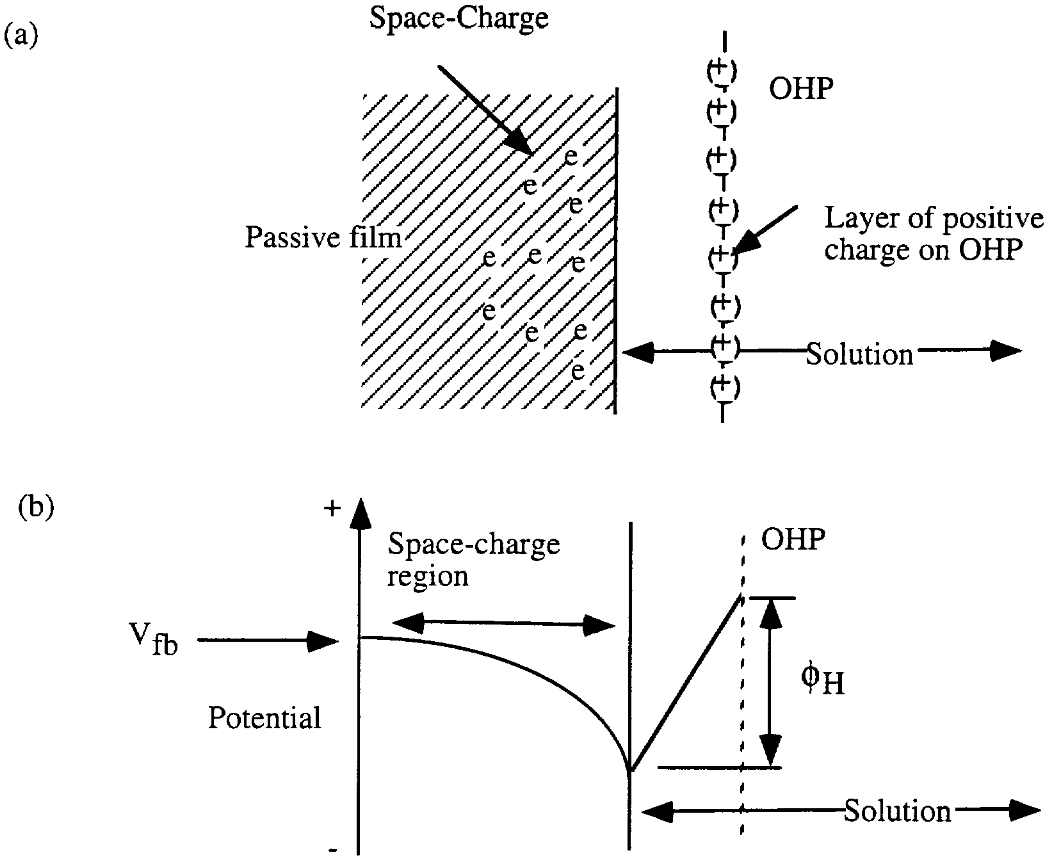

Figure 2-7. Illustration of the charge and potential distribution inside a semiconductor film. (a) space-charge region inside a semiconductor passive film, (b) the corresponding potential distribution, where V_{fb} is the flat band potential, OHP is the Outer Helmholtz Plane, ϕ_H is the potential drop over the Helmholtz layer.

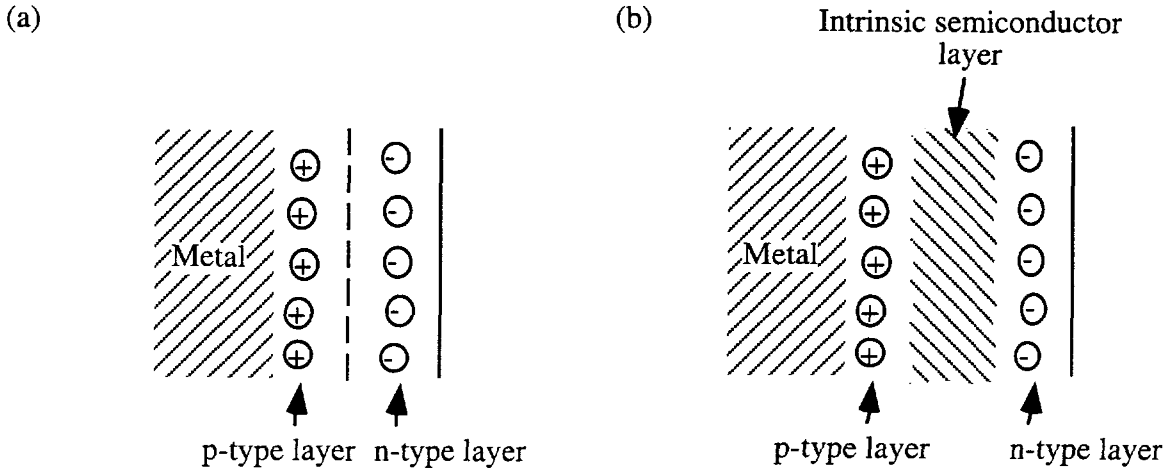

Figure 2-8. Semiconductor models for passive films.
(a) p-n junction model (b) p-i-n junction model.

3. EXPERIMENTAL PROCEDURE

3.1 Selection of Materials

The compositions of titanium aluminides selected for this study were based on the binary phase diagram for Ti-Al[16]. Titanium aluminides used in the experiments include $\alpha_2(Ti_3Al)$ and γ (TiAl), $TiAl_3$, and Ti_3Al+TiAl(minor phase), Ti_3Al(minor phase)+TiAl. Arc Melting (AM) was utilized in the preparation of all the specimens. $TiAl_3$ specimens were further treated by Hot Isostatic Pressing (HIP) to decrease the porosity. The HIP conditions were 1150°C and 25ksi for 2 hours. The density of the $TiAl_3$ specimens after HIPing was 3.30 gcm^{-3}. All specimens were then homogenized in vacuum at 1000°C for 24 hours to eliminate the minor phases and improve the porosity of the specimens. Pure titanium and pure aluminum were used in the electrochemical experiments for comparison. The composition of each specimen is shown in Table 3-1, where the subscript (m) stands for minor phase in the specimen.

Specimens used in the tests were cut into flat round disks approximately 1.0 cm in diameter. Electrical contact was made by spot welding a stainless steel wire to the back face of the specimens. The samples were mounted in epoxy resin such that only one surface was exposed to solution. For potentiostatic and potentiodynamic tests, before each test the specimen was wet polished from 240 to 600 grit SiC paper. For Electrochemical Impedance Spectroscopy (EIS) and X-ray Photoelectron Spectroscopy (XPS) experiments, each specimen was wet polished from 240 to 800 grit SiC paper.

Titanium aluminide specimens (except $TiAl_3$) were analyzed by X-ray diffraction (XRD) to identify crystalline phases. Phase analysis was performed using a Philips APD 3720 diffractometer system. The instrument was equipped with an automated goniometer, Cu X-ray tube, variable divergence slit, focusing graphite monochromator and scintillation counter. The results are summarized in Table 3-2. Examples of the optical micrograhps of some titanium aluminide samples are illustrated in Figure 3-1.

3.2 Selection of Electrolytes

Due to limited data available in the literature on the corrosion behavior of titanium aluminide alloys, an evaluation of the electrochemical behavior of pure titanium and aluminum is helpful. The Pourbaix diagram for titanium[71] shows that titanium passivates in the whole pH range (assuming passivation by the hydrated oxide TiO_2. H_2O)[27,32,33]. The Pourbaix diagram for aluminum[23] shows that aluminum corrodes at low and high pH. At pH close to neutral, aluminum passivates, and therefore, becomes corrosion-resistant.

Since one motivation for this research is the development of the electrochemical machining (ECM) process, the selection of electrolytes was, therefore, based on the requirements of the ECM. Electrolytes used in electrochemical machining must have high electrical conductivity, low toxicity and corrosivity, and a controllable passivating effect. It is reported that the presence of sulfate ions can have an inhibiting effect on the dissolution of aluminum. For different acids, the relative inhibition decreases in the following order: $SO_4^{2-} > NO_3^- > CrO_4^{2-} > PO_4^{3-} > CO_3^{2-}$ for Ti[13]. In hot, very pure solutions or vapor condensates of nitric acid, significant uniform corrosion rates may occur. In 20-70 wt% HNO_3 which are very aggressive, semi-protective oxide surface films will form that do not fully retard continued oxidation of the metal surface[13]. Based on these considerations, $2\underline{N}$ Na_2SO_4, $2\underline{N}$ H_2SO_4, $2\underline{N}$ $NaNO_3$ and $2\underline{N}$ HNO_3 were selected for this study. Also, $2\underline{N}$ NaOH and $2\underline{N}$ Na_2SO_4 + $2\underline{N}$ NaOH solutions were used to investigate the effect of pH as well as the effect of SO_4^{2-} ions on the dissolution of the passive films. The electrolytes used in the experiments were prepared by dissolving chemicals in deionized water.

3.3 Selection of Experimental Methods

Electrochemical and surface analysis techniques were used to investigate the electrochemical behavior of titanium aluminides and their passivity mechanisms: potentiodynamic experiments were performed to determine the general corrosion behavior of titanium aluminides; potentiostatic experiments were used to determine their dissolution rates at the steady state; electrochemical impedance spectroscopy (EIS) was used to investigate their semiconductor properties; X-ray photoelectron spectroscopy (XPS) was used to determine their passive film compositions.

3.3.1 Electrochemical Experiments

3.3.1.1 Potentiodynamic Experiments

An EG&G 273A Potentiostat/Galvanostat was used along with 352 SoftCorr II Corrosion Software for data collection. The reference electrode was a saturated calomel electrode (SCE), and the counter electrode was made of a Pt mesh. The solutions were deaerated with argon gas for about one hour before each experiment. For convenience, the potential values reported in this thesis are potentials measured vs. SCE by default. Electrochemical experiments were carried out at room temperature in a typical three-electrode cell. For potentiodynamic experiments, before each test, the specimen was cathodically polarized with a current of approximately $2 \cdot 10^{-8}$A for 2 minutes to remove as much of the air-formed passive film as possible. The specimen was immersed in the solution at open circuit for about half an hour to reach a relatively stable open-circuit potential. Potentiodynamic experiments were performed at a scan rate of 1.67 mVs^{-1} from -50 mV versus open circuit potential to 2.5V versus SCE in acidic solutions and to 2V in alkaline solutions.

3.3.1.2 Potentiostatic Experiments

The instruments and specimen preparation procedure for potentiostatic experiments are essentially the same as described in the potentiodynamic experiments. Each potentiostatic test lasted one hour at an applied potential of 1V in acidic solutions and neutral solutions. The applied potential was 0.2V for tests in alkaline solutions.

3.3.1.3 Electrochemical Impedance Spectroscopy (EIS)

A frequency response analyzer (Solartron/Schlumberger Model 1285) was used in the measurement of electrode impedance. The measurements were conducted by superimposing an AC voltage of 10mV amplitude with the frequency ranging from 0.02 to 15 kHz on a DC bias of a potentiostat. Impedance measurements were performed in

NaOH, H_2SO_4 and HNO_3 solutions for Ti, Ti_3Al and TiAl. The film formation potentials (V_f) were the same as used in the potentiostatic study: 1V for films formed in H_2SO_4 and HNO_3, and 0.2V for those formed in NaOH.

To evaluate the semiconductive property of the passive films, Mott-Schottky plots were derived with the impedance data obtained by the following procedure[65] as illustrated in Figure 3-2:

(1) The passive film was formed at a given film formation potential V_f for 3000s.
(2) The potential was lowered to a measurement potential $V_{m(i)}$, where the impedance was measured in the frequency range from 0.2 to 15k Hz within 80s.
(3) The potential was raised to V_f for 200s and lowered to $Vm_{(i+1)}$ where the impedance was measured.
(4) Step 3 was repeated to obtain the impedance at successively lower potentials.
(5) Steps 1-4 were repeated to obtain the impedance at successively higher film formation potentials.

In order to obtain the capacitance value of the space-charge layer in the passive film, a curve fitting method on the Bode diagram was employed using ZView™ software. Electrochemical Impedance Spectroscopy (EIS) data analysis was performed by first selecting an equivalent circuit model based upon a rational physical description of the phenomenon being probed as well as precedence for similar phenomena in the literature. For titanium and titanium aluminides, an equivalent circuit for the passive film is assumed consisting of a parallel RC circuit in series with a resistance R_S as shown in Figure 3-3, where C_f and R_f are the film capacitance and resistance and R_S is the electrolyte resistance. From the impedance diagrams obtained at various potentials V_m, the components of C and R can be estimated for the passive film formed at a certain potential V_f. Finally, from C^{-2} changing with V_m, one can obtain the Mott-Schottky plot for the passive film formed at various potentials V_f.

3.3.2 Surface Analysis: X-ray Photoelectron Spectroscopy (XPS)

Ti_3Al and TiAl specimens were passivated potentiostatically at 1V in H_2SO_4 and HNO_3, and 0.2V in NaOH for one hour respectively. Immediately after the anodic polarization, the specimens were rinsed with deionized water and dried with compressed argon. The specimens were then analyzed using a Surface Science Laboratory SSX-100 ESCA spectrometer using a 600µm analysis spot size. Argon ion sputter etching was used to incrementally remove material from the sample surface to produce a composition depth profile. The removal rate was based on the measurement of the removal rate for SiO_2. One survey scans were performed on each sample to determine the elements present and the binding energies to use for depth profiling. Areas selected for the depth profiles were different from those used for the survey scans. The concentration in atomic percentage for the i^{th} element, C_i, was determined using the formula:

$$C_i = \frac{A_i/S_i}{\sum_j A_j/S_j} \qquad [3\text{-}1]$$

and

$$S_i = SF_0\left(\frac{\mathrm{Al\ Kal,2}\ -\ BE_i}{\mathrm{Al\ Kal,2}\ -\ C_{1s}}\right)^X \qquad [3\text{-}2]$$

where A_i is the area under the i^{th} peak, S_i is the sensitivity factor, BE_i is the binding energy of the i^{th} peak, $Al\ Kal,2$ is equal to 1486.6 eV, C_{1s} is the binding energy of the Carbon 1s electron and x is an instrument determined parameter. All binding energies were referenced to the energy of the 1s photoelectron line for hydrocarbon which is 285.5 eV. Area and binding energies were determined from curve fit using a combined Gaussian-Lorentzian formula, and background subtraction by the Shirley method[72]. XPSpeak™ software was used for curve fitting to determine different oxidation states of Ti, Al and O for each specimen.

3.4 Summary

The solutions and specimens used in each experiment are summarized in Table 3-3.

Table 3-1. Compositions of specimens used in all experiments

Materials	Ti wt% (at%)	Al wt% (at%)
Ti	99.9	N/A
Ti_3Al	84.9 (76.0)	15.1 (24.0)
$Ti_3Al+TiAl_{(m)}$	74.8 (62.6)	25.2 (37.4)
$Ti_3Al_{(m)}+TiAl$	68.7 (55.3)	31.3 (44.7)
TiAl	65.5 (51.7)	34.5 (48.3)
$TiAl_3$	41.0 (28.1)	59.0 (71.9)
Al	N/A	99.9

Table 3-2. XRD determined phases for some titanium aluminide specimens

Materials	XRD Determined Phases
TiAl (15.1wt%Al)	Ti_3Al
Ti_3Al+TiAl (25.2wt%Al)	major phase Ti_3Al minor phase TiAl
Ti_3Al+TiAl (31.3wt%Al)	major phase TiAl minor phase Ti_3Al
TiAl (34.5%)	TiAl May contain trace amount of Ti_3Al

Table 3-3. Summary of solutions and specimens used for each experimental method

Experiment	Solutions	Materials
Potentiodynamic	H_2SO_4, Na_2SO_4, HNO_3, $NaNO_3$, NaOH, NaOH+Na_2SO_4	Ti, Al, Ti_3Al, TiAl, $TiAl_3$
Potentiostatic	H_2SO_4, Na_2SO_4, HNO_3, $NaNO_3$, NaOH, NaOH+Na_2SO_4	Ti, Al, Ti_3Al, TiAl, $TiAl_3$
EIS	H_2SO_4, HNO_3, NaOH	Ti, Ti_3Al, TiAl
XPS	H_2SO_4, HNO_3, NaOH	Ti_3Al, TiAl

XPS: X-ray Photoelectron Spectroscopy

EIS: Electrochemical Impedance Spectroscopy

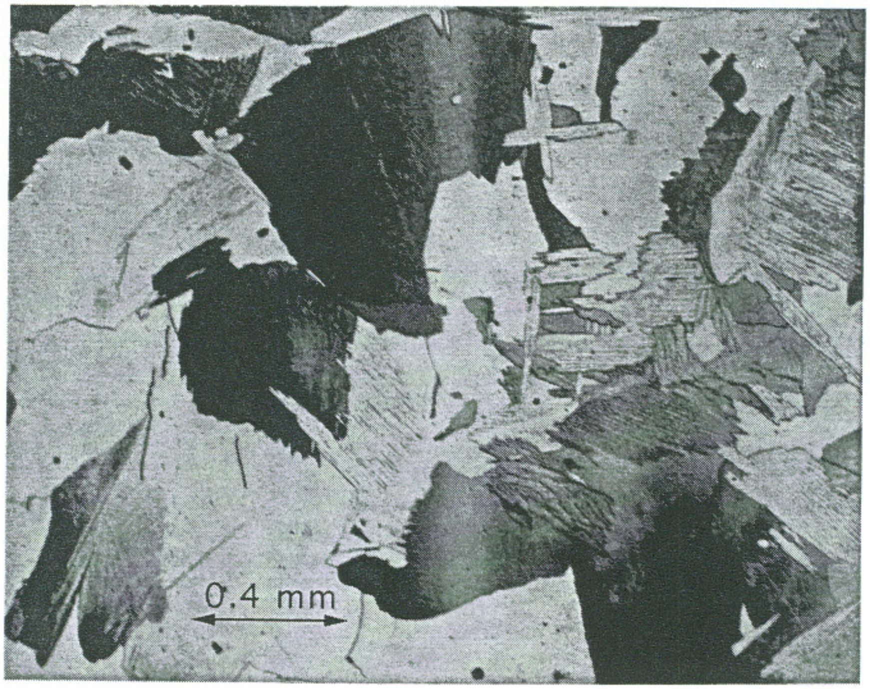

(a) Ti_3Al

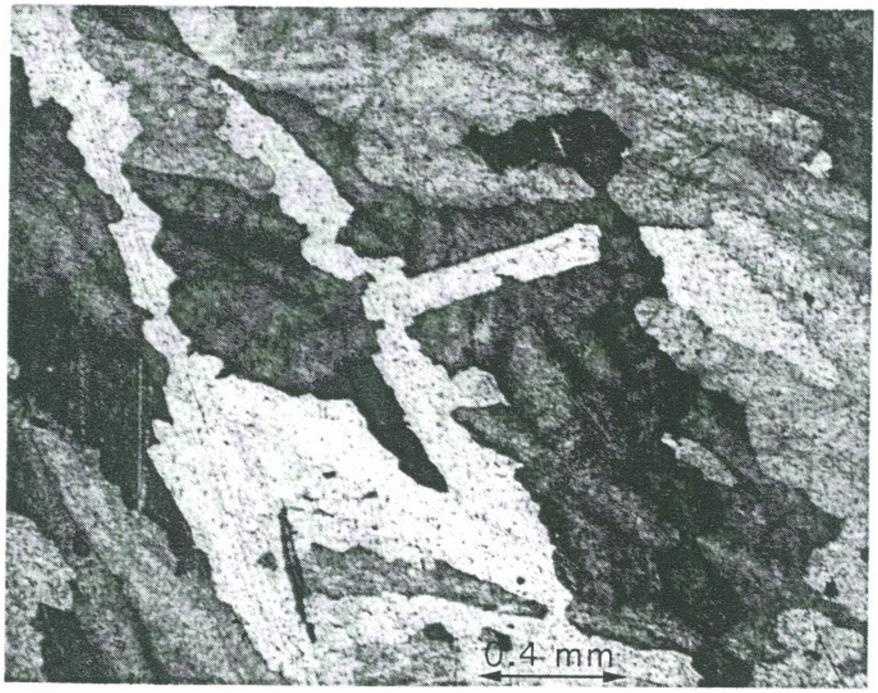

(b) TiAl

Figure 3-1. Optical micrographs of etched Ti_3Al and TiAl specimens.

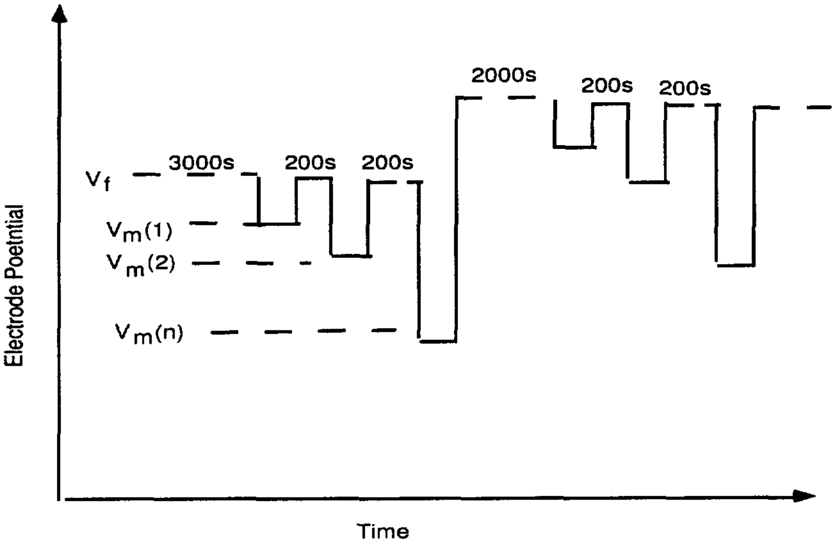

Figure 3-2. Potential-time diagram for the measurement of Mott-Schottky relation where V_f is film formation potential, V_m is measurement potential.

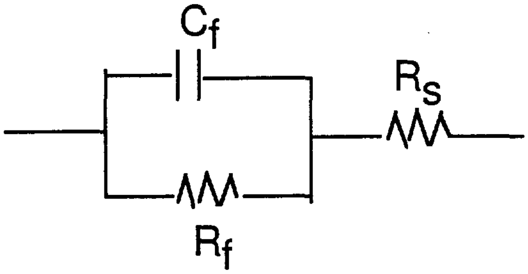

Figure 3-3. Equivalent circuit for passive films formed on titanium aluminides where C_f and R_f are the film capacitance and resistance and R_S is the electrolyte resistance.

4. RESULTS & ANALYSIS

4.1 Electrochemical Experiments

4.1.1 Potentiodynamic Experiments

4.1.1.1 Acidic solutions

Figure 4-1-1-1 shows the potentiodynamic polarization curves for Ti, Ti_3Al, TiAl, $Ti_3Al+TiAl_{(m)}$, $Ti_3Al_{(m)}+TiAl$, $TiAl_3$ and Al in H_2SO_4, where the subscript (m) stands for the minor phase in the specimen. All the titanium aluminide specimens show active, active-passive, and passive regions similar to titanium. The active-passive transition occurs at a potential range from -0.5 to -0.4 V_{SCE}. The passive regions are at potentials higher than about -0.3 V_{SCE}. The shape of the polarization curves for titanium aluminides is similar to that of pure titanium. They all show an activation current peak at around 1.7 V_{SCE}. This activation peak is typical for titanium which has been found by other researchers. According to Armstrong[73], the occurrence of the activation peak could be due to a phase transformation of the originally formed oxide film.

The highest current is observed for Al in the applied range of potentials. The minimum passive current densities of titanium and titanium aluminides increase with the increase of the aluminum content in the specimen as shown in Table 4-1-1-1. This indicates that Al affects the corrosion properties of titanium aluminides in H_2SO_4 solution.

Results of the potentiodynamic experiments in HNO_3 are shown in Figure 4-1-1-2. In HNO_3, all titanium aluminides show passive behavior. The transpassive behavior for Al, TiAl, $Ti_3Al+TiAl_{(m)}$ and $Ti_3Al_{(m)}+TiAl$ occurs at potentials around 1.7 V. After the experiments, round shaped pits were found on these specimen surfaces. An optical micrograph of the pits formed on TiAl is shown in Figure 4-1-1-3 as an example. For Ti and Ti_3Al, the specimen surfaces did not show any pit after the experiments.

The breakdown potentials for titanium aluminides decreases with the increase of the Al content as shown in Table 4-1-1-2. This is similar to the results in NaCl where Saffarian et al.[10,11] found the breakdown potential decreases in the order Ti_3Al > TiAl > $TiAl_3$. In both HNO_3 and H_2SO_4, the passive current density increases with the increase of Al content in the specimens.

4.1.1.2 Neutral Solutions

Figure 4-1-1-4 shows the results of the potentiodynamic experiments in Na_2SO_4. The shape of the polarization curves of titanium aluminides is similar to that of pure titanium. An activation peak is observed on the polarization curves for titanium and the intermetallics which begins to form at the potential of approximately 1.6 V. Since the shape of the polarization curves for the intermetallics is similar to that of titanium, the presence of these peaks can be associated with the transformation of the passive film as reported in the literature for titanium[73]. As shown in Table 4-1-1-3, titanium aluminides show lower minimum passive current densities than titanium. This is quite different from the results in acidic solutions where titanium aluminides show higher minimum passive current density than Ti in general. This result shows that pH of the solution can significantly affect the dissolution rate of titanium aluminides. The values of E_{corr} of the investigated intermetallics, as shown in Table 4-1-1-3, are also very similar to that of titanium.

Figure 4-1-1-4 shows the results of Ti, Ti_3Al, TiAl, $Ti_3Al+TiAl_{(m)}$, $Ti_3Al_{(m)}+TiAl$, $TiAl_3$ and Al in $NaNO_3$. Similar to the results obtained in HNO_3, none of the specimen shows active-passive transition. At potentials around 1.7 V, Al and all the intermetallics except Ti_3Al show great increase in current which is also accompanied with oxygen evolution. After the experiments, round shaped pits were found on these specimen surfaces. This indicates the specimens were attacked by pitting corrosion. Table 4-1-1-4 shows that the breakdown potentials of titanium aluminides decrease with the increase of the Al content in the specimen. Ti and Ti_3Al did not undergo pitting corrosion at this potential range. According to the literature, the breakdown potential of Ti in HNO_3 could be higher than 12V[74]. The minimum passive current density increases with the decrease of the Al content, which is very similar to the results obtained in Na_2SO_4.

4.1.1.3 Alkaline Solutions

The potentiodynamic polarization curves for Ti, Ti_3Al, TiAl, $Ti_3Al+TiAl_{(m)}$, $Ti_3Al_{(m)}+TiAl$, $TiAl_3$ and Al in NaOH are shown in Figure 4-1-1-6. The highest current density is found for Al. At potential around 0.6 V, Al reaches the transpassive state accompanied by oxygen evolution. After the experiment, pits were found on the specimen surface.

An activation peak is observed on the polarization curves for titanium and the intermetallics which begins to form at the potential of approximately 0.5V which can be associated with the transformation of the passive film[73]. Pits were not found for titanium and titanium aluminides in the applied potential range. For all the specimens, the corrosion potentials (E_{corr}) show similar values as shown in Table 4-1-1-5. For titanium and titanium aluminides, except $TiAl_3$, the critical passivation current density decreases with the increase of the Al content.

The potentiodynamic polarization curves for Ti, Al and the titanium aluminides in $NaOH+Na_2SO_4$ solution are shown in Figure 4-1-1-7. The results are summarized in Table 4-1-1-6. Al and $TiAl_3$ show much higher anodic current densities than Ti and the other intermetallics. The current densities for Ti and titanium aluminides, except $TiAl_3$, show very similar values. An activation peak is also observed on the polarization curves for titanium and the intermetallics. Pits were not found for titanium and titanium aluminides after the potentiodynamic experiments.

4.1.1.4 Summary of Potentiodynamic Experiments

The results of the potentiodynamic experiments indicate that titanium aluminides show very similar corrosion behavior to that of titanium. $TiAl_3$ also shows some similarity to Al which has relatively high anodic dissolution rate in all the solutions. In the NO_3^- containing solutions, titanium aluminides are susceptible to pitting corrosion. The breakdown potential increases with the increase of Al content in the specimen. For Ti and Ti_3Al, pits were not observed after the potentiodynamic polarization in the applied potential ranges.

4.1.2 Potentiostatic Experiments

Potentiostatic experiments were performed to determine the dissolution rate of titanium aluminides at the steady state. In H_2SO_4, as shown in Figure 4-1-2-1, the anodic current of Ti decayed to a very low value of the order of a few μAcm^{-2}, after one hour of polarization. Because the current continues to drop with time, a real steady state for titanium is difficult to attain. Shibata et al.[29] demonstrated that the rate of passive film growth after 1 hour was approximately equal to the rate of the film dissolution. Therefore, a steady state on titanium can be considered to be attained after one hour. According to literature, the charge consumed for passive film formation can be expressed as[29,47]:

$$Q_f = A + B \log (t+t_0) \qquad [4\text{-}1\text{-}2\text{-}1]$$

where Q_f is the charge consumed for the passive film formation, A and B are constants, t is the time, and t_0 is the incubation time. By differentiating equation [4-1-2-1], we can derive:

$$i = B/(t+t_0) \qquad [4\text{-}1\text{-}2\text{-}2]$$

where i is the passive current density caused by the passive film formation. Equation [4-1-2-1] and equation [4-1-2-2] assume that the passive film dissolution is negligible[29,50]. When the passive film dissolution is considered, the passive film formation process should be in equilibrium with the film dissolution process at the steady state. Therefore, the passive current density at the steady state can be determined from the film dissolution rate[50,54]. According to Macdonald et al.[50,52,53,75], the film dissolution rate is a constant value at the steady state. Therefore, adding a dissolution current into equation [4-1-2-2], a new equation obtained:

$$i = B/(t+t_0) + i_d \qquad [4\text{-}1\text{-}2\text{-}3]$$

where i_d is the current density associated with the film dissolution at the steady state.

In the following sections, for each potentiostatic curve, the *time* and *current density* are reported in log scale. The results are reported according to the solution pH: acidic, neutral and base solutions.

4.1.2.1 Acidic solutions

Figure 4-1-2-1 shows the results of the potentiostatic experiments for Ti, Ti_3Al, TiAl, $Ti_3Al+TiAl_{(m)}$, $Ti_3Al_{(m)}+TiAl$, $TiAl_3$ and Al obtained in H_2SO_4. Each curve can be divided into two parts. The first part shows a liner relation between log(current density) and log(time). The second part is curved and gradually approaches a constant value. The slopes of the linear part for titanium aluminides are very similar. However, none of the curves, except Ti, can be simulated based on the equation [4-1-2-3] because of their irregular shapes. For Ti, the curve can be fitted as:

$$i = 6.68e\text{-}7 + 7.95e\text{-}4 / (t - 0.38)^{0.914} \qquad [4\text{-}1\text{-}2\text{-}4]$$

where i is the current density (Acm^{-2}), t is the time (s). Equation [4-1-2-4] is very similar to equation [4-1-2-3] except that the power of $(t+t_0)$ is not a unit value. Such difference could result from many factors such as change in surface roughness of the electrode[76], or change in ion concentration at the film/solution interface[77].

As shown in Figure 4-1-2-1, the current densities approach steady values at the end of the experiments. This indicates that the steady state current density (SSCD) increases with the increase of the Al content in the materials which is in the following order:

$Ti < Ti_3Al < TiAl < Ti_3Al+TiAl(m) < Ti_3Al(m)+TiAl < TiAl_3 < Al$

The values of the SSCD are listed in Table 4-1-2-1.

The results of potentiostatic experiment obtained in HNO_3 are shown in Figure 4-1-2-2. Similar to the results obtained in H_2SO_4, each curve can be divided into the linear and the curved parts. Ti shows the longest linear region. The curve for all specimens except Al can be described by a equation similar to equation [4-1-2-4]:

$$i = i_d + A/(t + t_0)^{\alpha} \qquad [4\text{-}1\text{-}2\text{-}5]$$

where i is the current density (Acm^{-2}), t is the time (s), t_0 is the incubation time, i_d is the current associated with the film dissolution at the steady state, α and A are constants. Each curve is fitted with equation [4-1-2-5], and the results are shown in Table 4-1-2-2.

As shown in Table 4-1-2-2, the values of α for Ti, $Ti_3Al+TiAl_{(m)}$, Ti_3Al and $Ti_3Al_{(m)}+TiAl$ are very close to the ideal value 1. For TiAl and $TiAl_3$, α is quite different from the ideal value. This could be associated with their high dissolution rate which results in the change in surface roughness of the electrode[76]. The values of SSCD obtained in HNO_3 are similar to values in H_2SO_4: the SSCD increases with the increase of Al content in the specimen.

4.1.2.2 Neutral Solutions

The results of potentiostatic experiments for Ti, Ti_3Al, TiAl, $Ti_3Al+TiAl_{(m)}$, $Ti_3Al_{(m)}+TiAl$, $TiAl_3$ and Al obtained in Na_2SO_4 are shown in Figure 4-1-2-3. The polarization curves for Al and $TiAl_3$ can be divided into the linear and the curved parts which fit very well with equation [4-1-2-5]. For the other titanium aluminides and pure titanium, there is only the linear region. Because the curves only show the linear region, the dissolution current can be neglected from equation [4-1-2-5], which results in equation:

$$i = A/(t + t_0)^{\alpha} \qquad [4\text{-}1\text{-}2\text{-}6]$$

where i is the current density (Acm^{-2}), t is the time (s), t_0 is the incubation time, α and A are constants. The curve-fitting results are shown in Table 4-1-2-3. For Ti and titanium aluminides, except $TiAl_3$, steady state was not reached at the end of the experiments where the current densities were below $10^{-6}Acm^{-2}$. This indicates that these specimens have much lower dissolution rates in Na_2SO_4 than in the acidic solutions. According to the literature, the steady state current density for Ti in solutions of pH 6.9, is below $10^{-8}Acm^{-2}$[76,78,79]. Therefore, the current values measured at the end of the one hour polarization could be much higher than the real steady state value. The α values range from 0.9 to 1.1 which are very close to the ideal value 1. This may also associated with the low dissolution rate of passive film at the steady state.

Figure 4-1-2-4 shows the results of potentiostatic experiments for Ti, Ti_3Al, TiAl, $Ti_3Al+TiAl_{(m)}$, $Ti_3Al_{(m)}+TiAl$, $TiAl_3$ and Al obtained in $NaNO_3$. Similar to the results obtained in Na_2SO_4, the curves for Al and $TiAl_3$ can be divided into the linear part and the curved part. For the other titanium aluminides and pure titanium, the curves only show the linear region which indicates that the steady state were not reached at the end of the polarization. The curve-fitting results are summarized in Table 4-1-2-4.

4.1.2.3 Alkaline Solutions

Figure 4-1-2-5 shows the results of potentiostatic experiments for Ti, Ti_3Al, TiAl, $Ti_3Al+TiAl_{(m)}$, $Ti_3Al_{(m)}+TiAl$, $TiAl_3$ and Al obtained in NaOH. The characteristics of the curves for the intermetallics are different from those obtained in acidic and neutral solutions. This may indicate the complex nature of the dissolution mechanism for titanium aluminides in NaOH solution. According to the literature, Ti dissolution in KOH could occur in three steps[33]. The first step is the dissolution of natural oxide film of TiO_2 which can be described as:

$$TiO_2 + OH^- \dashrightarrow HTiO_3^- \qquad [4\text{-}1\text{-}2\text{-}7]$$

The second step is the film growth:

$$Ti + OH^- \dashrightarrow Ti(OH)_3 + 3e^- \qquad [4\text{-}1\text{-}2\text{-}8]$$

This reaction is in accordance with the Pourbaix diagram and it occurs only on virgin sites of the Ti where the natural oxide film previously dissolved, or by migration of the OH^- ions through the structural defects on the thinnest parts of the natural oxide film. The third step is the slow transformation of $Ti(OH)_3$ into the hydrated TiO_2 layer:

$$Ti(OH)_3 \dashrightarrow TiO_2.H_2O + 1/2H_2 \qquad [4\text{-}1\text{-}2\text{-}9]$$

Therefore, the curved shape of the potentiostatic curves in NaOH could indicate the complex nature of the titanium dissolution reactions.

As shown in Table 4-1-2-5, Al and $TiAl_3$ show the highest values of SSCD among the investigated materials. Also, values of SSCD for titanium aluminides except $TiAl_3$, are very similar to that of Ti.

Figure 4-1-2-6 shows the results of potentiostatic experiments for Ti, Ti_3Al, TiAl, $Ti_3Al+TiAl_{(m)}$, $Ti_3Al_{(m)}+TiAl$, $TiAl_3$ and Al obtained in $NaOH+Na_2SO_4$. Similar to the results obtained in NaOH, the curves for the intermetallics show different characteristics from those obtained in acidic and neutral solutions. The SSCD values for titanium aluminides, except $TiAl_3$, are very similar to that of Ti. The experiment results in $NaOH+Na_2SO_4$ are shown Table 4-1-2-6.

4.1.2.4 Summary of Potentiostatic Experiments

The dissolution behavior of titanium aluminides is pH dependent. In the acidic solutions, the SSCD increases with the increase of Al content in the materials. In the alkaline solutions, although Al has much higher dissolution rate, dissolution rates of titanium aluminides, except $TiAl_3$, are very similar to that of Ti. In the neutral solutions, titanium aluminides show relatively low dissolution rates. At the end of polarization, none of the titanium aluminides have reached the steady state, except for $TiAl_3$. The values of current density for all the investigated materials in acidic, neutral, alkaline solutions after one hour polarization are shown in Table 4-1-7.

4.1.3 Electrochemical Impedance Spectroscopy (EIS)

4.1.3.1 Equivalent Circuit

In a metal/film/solution system, a space charge can be formed in the passive film as illustrated in Figure 4-1-3-1. In order to determine the capacitance value C_{SC} of the space-charge layer in the passive film, curve fitting was applied to the Bode diagrams. Based on the experimental and the curve fitting results, an equivalent circuit was determined. The circuit consists of a series connection of one parallel RC circuits, where C is the capacitance of the space charge layer and R is its resistance, and a resistance of solution R_S. Examples of the curve fitting results for Ti, Ti_3Al and TiAl in H_2SO_4 and NaOH are shown in Figure 4-1-3-2 to Figure 4-1-3-4 respectively. The curve fitting results of the Bode diagrams for Ti and Ti_3Al are in agreement with the experimental results. However, for TiAl, some deviations were observed. Such difference could be attributed to adverse effect of Al on the dissolution of TiAl in NaOH and H_2SO_4[80].

4.1.3.2 Capacitance and Film Formation Potential

Figure 4-1-3-5 shows the reciprocal of the capacitance, C^{-1}, measured at various measurement potentials V_m, where V_m values are equal to the film formation potentials for both H_2SO_4 and NaOH. For all the three specimens in both solutions, a linear relation was observed between C^{-1} and V_m. The capacitance of passive film is related to the passive film thickness by equation [4-1-3-1][38,81]:

$$C_{SC} = \varepsilon\varepsilon_0 A/d \qquad [4\text{-}1\text{-}3\text{-}1]$$

where C_{SC} is the capacitance of the space charge layer of the passive film, ε is the dielectric constant of the passive film, ε_0 is the permittivity of free space, A is the area of the specimen and d is the film thickness. The linear relation between the reciprocal of the capacitance of the space charge, C_{SC}^{-1}, and the film formation potential, V_m, indicates that the growth of the passive film is proportional to the film formation potential. The passive film thickness for titanium aluminides can be estimated by assuming the passive films have a dielectric constant similar to that of TiO_2 which is about 60[78]. Therefore the passive film thickness of Ti, Ti_3Al and TiAl can be estimated to be 4nm, 9nm and 12nm respectively in H_2SO_4 formed at potential 2V, and 5nm, 8nm and 9nm in NaOH formed at potential 0.6V. The calculated film thickness might also be affected by the Helmholtz capacitance. In general, the measured capacitance C is not the same as the capacitance of space charge layer, C_{SC}. According to the literature, the relationship between the capacitance measured, C, and the space charge capacitance, C_{SC}, is as the following[24]:

$$C^{-1} = C_{SC}^{-1} + C_H^{-1} \qquad [4\text{-}1\text{-}3\text{-}2]$$

where C_H is the capacitance of the Helmholtz layer at the oxide surface. If $C_{SC} << C_H$, then $C_{SC} \cong C$. According to the literature, $C_{SC} << C_H$ is valid for Ti[12]. Using ε=60 and $C_{SC} << C_H$, the growth rate for titanium aluminides can be estimated as around 2-4 nmV^{-1} which is typical for anodic oxide films on many metals[32,40].

4.1.3.3 Mott-Schottky Plot

Figure 4-1-3-6 shows the Mott-Schottky plots for passive films formed on Ti, Ti_3Al and TiAl in H_2SO_4 at different film formation potentials. For Ti, the plots for passive films formed at 0.2, 0.6, and 1 V show a linear relation between C^{-2} and the measured potentials. At higher film formation potentials, the deviation from linearity in the Mott-

Schottky plots was observed. Such deviation for Ti was also found by other researchers[12,66,82].

For Ti_3Al and TiAl, the Mott-Schottky plots show similar shape and the deviations occurred at potentials around 0.6 V for passive films formed at 1.5V and 2V. For Ti and the intermetallics, the slope of the Mott-Schottky plots increases with the increase of the film formation potential.

The Mott-Schottky plots for passive films formed in NaOH are shown in Figure 4-1-3-7. The linear relation between C^{-2} and the measurement potential is observed. The linear plots for the films formed at -0.2, 0, and 0.4 V have similar slopes. This is different from that in H_2SO_4, where the slope increases with the increase of the film formation potential.

The Mott-Schottky plots for passive films formed in HNO_3 are shown in Figure 4-1-3-8. For all the materials, the deviation from linearity was observed. The deviation is more significant for films formed at higher potentials than those formed at lower potentials. The shapes of the plots for the investigated materials are similar to that in H_2SO_4. However, for Ti_3Al, a significant increase of the slope at formation potential 2V was observed. For TiAl, the highest film formation potential used was 1.5V, since at potential higher than 1.5V, passive film breakdown occurred as shown in Figure 4-1-2.

The passive film formed on Ti was found to be a n-type semiconductor[83-85]. The positive values of the slopes in the linear region also indicate that the passive films formed on Ti_3Al and TiAl in both solutions have such n-type semiconductor property[86]. The value of the donor density, N_D, can be calculated from the Mott-Schottky plot, using the equation[12]:

$$\frac{1}{C^2} = \frac{1}{C_H^2} + \frac{2}{e \cdot N_D \varepsilon \varepsilon_0}(V_m - V_{FB} - kT/e) \qquad [4\text{-}1\text{-}3\text{-}3]$$

where C is the total measured capacitance, C_H is the Helmholtz capacitance, e is the charge of electron, ε_0 is the permittivity of the free space, ε is the dielectric constant, N_D is the donor density, V_m is the imposed potential, V_{FB} is the flatband potential, K is the Boltzman constant and T is the absolute temperature. For plots showing the deviation in the Mott-Schottky plot, the low potential linear part is used to calculate the N_D[66,83,87]. According to the literature, the discrepancy from the ideal Mott-Schottky plot could come from the presence of surface states which include intrinsic surface states, Lewis sites, and surface states arising from foreign species[64,88]. An alternative mechanism is the nonhomogenous donor distribution[89] which will be further discussed in Chapter 5.

Due to the lack of the dielectric constant data for titanium aluminide passive films in the literature, in this study, it is assumed the dielectric constants for passive films formed on Ti_3Al and TiAl are the same as that of Ti in all the solutions used, which is about 60[78]. As discussed in the previous section, based on this dielectric constant value, the film growth rates for titanium and titanium aluminides is around 2-4nmV^{-1}, which are typical for passive films on many metals[32,40]. Therefore, the donor densities can be calculated using equation [4-1-3-3] by measuring the slope of the Mott-Schottky plots. Donor densities for the passive films formed in H_2SO_4, NaOH, and HNO_3 are shown in Figure 4-1-3-9. For all the specimens, the donor density decreases with the increase of the film formation potential. Leitner et al.[68] has shown that for Ti, at low film formation potential, the passive film might be largely non-stoichiometric and possibly amorphous or highly disordered; at high formation potential, a stoichiometry close to TiO_2 and crystallinity of the film can be formed. Therefore, the donor density data indicate that the higher disorder the film structure, the higher donor density in the film.

In H_2SO_4, the donor densities increase in the order: TiAl < Ti_3Al < Ti. In NaOH or HNO_3, Ti has the lowest donor density while TiAl and Ti_3Al have very similar values. The donor density of Ti ranges from 10^{20} to 10^{21} cm^{-3} which is typical for thin oxide films on Ti[68,88]. Such high donor concentration could be attributed to the amorphous structure of the passive film formed at low potentials[31].

Mott-Schottky plot could also be used to estimate the flatband potentials. The principal difficulty lies in evaluating the Helmholtz capacitance C_H, as illustrated in Figure 2-6. According to the literature, the Helmholtz capacitance C_H, is considered to be independent of the imposed potential and usually to be much larger than the capacitance of the depletion layer of the semiconductor C_{SC}. According to equation [4-1-3-3], the potential shift caused by C_H is $eN_D\varepsilon\varepsilon_0/2C_H^2$. Assuming a C_H of 80 μFcm^{-2}[83], the flatband potentials can be estimated from extrapolation of C^{-2} to $C^{-2} = 0$ in the Mott-Schottky plot and justifies the value with the potential shift by C_H[12,66]. Therefore, the flatband potential can be expressed as:

$$V_{FBi} = V_{0i} - kT/e + eN_{Di}\varepsilon\varepsilon_0/2C_H^2 \qquad [4\text{-}1\text{-}3\text{-}4]$$

where V_{0i} is the potential estimated from extrapolation of C^{-2} to $C^{-2} = 0$ in the Mott-Schottky plot. The 'i' denotes the different formation potentials. The flatband potentials calculated for Ti, Ti_3Al and TiAl in H_2SO_4, NaOH and HNO_3 are shown in Table 4-1-3-1, 4-1-3-2, and 4-1-3-3.

The flatband potentials calculated for Ti, Ti_3Al and TiAl in H_2SO_4 are very similar to the values reported by Fonseca et al., which is around -0.3 to -0.4 V[83]. The flatband potentials for Ti, Ti_3Al and TiAl in HNO_3 are similar to the results obtained in H_2SO_4. In NaOH, the flatband potential for Ti_3Al and TiAl are quite different from that for Ti.

The flatband potentials calculated using equation [4-1-3-4], generally are sensitive to the choosing of C_H. For example, choosing C_H as 40 μFcm^{-2} instead of 80 μFcm^{-2} will result in flatband potential shifting about +0.1V in the case of Ti_3Al. The flatband potential of Ti is more sensitive to C_H due to its high N_D value. Therefore, a more sophisticated method is needed to verify our result. According to semiconductor physics, for a classical semiconductor, the following equation can be used[83]:

$$E_F = E_C + kT\ln(N_D/N_C) \qquad [4\text{-}1\text{-}3\text{-}5]$$

where E_F and F_C are the positions in the energy band diagram of the Fermi level and the conduction band, N_C is a characteristic parameter of the effective electronic density in the conduction band. In the potential scale and in flatband conditions, by definition, $eV_{FB} = -E_F$ and $eV_C = -E_C$. Therefore, equation [4-1-3-5] can also be written in the form:

$$-V_{FB} = -V_C + (kT/e)\ln(N_D/N_C) \qquad [4\text{-}1\text{-}3\text{-}6]$$

Substituting equation [4-1-3-6] in equation [4-1-3-4], leads to[83]:

$$V_{0\,i} - (kT/e)\ln(N_{D\,l}/N_{D\,i}) = V_{FBl} + (kT/e) - eN_{D\,i}\varepsilon\varepsilon_0/2C_H^2 \qquad [4\text{-}1\text{-}3\text{-}7]$$

where 'i' denotes for different film formation potentials, 'l' is for a particular film formation potential. Therefore, the plot of $V_{0\,i} - (kT/e)\ln(N_{D\,l}/N_{D\,i})$ as a function of $eN_{Di}\varepsilon\varepsilon_0/(2C_H^2)$ leads to the determination of V_{FBl} and C_H. As V_{FBl} is little dependent on N_D, this value can be considered as a good approximation of the average flatband potential.

Equation [4-1-3-7] was first proposed by Fonseca et al. to estimate C_H for Ti in H_2SO_4[83]. For simplicity, the plot based on equation [4-1-3-7] is called Fonseca plot in this paper. The Fonseca plots for the passive films formed in H_2SO_4 and HNO_3 are shown in Figure 4-1-3-10. The flatband potentials and C_H derived for H_2SO_4 and HNO_3 are listed in Table 4-1-3-4 and Table 4-1-3-5. The values of the flatband potentials estimated based on the Fonseca method are very similar to the results obtained using the previous method. The difference may caused mainly by the selecting of C_H. Using the Fonseca method, C_H were estimated as 40-50 μFcm^{-2}. For NaOH, no linear plot can be derived using the Fonseca method. This could be attributed to the complex nature of the passive film formation and dissolution reactions in NaOH, as discussed in the previous sections.

4.1.3.4 Summary of EIS Experiments

The EIS results in H_2SO_4, HNO_3 and NaOH show that Ti, Ti_3Al and TiAl passive films have n-type semiconductor properties. The donor densities are derived from the Mott-Schottky plots for Ti, Ti_3Al and TiAl in H_2SO_4, HNO_3 and NaOH solutions. The donor densities decrease with the increase of the film formation potential. The donor densities for the Ti passive films are significantly higher than those for Ti_3Al and TiAl under the same experiment conditions.

4.2 Surface Analysis: X-ray Photoelectron Spectroscopy (XPS)

XPS analyses were performed to evaluate the passive film compositions of Ti_3Al and TiAl formed in H_2SO_4, NaOH and HNO_3. Figure 4-2-1 shows the XPS survey spectra for Ti_3Al and TiAl potentiostatically passivated in H_2SO_4, HNO_3 and NaOH. Strong Ti 2p and O 1s peaks and a relatively strong C 1s peak dominated the spectra of all the specimens. Significant peaks from Si were always observed on the surfaces of the specimens passivated in H_2SO_4 and NaOH. In HNO_3, the Si peaks are nearly non-detectable. A small nitrogen peak was also detected for specimens passivated in H_2SO_4. For those passivated in HNO_3 and NaOH, the nitrogen peak was less significant. The nitrogen peak for passive films formed in HNO_3 may not be an indication of the existence of M_xNO_3, because even stronger signals of nitrogen appeared on passive films formed in H_2SO_4 and NaOH. For passive films formed in H_2SO_4 and HNO_3, relatively strong Al peaks were observed. For films formed in NaOH, Al peaks were not observed on the surface. There was no sign of sulfur detected for specimens passivated in H_2SO_4.

Figure 4-2-2 shows typical appearance of the high-resolution XPS spectra of the Ti 2p region from the passivated samples. Spectra from different depth were derived by Ar^+ sputtering, where Figure 4-2-2a shows the signal from the topmost layer, Figure 4-2-2b and 4-2-2c show signals after several cycles of Ar^+ sputtering. In the figures, solid lines are used for the actual XPS spectra and backgrounds, and dashed lines are used for the peaks generated by the curve fitting program. As shown in Figure 4-2-2a, the shape and position of the Ti $2p_{1/2}$ and $2p_{3/2}$ peaks are found to correspond to Ti^{4+}, with binding energies around 464.8 eV and 459 eV, respectively. The $2p_{3/2}$ values are very close to the reported values for Ti and Ti-Ni alloys passivated in sulfuric acid, which are 458.98 eV and 458.90 eV, respectively[90]. After several cycles of Ar^+ sputtering, other oxidation states were also observed. As shown in Figure 4-2-2b, the spectrum was deconvoluted to three $2p_{3/2}$ and three $2p_{1/2}$ peaks which correspond to Ti^{4+}, Ti^{3+}, and Ti^{2+}, respectively. After further removal of the surface atoms by sputtering, a binding energy corresponding to metallic Ti eventually became dominant, as shown in Figure 4-2-2c. The binding energies of $2p_{3/2}$ peaks for different chemical states of Ti are listed in Table 4-2-1. The binding energies (B_E) around 457 eV, 455eV, and 454eV correspond to Ti^{3+}, Ti^{2+} and metallic Ti respectively[90]. The depth profiles for the different chemical states of Ti are generated by measuring the area under each peak.

Figure 4-2-3 shows a typical appearance of the high-resolution XPS spectra of the Al 2p region from the samples passivated in H_2SO_4. Spectra from different depth were derived from Ar^+ sputtering, where Figure 4-2-3a shows the signal from the topmost layer, Figure 4-2-3b and Figure 4-2-3c show the signals after several cycles of Ar^+ sputtering. The peak with binding energy of 75V in Figure 4-2-3a corresponds to Al^{3+}[91]. Nearly all Al are in Al^{3+} state on the topmost layer. After several cycles of Ar^+ sputtering, the Al signals can be deconvoluted to two peaks as shown in Figure 4-2-3b. The peak at about 72 eV corresponds to metallic Al[91]. After more cycles of Ar^+ sputtering, only metallic Al left in the film as shown in Figure 4-2-3c. For the films formed in HNO_3, the results are similar to that in H_2SO_4.

For the films formed in NaOH, however, no Al signals were found on the surface until after several cycles of Ar^+ sputtering. Similar to the results in H_2SO_4 and HNO_3, at the initial depth where the Al signal first appeared, almost all the Al atoms are in the Al^{3+} state. The metallic Al gradually becomes dominant with the increase of depth. The O 1s spectrum could be deconvoluted into two peaks as shown in Figure 4-2-4. The peak at 531 eV could be attributed to O^{2-} or OH^-, while the peak at 533 eV could be attributed to adsorbed or bound water[90]. The binding energies for different oxidation states of Al and oxygen species in different solutions are also shown in Table 4-2-1.

The original depth profiles for TiAl are shown in Figure 4-2-5. As shown in Figure 4-2-5, the relative concentration of C is in the range 23% - 45% at the outermost surfaces of passivated titanium aluminide specimens. After one cycle of Ar^+ sputtering, the carbon concentration is substantially reduced. The C 1s peak is dominated by a peak at 285 eV which can be assigned to hydrocarbons[92]. Therefore, this very high concentration of carbon on the surface could be caused by surface contamination. Besides C, there are also significant peaks of Si detected on the surface which is also resulted from surface contamination. The Si peaks can be attributed to our specimen polishing method where SiC papers were used. Since this study is focused on the elements associated with the passive film formation and dissolution, in the following depth profiles, only Ti, Al and O are included for further analysis.

Figure 4-2-6 shows the depth profiles for Ti, Al and O in the passive films formed on Ti_3Al and TiAl in H_2SO_4. All the depth values shown in the graphs are based on the measurement of the sputtering rate for SiO_2. For Ti_3Al, the oxygen content drops to half of its maximum atom percent at around 290Å (from more than 80% to 40%). For TiAl, the oxygen content drops to half of its maximum concentration at around 150Å. We can also see that Al has a relatively higher concentration in the outer layer of the passive films than in the bulk materials for both Ti_3Al and TiAl, as shown in Figure 4-2-7. The depth profiles for different oxidation states of Ti are shown in Figure 4-2-8. Ti^{4+} is nearly 100% before the Ar^+ sputtering. It gradually decreases to zero at around 150Å. The concentration of Ti^{3+} increases from zero to around 40% at depth 40Å, and then starts to decrease until it reaches zero at around 250Å. Ti^{2+} shows profiles similar to that of Ti^{3+}. However, Ti^{2+} concentration is relatively high even at depths around 300Å.

Depth profiles for different oxidation states of Al are shown in Figure 4-2-9. Al^{3+} is nearly 100% before the Ar^+ sputtering. It gradually decreases to 50% at around 130Å for Ti_3Al and 240Å for TiAl.

The depth profiles for films formed in HNO_3 are very similar to that in H_2SO_4. As shown in Figure 4-2-10, for both Ti_3Al and TiAl, the oxygen still exists in a small amount even at a very large depth (>1000Å) from the surface. Al has a relatively higher concentration on the surface than in the bulk materials as shown in Figure 4-2-11. The

Al/Ti ratio gradually reaches to 0.33 for TiAl, and reaches to 1 for Ti_3Al, which is very close the bulk ratio. The depth profiles of oxidation states of Ti are shown in Figure 4-2-12 and those for Al are shown in Figure 4-2-13. The characteristics of the distribution of different oxidation states of Ti and Al are very similar to the films formed in H_2SO_4.

The depth profiles for passive films formed in NaOH are quite different from those formed in H_2SO_4 and HNO_3, as shown in Figure 4-2-14. In the topmost layers of the passive films, the concentration of Al is nearly zero for both Ti_3Al and TiAl. Al gradually reaches around 5% at depth around 100Å. Al increases to the bulk concentration at around 400Å from the surface. For Ti_3Al, as shown in Figure 4-2-15, the ratio of Al/Ti eventually reaches 0.4 which is very close to the bulk ratio of 0.33. The Al/Ti ratio for TiAl reaches 1.4 at a large depth which is a little different from the bulk ratio of 1 as shown in Figure 4-2-15. Such deviation is not very significant and could be caused by the variation of composition in the TiAl specimen. For either Ti_3Al or TiAl, in the topmost layers, there are only titanium oxides and the ratio of Ti:O is close to 1:2. The distributions of oxidation states of titanium are shown in Figure 4-2-16, where the Ti^{4+} ion is the dominant species in the topmost layers. This is in agreement with the conclusion of other researchers that TiO_2 is the main component in the passive film of Ti[32]. The distributions of oxidation states of Al, as shown in Figure 4-2-17, are similar to those formed in the acidic solutions except that Al has very low concentration on the outer layers of the passive films.

Table 4-1-1-1. Summary of potentiodynamic experiment results in H_2SO_4

	Ti	Ti_3Al	Ti_3Al + $TiAl_{(m)}$	$Ti_3Al_{(m)}$ + TiAl	TiAl	$TiAl_3$	Al
E_{corr} (V)	-0.70	-0.70	-0.77	-0.72	-0.62	-0.54	-0.67
E_{pp}(V)	-0.56	-0.54	-0.56	-0.55	-0.50	-0.4	N/A
Critical Passivation Current Density (Acm^{-2})	9.5 e-5	11.6 e-5	13.6 e-5	16.8 e-5	19.9 e-5	8.5 e-5	N/A
Minimum Passive Current Density (Acm^{-2})	1.9 e-5	1.9 e-5	3.0 e-5	3.6 e-5	7.7 e-5	8.2 e-5	N/A

E_{pp}: primary passive potential

Table 4-1-1-2. Summary of the potentiodynamic experiment results in HNO_3

	Ti	Ti_3Al	Ti_3Al + $TiAl_{(m)}$	$Ti_3Al_{(m)}$ + TiAl	TiAl	$TiAl_3$	Al
E_{corr} (V)	0.17	0.04	-0.16	-0.28	-0.19	-0.40	-0.43
Breakdown Potential (V)	N/A	N/A	1.77	1.69	1.67	1.65	1.59
Minimum Passive Current Density (Acm^{-2})	1.42 e-5	1.42 e-5	2.33 e-5	2.9 e-5	4.0 e-5	12.1 e-5	14.4 e-5

Table 4-1-1-3. Summary of potentiodynamic experiment results in Na_2SO_4

	Ti	Ti_3Al	Ti_3Al + $TiAl_{(m)}$	$Ti_3Al_{(m)}$ + TiAl	TiAl	$TiAl_3$	Al
E_{corr} (V)	-0.78	-0.62	-0.59	-0.56	-0.61	-0.63	-0.96
E_{pp} (V)	-0.56	-0.54	-0.56	-0.55	-0.50	-0.4	N/A
Minimum Passive Current Density (Acm^{-2})	1.01 e-5	0.73 e-5	0.80 e-5	0.75 e-5	0.79 e-5	1.2 e-5	N/A

E_{pp}: primary passive potential

Table 4-1-1-4. Summary of potentiodynamic experiment results in $NaNO_3$

	Ti	Ti_3Al	Ti_3Al + $TiAl_{(m)}$	$Ti_3Al_{(m)}$ + TiAl	TiAl	$TiAl_3$	Al
E_{corr} (V)	-0.50	-0.48	-0.45	-0.41	-0.52	-0.38	-0.51
Breakdown Potential (V)	N/A	N/A	1.98	1.75	1.75	1.66	1.55
Minimum Passive Current Density (Acm^{-2})	1.1 e-5	0.84 e-5	0.79 e-5	0.74 e-5	0.45 e-5	0.97 e-5	N/A

Table 4-1-1-5. Summary of potentiodynamic experiment results in NaOH

	Ti	Ti_3Al	Ti_3Al + $TiAl_{(m)}$	$Ti_3Al_{(m)}$ + TiAl	TiAl	$TiAl_3$	Al
E_{corr} (V)	-1.43	-1.49	-1.52	-1.36	-1.36	-1.27	-1.46
Critical Passivation Current Density (Acm^{-2})	9 e-5	6.9 e-5	2.6 e-5	1.1 e-5	1.1 e-5	9.3 e-5	N/A
Minimum Passive Current Density (Acm^{-2})	2.2 e-5	1.3 e-5	1.0 e-5	1.0 e-5	1.2 e-5	10.0 e-5	N/A

Table 4-1-1-6. Summary of potentiodynamic experiment results in NaOH+Na_2SO_4

	Ti	Ti_3Al	Ti_3Al + $TiAl_{(m)}$	$Ti_3Al_{(m)}$ + TiAl	TiAl	$TiAl_3$	Al
E_{corr} (V)	-1.33	-1.45	-1.51	-1.42	-1.34	-1.45	-1.50
Critical Passivation current (Acm^{-2})	5.8 e-5	11.0 e-5	18.4 e-5	2.0 e-5	1.5 e-5	9.6 e-4	N/A
Minimum Passive Current Density (Acm^{-2})	1.2 e-5	1.0 e-5	1.04 e-5	1.1 e-5	1.5 e-5	51.0 e-5	N/A

Table 4-1-2-1. Current densities at the end of one hour polarization at 1V in H_2SO_4

Sample	SSCD (Acm^{-2})
Ti	1.26e-06
Ti_3Al	3.47e-06
$Ti_3Al+TiAl_{(m)}$	9.17e-06
$Ti_3Al_{(m)}+TiAl$	1.18e-05
TiAl	3.1e-05
$TiAl_3$	1.46e-4
Al	5.61e-4

Table 4-1-2-2. Curve fitting parameters for potentiostatic polarization curves obtained in HNO_3

Sample	i_d (Acm^{-2})	A	t_0 (s)	α
Ti	3.04e-7	3.68e-4	0.984	0.884
Ti_3Al	1.93e-6	4.43e-4	0.225	0.969
$Ti_3Al+TiAl_{(m)}$	5.70e-6	5.43e-4	0.185	1.069
$Ti_3Al_{(m)}+TiAl$	1.180e-5	5.19e-4	0.247	1.076
TiAl	2.574e-5	3.35e-3	3.82	1.536
$TiAl_3$	2.14e-4	0.0125	3.402	1.926

* Curve fittings are based on equation [4-1-2-5]

* Applied potential is 1V

Table 4-1-2-3. Curve fitting parameters for potentiostatic polarization curves obtained in Na_2SO_4

Sample	i_0 (Acm^{-2})	A	t_0 (s)	α
Ti	N/A	5.57e-4	-0.646	0.935
Ti_3Al	N/A	3.57e-4	-0.300	0.952
$Ti_3Al+TiAl_{(m)}$	N/A	4.51e-4	-0.716	0.941
$Ti_3Al_{(m)}+TiAl$	N/A	3.27e-4	-0.588	0.936
TiAl	N/A	3.35e-4	-0.649	0.922
$TiAl_3$	8.35e-7	4.33e04	-0.204	0.896
Al	1.04e-4	6.12e-3	0.884	1.11

* Curve fittings are based on equation [4-1-2-5] or equation [4-1-2-6]

* Applied potential is 1V

Table 4-1-2-4. Curve fitting parameters for potentiostatic polarization curves obtained in $NaNO_3$

	i_0 (Acm^{-2})	A	t_0 (s)	α
Ti	N/A	6.70e-4	-14.6	0.975
Ti_3Al	N/A	1.13e-3	8.06	1.122
$Ti_3Al+TiAl_{(m)}$	N/A	3.95e-4	-0.698	0.942
$Ti_3Al_{(m)}+TiAl$	N/A	03.70e-4	-0.628	0.939
TiAl	1.02e-7	4.25e-4	-0.649	0.950
$TiAl_3$	6.18e-6	1.67e-3	0.237	0.970

* Curve fittings are based on equation [4-1-2-5] or equation [4-1-2-6]

* Applied potential is 1V

Table 4-1-2-5. Current densities at the end of one hour polarization at 0.2V in NaOH

Sample	SSCD (Acm^{-2})
Ti	3.47887e-06
Ti_3Al	4.30075e-06
$Ti_3Al+TiAl_{(m)}$	1.9037e-06
$Ti_3Al_{(m)}+TiAl$	1.68613e-06
TiAl	4.34815e-06
$TiAl_3$	9.55385e-05
Al	0.133684

Table 4-1-2-6. Current densities at the end of one hour polarization at 0.2V in $NaOH+Na_2SO_4$

Sample	SSCD (Acm^{-2})
Ti	1.11e-6
Ti_3Al	2.32e-6
$Ti_3Al+TiAl_{(m)}$	2.16e-6
$Ti_3Al_{(m)}+TiAl$	2.34e-6
TiAl	4.04e-6
$TiAl_3$	2.04e-4
Al	0.092

Table 4-1-2-7. Summary of current densities at the end of one hour polarization obtained in acidic, neutral and alkaline solutions

Sample	H_2SO_4 (Acm^{-2})	HNO_3 (Acm^{-2})	Na_2SO_4 (Acm^{-2})	$NaNO_3$ (Acm^{-2})	NaOH (Acm^{-2})	Na_2SO_4 + NaOH (Acm^{-2})
Ti	1.26e-6	5.65e-7	2.5e-7	2.34e-7	3.49e-6	1.11e-6
Ti_3Al	3.47e-6	2.18e-6	1.44e-7	1.52e-7	4.30e-6	2.32e-6
$Ti_3Al+TiAl_{(m)}$	9.17e-6	5.75e-6	1.91e-7	1.50e-7	1.90e-6	2.16e-6
$Ti_3Al_{(m)}+TiAl$	1.18e-5	1.16e-5	1.45e-7	1.42e-7	1.69e-6	2.34e-6
TiAl	3.08e-5	2.56e-5	1.81e-7	2.97e-7	4.35e-6	4.04e-6
$TiAl_3$	1.46e-4	2.03e-4	1.23e-6	7.38e-6	9.55e-5	2.04e-4
Al	5.61e-4	1.19e-3	1.05e-4	3.55e-4	0.134	0.092

Applied Potential = 1 V for H_2SO_4, HNO_3, Na_2SO_4, $NaNO_3$

Applied Potential = 0.2 V for NaOH, Na_2SO_4 + NaOH

Table 4-1-3-1. Flatband potentials for Ti, Ti_3Al and TiAl passive films formed in H_2SO_4

Film Formation Potential V_{SCE}	Ti V_{FB} (V)	Ti_3Al V_{FB} (V)	TiAl V_{FB} (V)
0.2	-0.32	-0.39	-0.46
0.6	-0.31	-0.37	-0.44
1.0	-0.27	-0.34	-0.39
1.5	-0.27	-0.28	-0.38
2.0	-0.25	-0.25	-0.42

*Assuming $C_H = 80\ \mu Fcm^{-2}$

Table 4-1-3-2. Flatband potentials for Ti, Ti_3Al and TiAl passive films formed in HNO_3

Film Formation Potential V_{SCE}	Ti V_{FB} (V)	Ti_3Al V_{FB} (V)	TiAl V_{FB} (V)
0.2	-0.35	-0.40	-0.51
0.6	-0.34	-0.38	-0.43
1.0	-0.31	-0.33	-0.38
1.5	-0.27	-0.28	-0.37
2.0	-0.24	-0.26	N/A

* Assuming $C_H = 80\ \mu Fcm^{-2}$

Table 4-1-3-3. Flatband potentials for Ti, Ti_3Al and TiAl passive films formed in NaOH

Film Formation Potential V_{SCE}	Ti V_{FB} (V)	Ti_3Al V_{FB} (V)	TiAl V_{FB} (V)
-0.4	-1.0	-1.4	-1.5
0.0	-1.0	-1.7	-1.6
0.2	-0.95	-1.7	-1.8
0.4	-0.91	-1.5	-1.9

* Assuming $C_H = 80\ \mu Fcm^{-2}$

Table 4-1-3-4. C_H and V_{FB} for passive films formed in H_2SO_4 estimated based on the Fonseca method

	Ti	Ti_3Al	TiAl
V_{FB} (V_{SCE})	-0.201	-0.265	-0.372
C_H (μFcm^{-2})	54	40	40

Table 4-1-3-5. C_H and V_{FB} for passive films formed in HNO_3 estimated based on the Fonseca method

	Ti	Ti_3Al	TiAl
V_{FB} (V_{SCE})	-0.24	-0.33	-0.39
C_H (μFcm^{-2})	47	44	47

Table 4-2-1. Binding energies of the Ti $2p_{3/2}$, Al 2p, O 1s electrons observed on Ti_3Al and TiAl passive films formed in H_2SO_4, NaOH and HNO_3

Electron level	Chemical state	Binding energy(eV)					
		TiAl			Ti_3Al		
		H_2SO_4	NaOH	HNO_3	H_2SO_4	NaOH	HNO_3
Ti $2p_{3/2}$	metallic	454.0	454.0	454.3	454.3	454.0	454.1
	+2	455.0	455.0	455.3	455.6	455.0	455.3
	+3	457.2	457.2	456.9	457.5	457.2	457.6
	+4	458.9	459.1	458.8	458.8	459.1	459.4
Al 2p	metallic	72.4	72.1	72.3	72.2	72.1	72.4
	+3	75.5	74.9	75	75.0	75.1	75.2
O 1s	O^{2-} / OH^-	531.4	531	531.4	531.1	530.8	531.7
	H_2O	532.9	533.0	533	532.9	533.0	533.0

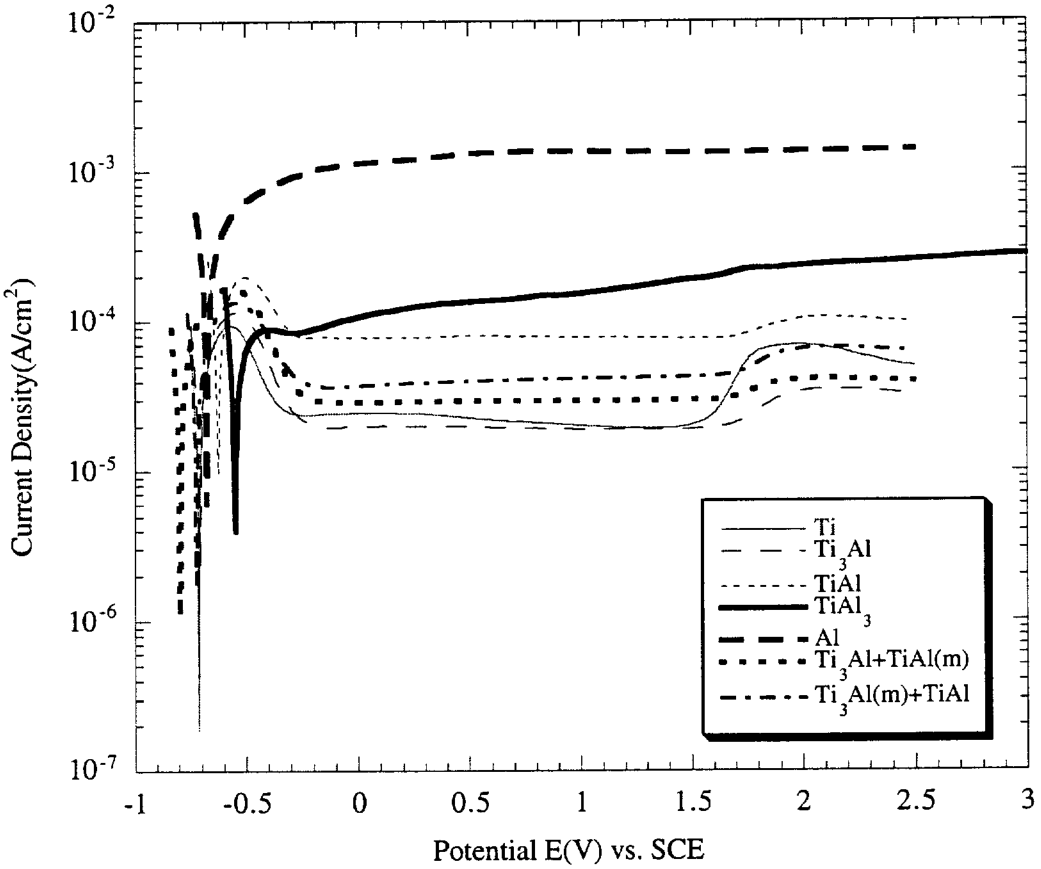

Figure 4-1-1-1. Potentiodynamic polarization curves for Ti, Ti_3Al, $Ti_3Al_{(m)}$+TiAl, Ti_3Al+$TiAl_{(m)}$, TiAl, $TiAl_3$ and Al in H_2SO_4.

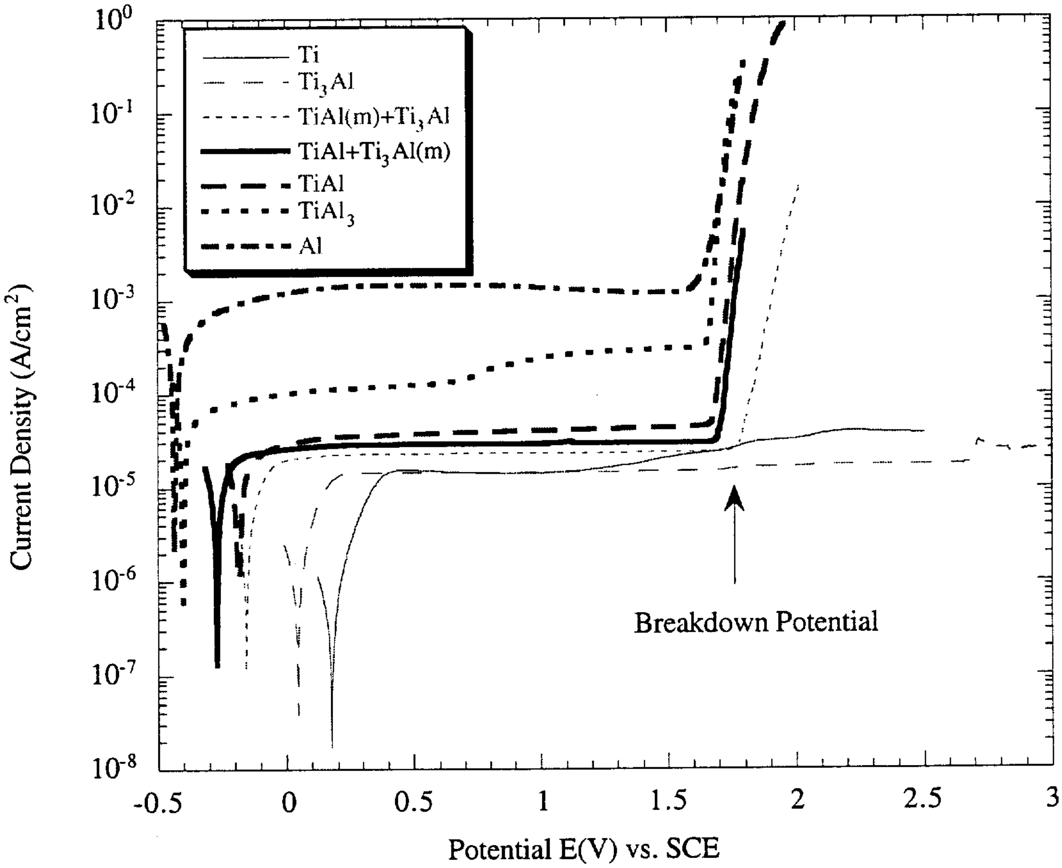

Figure 4-1-1-2. Potentiodynamic polarization curves for Ti, Ti_3Al, $Ti_3Al_{(m)}$+TiAl, Ti_3Al+$TiAl_{(m)}$, TiAl, $TiAl_3$ and Al in HNO_3.

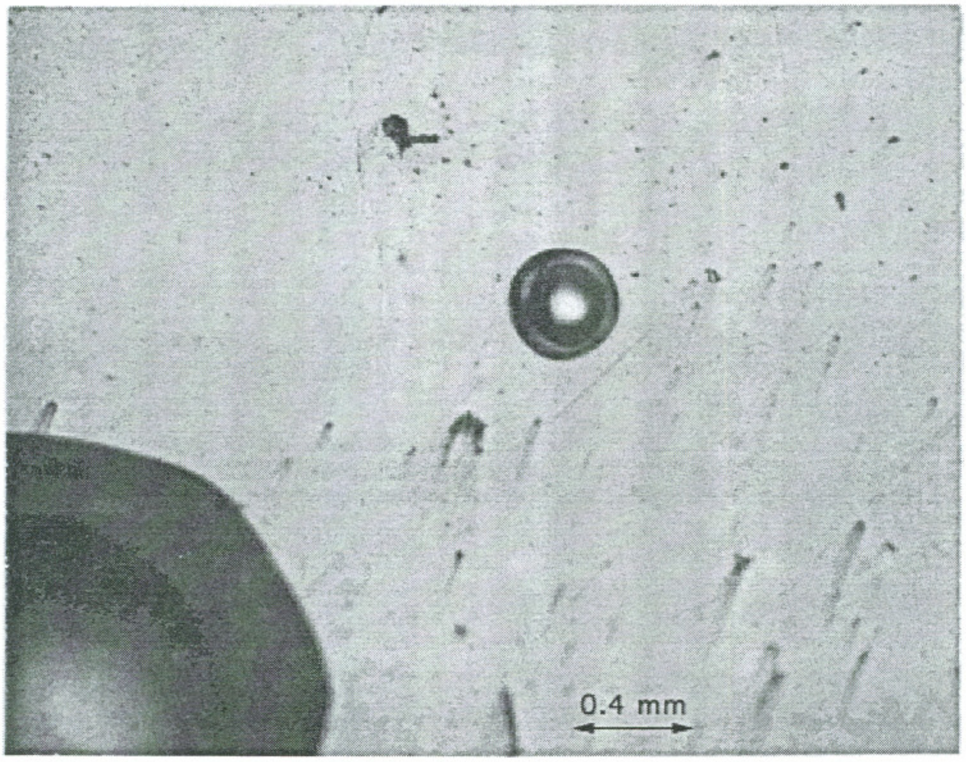

Figure 4-1-1-3. Optical micrograph of pits formed on TiAl after potentiodynamic polarization in HNO_3.

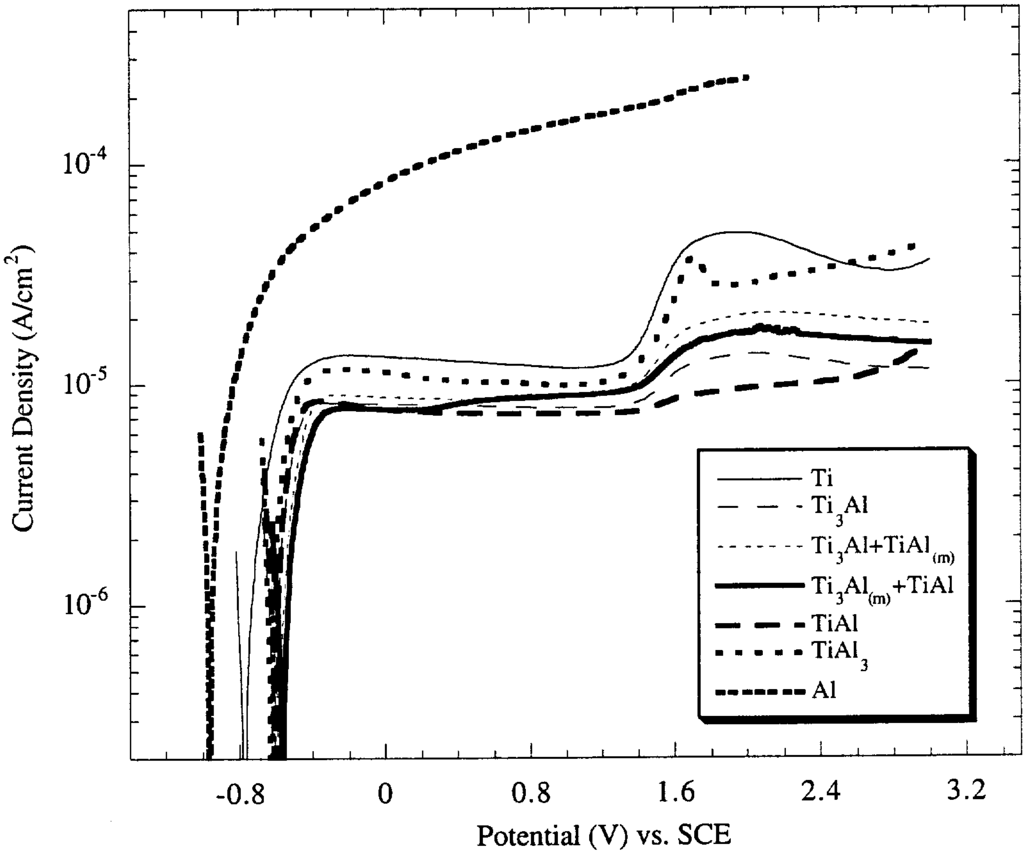

Figure 4-1-1-4. Potentiodynamic polarization curves for Ti, Ti_3Al, $Ti_3Al_{(m)}$+TiAl, $Ti_3Al+TiAl_{(m)}$, TiAl, $TiAl_3$ and Al in Na_2SO_4.

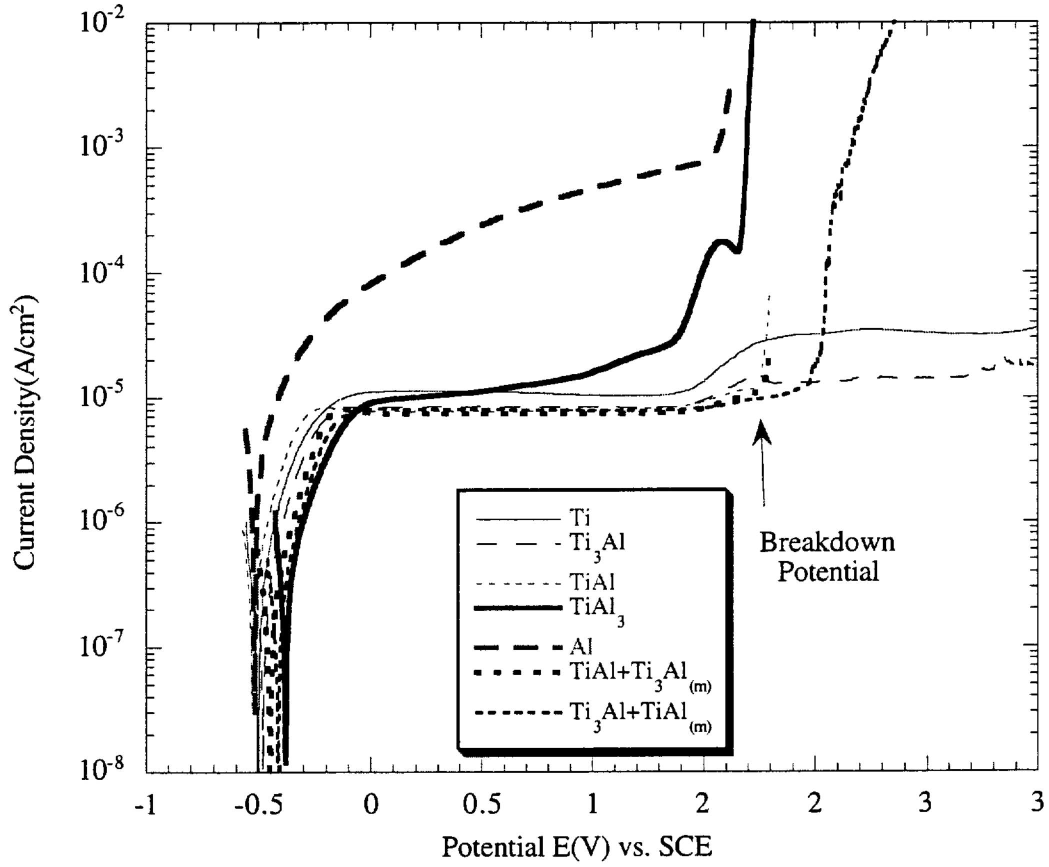

Figure 4-1-1-5. Potentiodynamic polarization curves for Ti, Ti_3Al, $Ti_3Al_{(m)}$+TiAl, Ti_3Al+$TiAl_{(m)}$, TiAl, $TiAl_3$ and Al in $NaNO_3$.

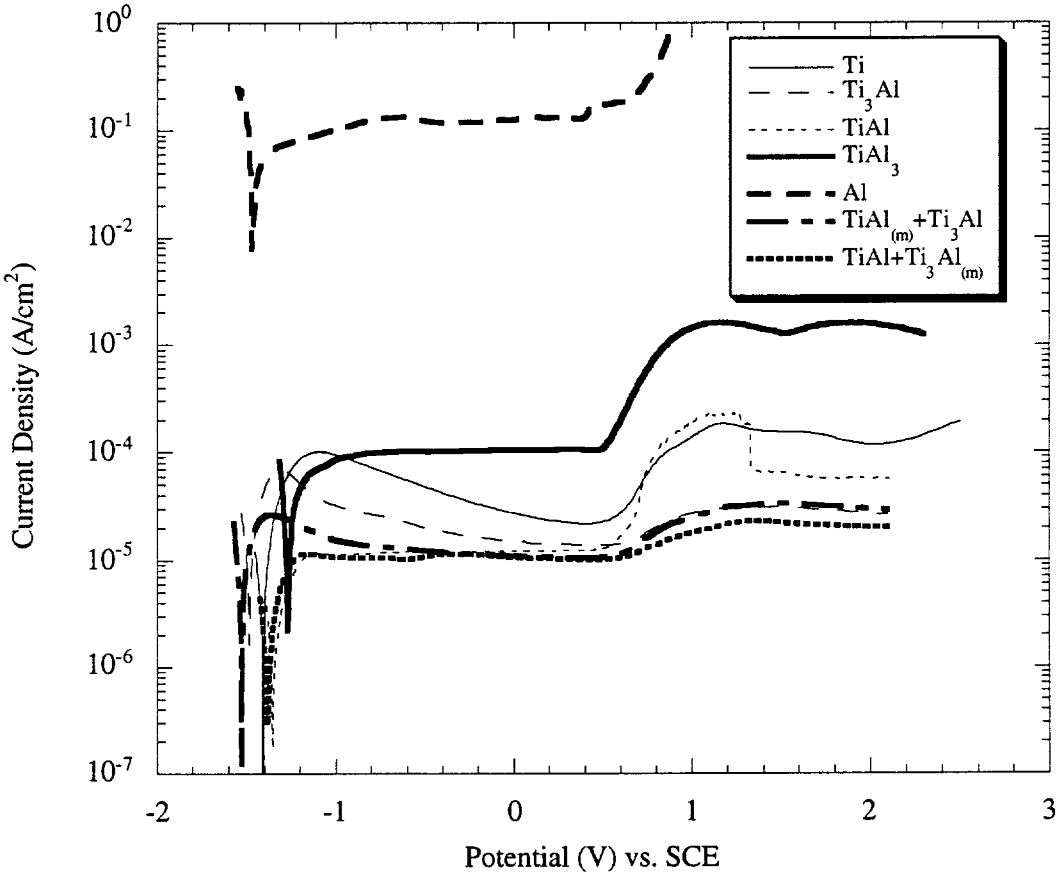

Figure 4-1-1-6. Potentiodynamic polarization curves for Ti, Ti_3Al, $Ti_3Al_{(m)}$+TiAl, Ti_3Al+$TiAl_{(m)}$, TiAl, $TiAl_3$ and Al in NaOH.

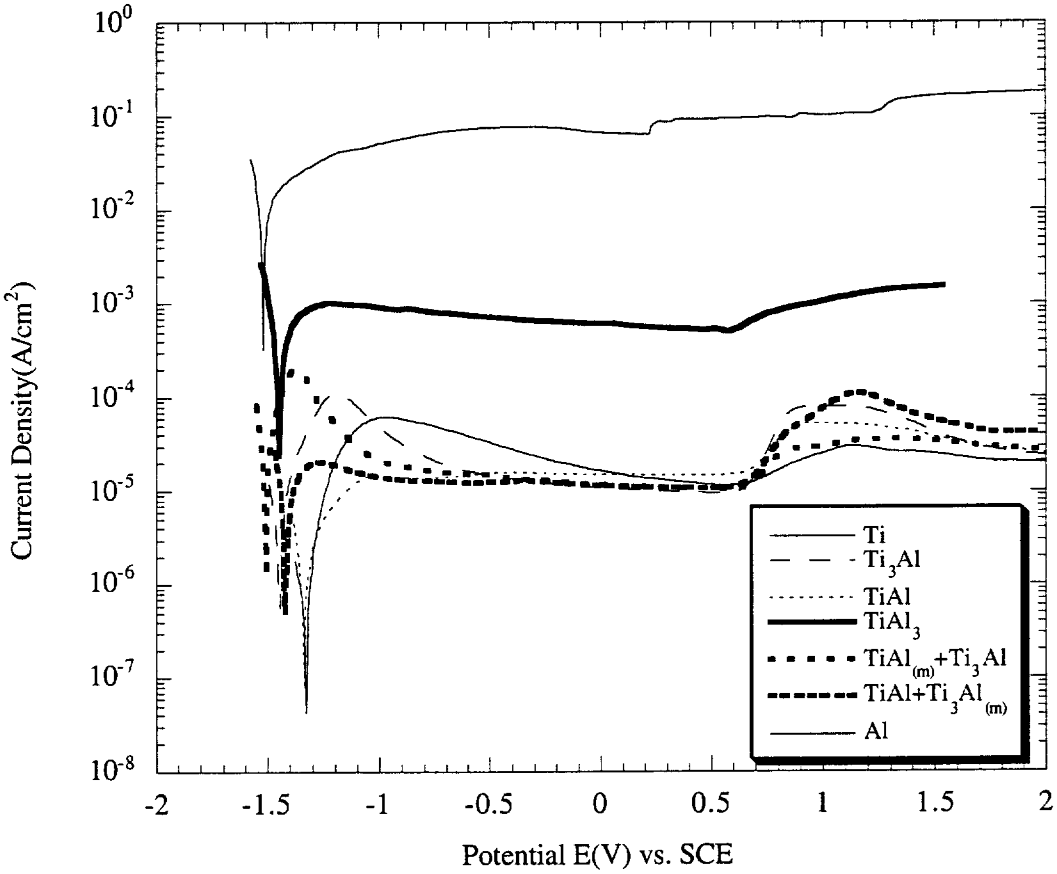

Figure 4-1-1-7. Potentiodynamic polarization curves for Ti, Ti_3Al, $Ti_3Al_{(m)}$+TiAl, Ti_3Al+$TiAl_{(m)}$, TiAl, $TiAl_3$ and Al in NaOH+Na_2SO_4.

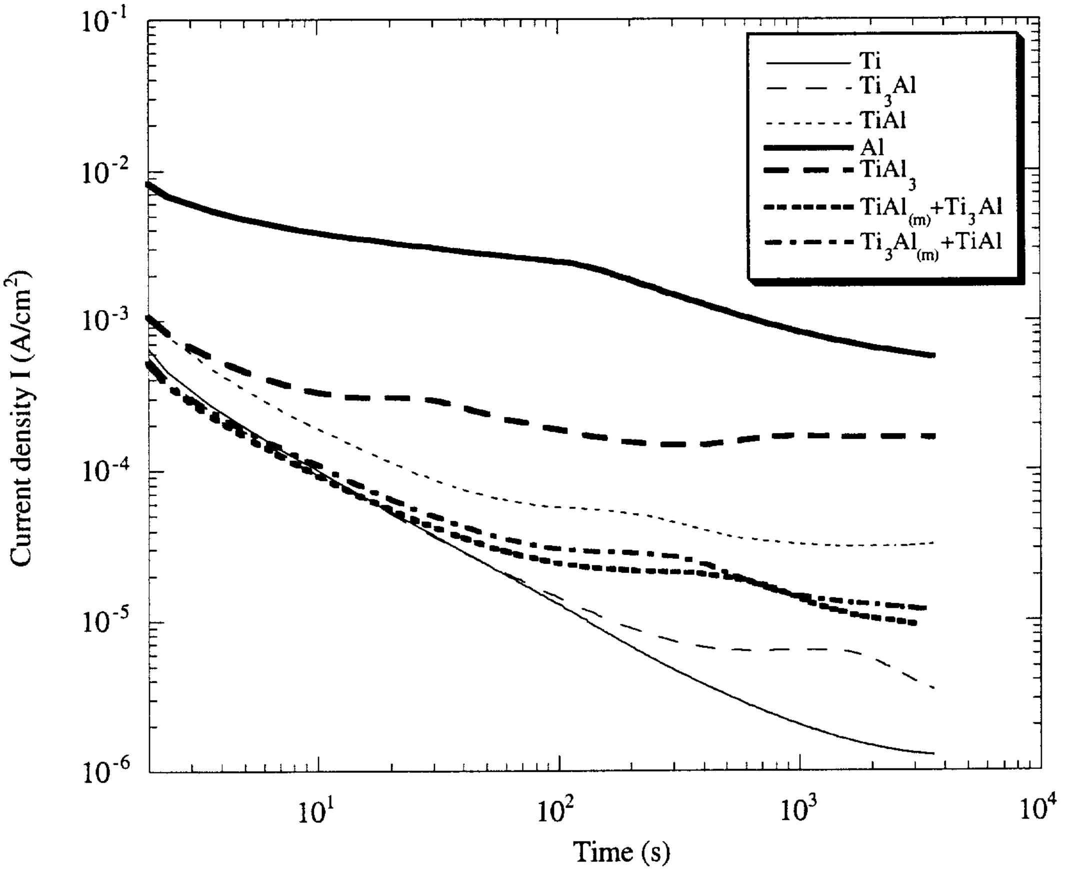

Figure 4-1-2-1. Potentiostatic polarization curves for Ti, Ti_3Al, TiAl, $Ti_3Al+TiAl_{(m)}$, $Ti_3Al_{(m)}+TiAl$, $TiAl_3$ and Al in H_2SO_4.

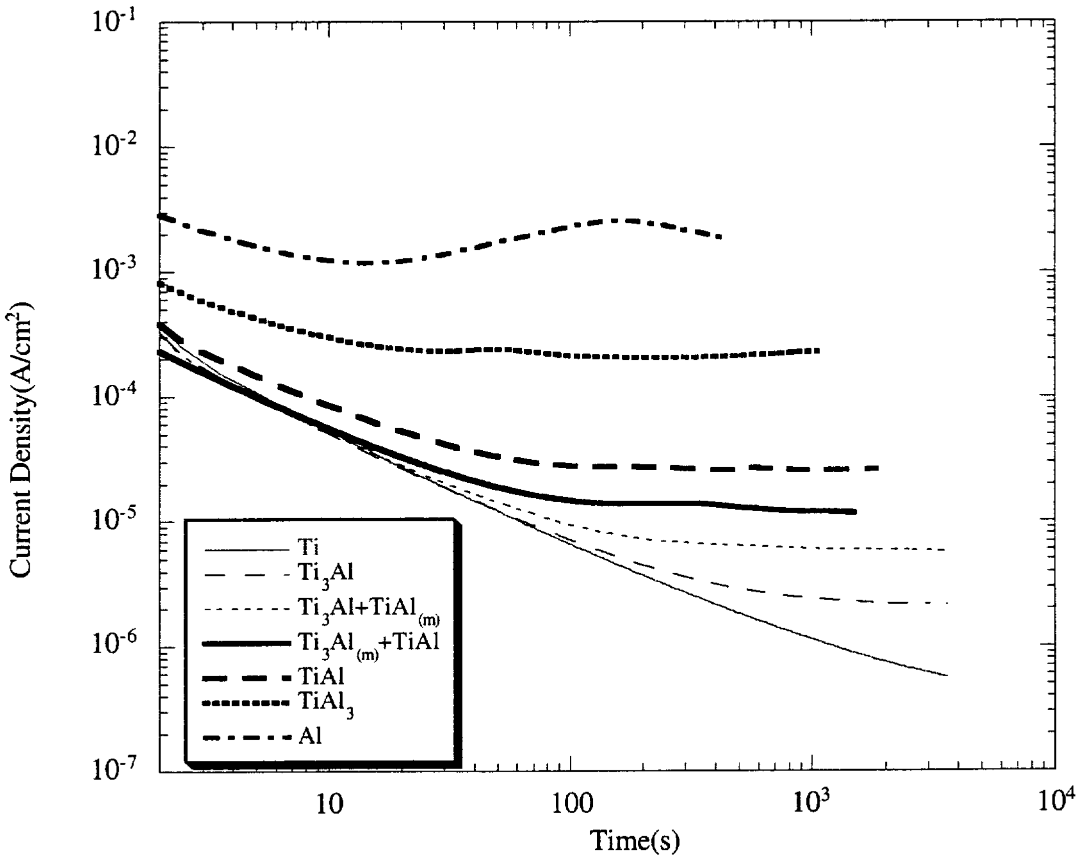

Figure 4-1-2-2. Potentiostatic polarization curves for Ti, Ti_3Al, TiAl, $Ti_3Al+TiAl_{(m)}$, $Ti_3Al_{(m)}+TiAl$, $TiAl_3$ and Al in HNO_3.

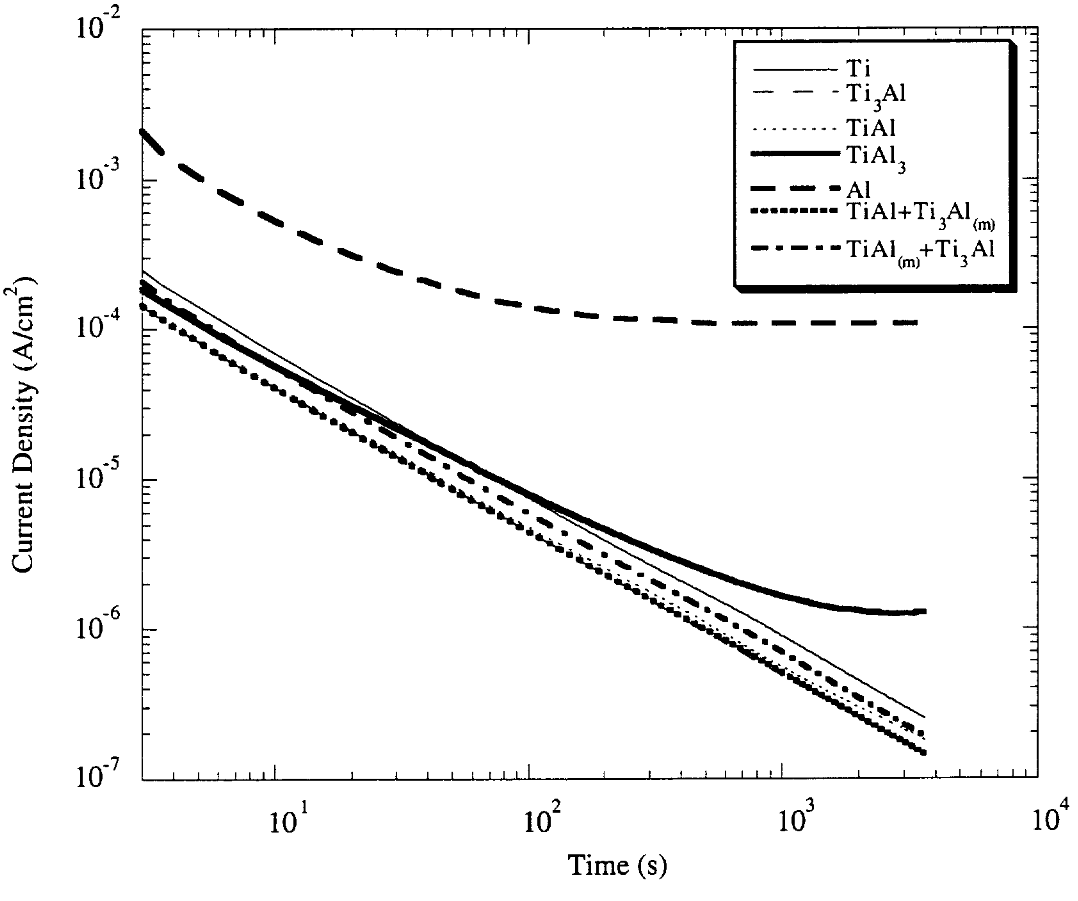

Figure 4-1-2-3. Potentiostatic polarization curves for Ti, Ti_3Al, TiAl, Ti_3Al+$TiAl_{(m)}$, $Ti_3Al_{(m)}$+TiAl, $TiAl_3$ and Al in Na_2SO_4.

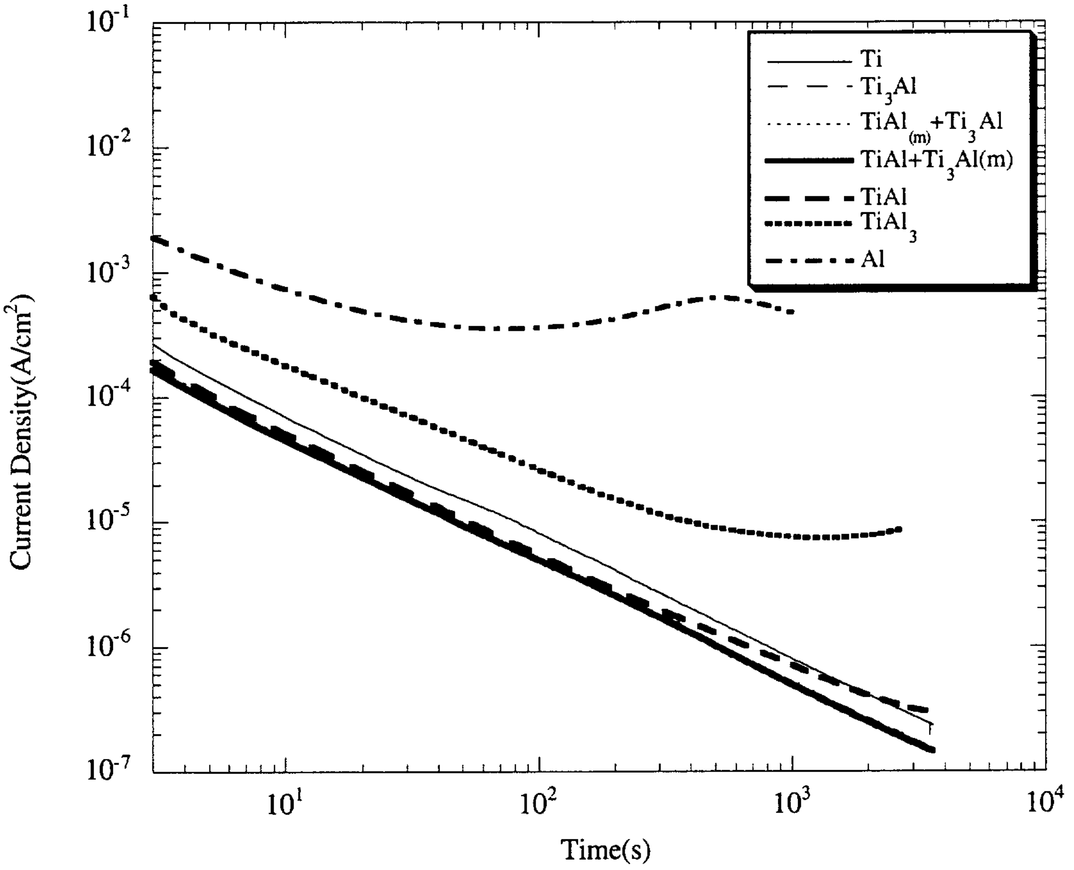

Figure 4-1-2-4. Potentiostatic polarization curves for Ti, Ti_3Al, TiAl, $Ti_3Al+TiAl_{(m)}$, $Ti_3Al_{(m)}+TiAl$, $TiAl_3$ and Al in $NaNO_3$.

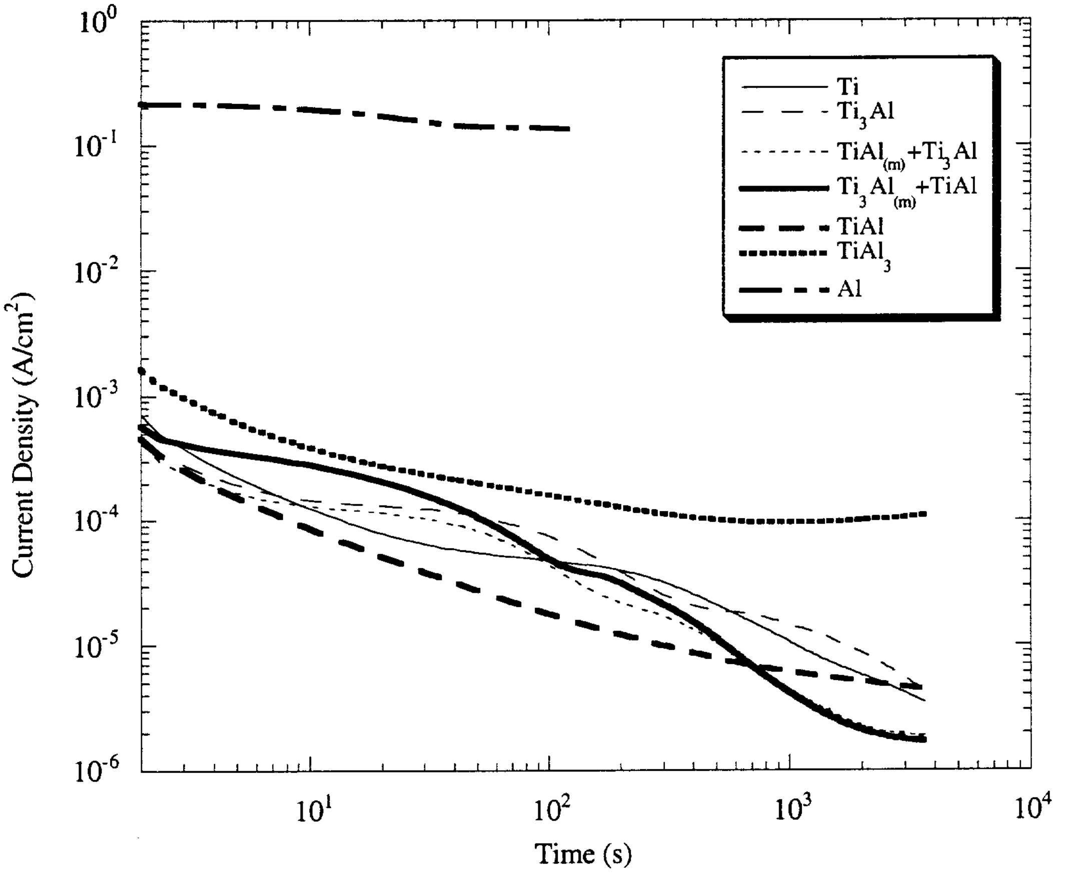

Figure 4-1-2-5. Potentiostatic polarization curves for Ti, Ti_3Al, TiAl, $Ti_3Al+TiAl_{(m)}$, $Ti_3Al_{(m)}+TiAl$, $TiAl_3$ and Al in NaOH.

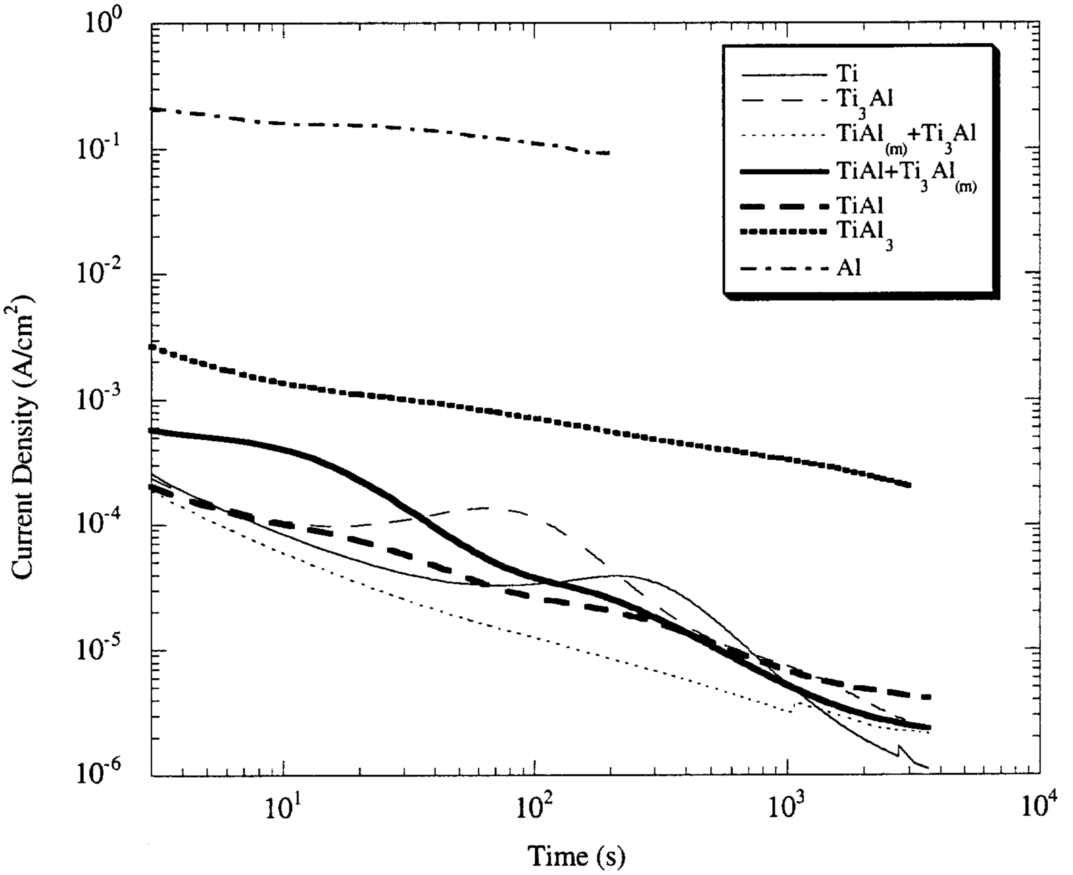

Figure 4-1-2-6. Potentiostatic polarization curves for Ti, Ti_3Al, TiAl, $Ti_3Al+TiAl_{(m)}$, $Ti_3Al_{(m)}+TiAl$, $TiAl_3$ and Al in $NaOH+Na_2SO_4$.

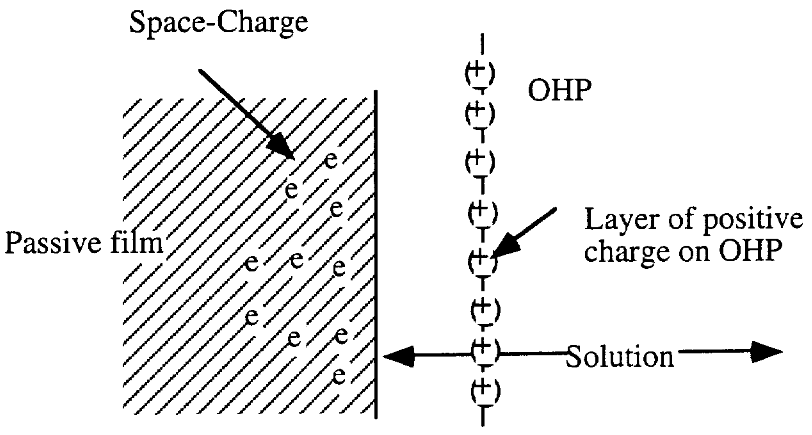

Figure 4-1-3-1. Schematic representation of the surface charge at the space charge region and the Outer Helmholtz Plane (OHP).

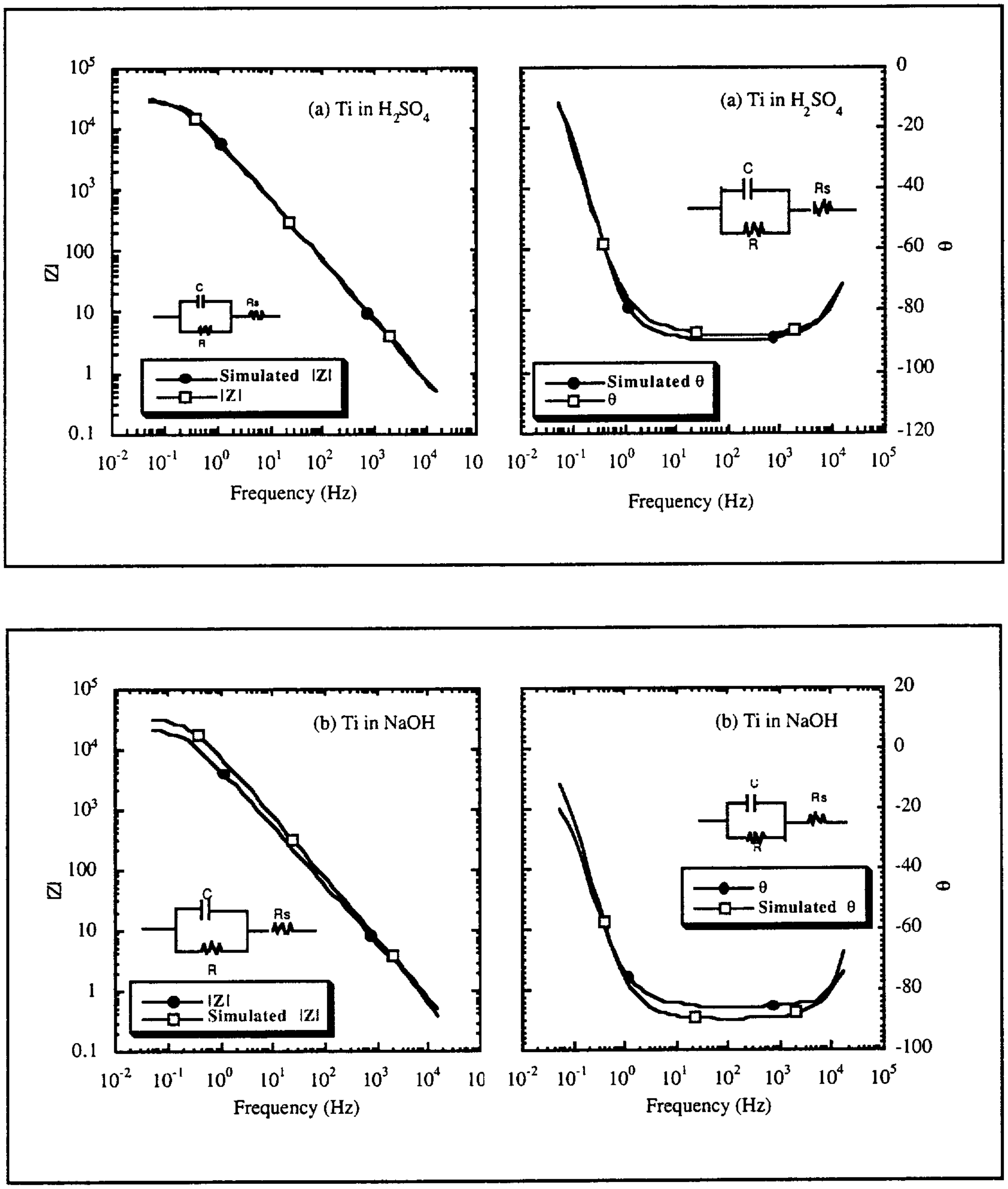

Figure 4-1-3-2. Bode diagrams of the EIS experimental and simulation results for Ti. (a)H_2SO_4, (b)NaOH

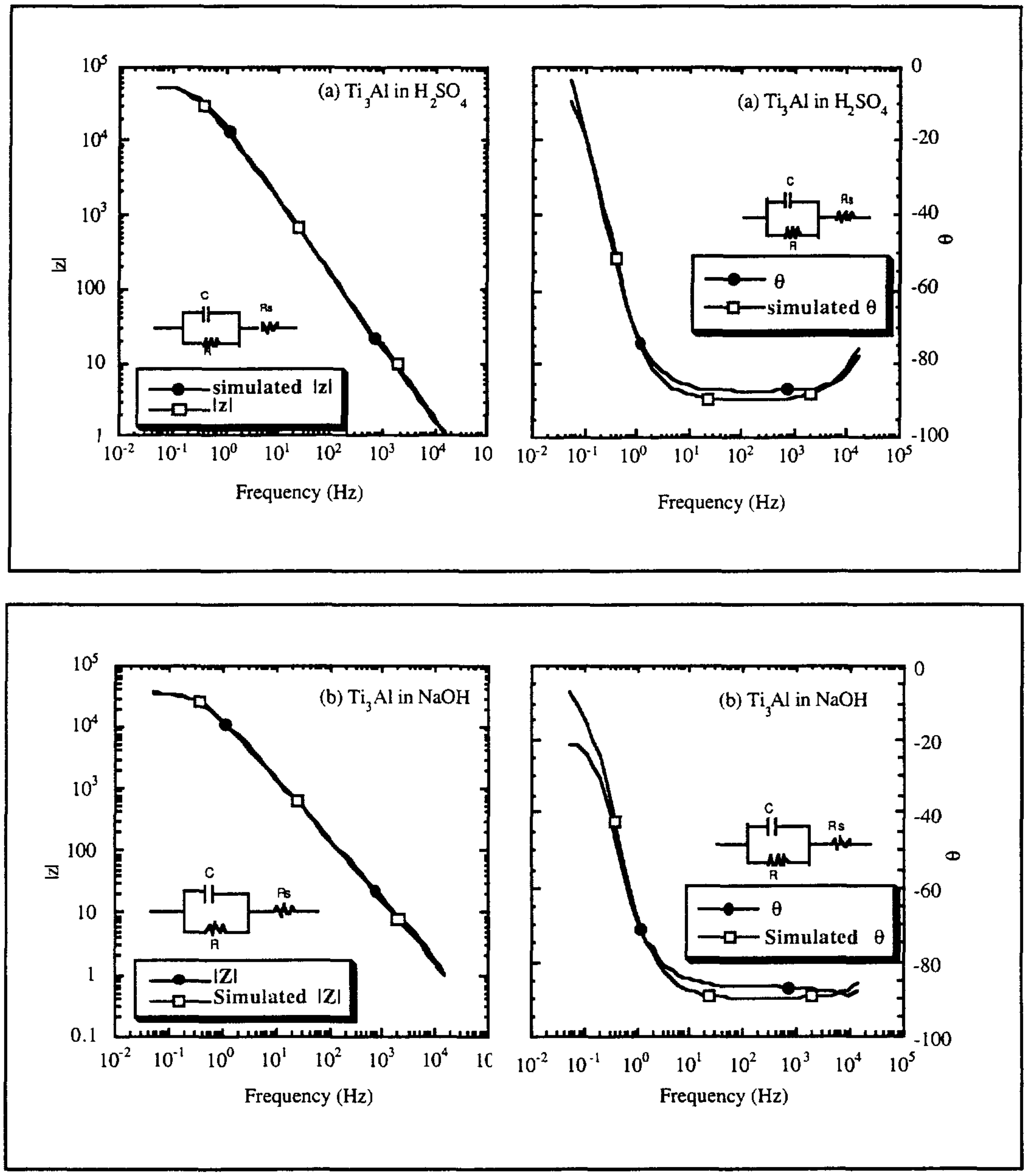

Figure 4-1-3-3. Bode diagrams of the EIS experimental and simulation results for Ti_3Al. (a)H_2SO_4, (b)NaOH

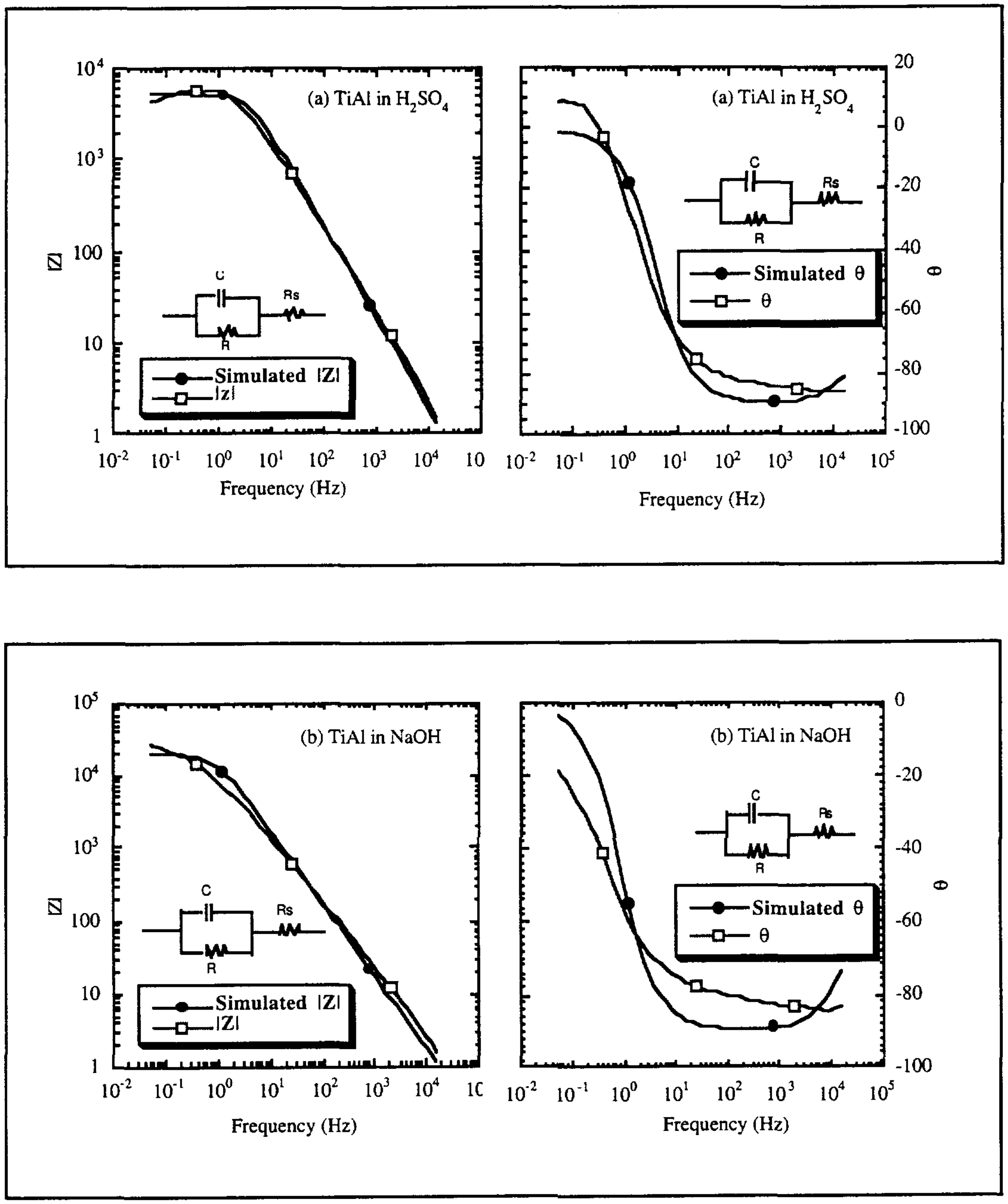

Figure 4-1-3-4. Bode diagrams of the EIS experimental and simulation results for TiAl. (a)H_2SO_4, (b)NaOH

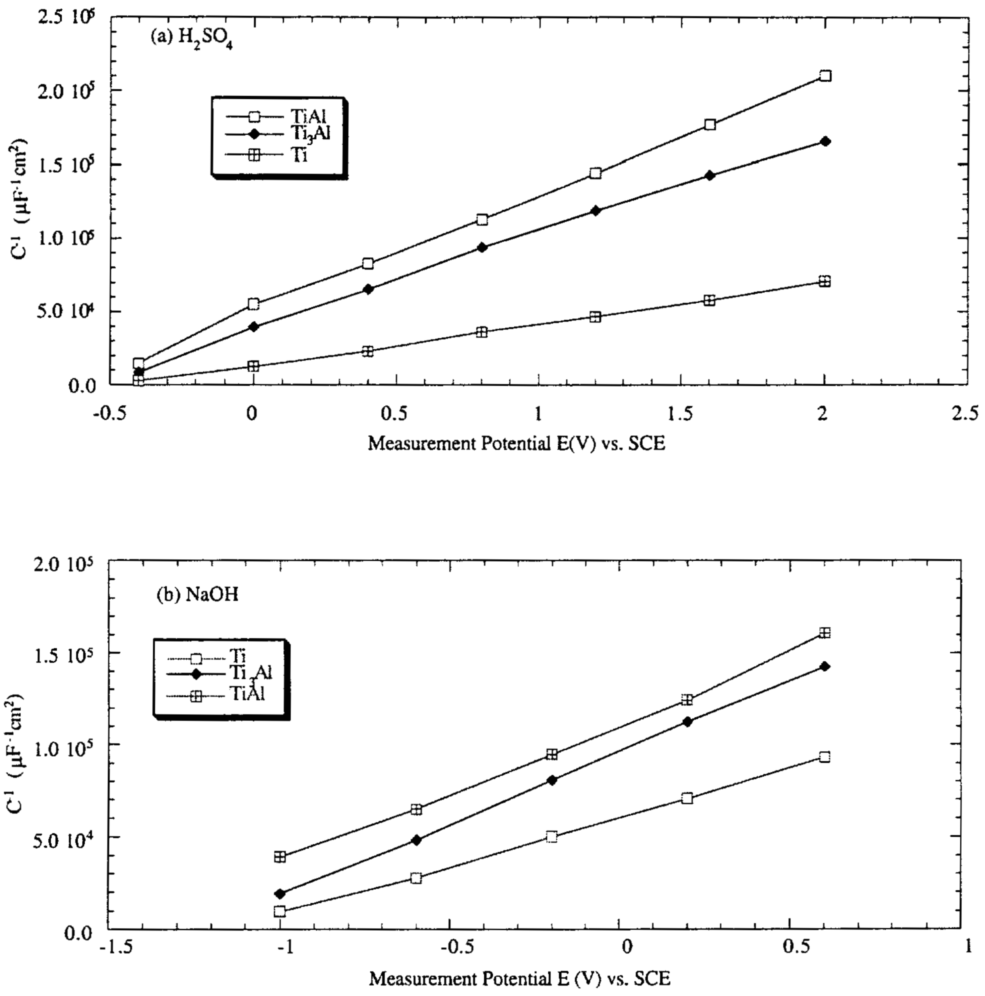

Figure 4-1-3-5. Relation between the reciprocal capacitance and measured potentials for Ti, Ti_3Al and TiAl. (a) H_2SO_4 and (b) NaOH

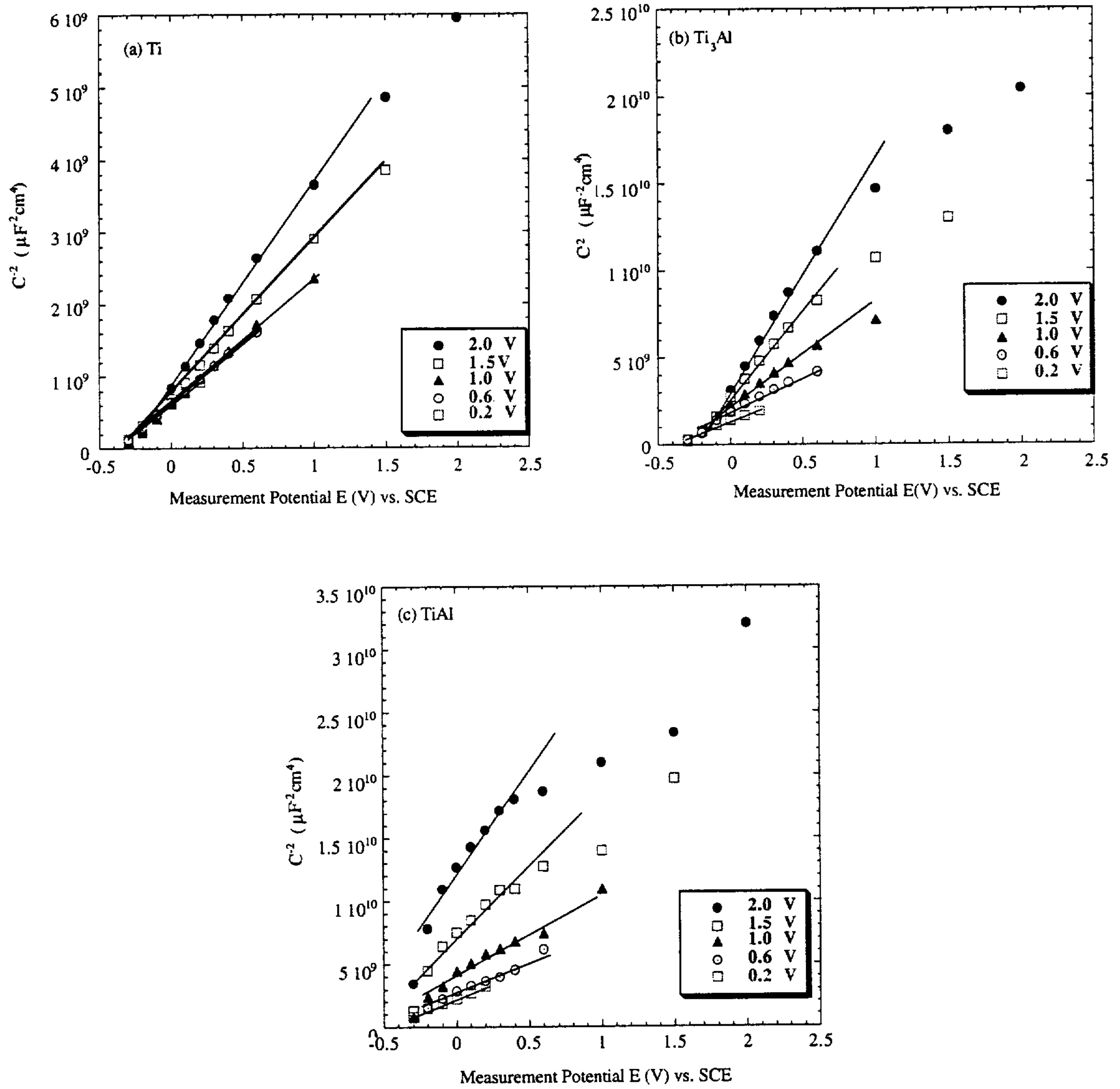

Figure 4-1-3-6. Mott-Schottky plots for passive films formed at different potentials in H_2SO_4. (a) Ti (b) Ti_3Al (c) TiAl

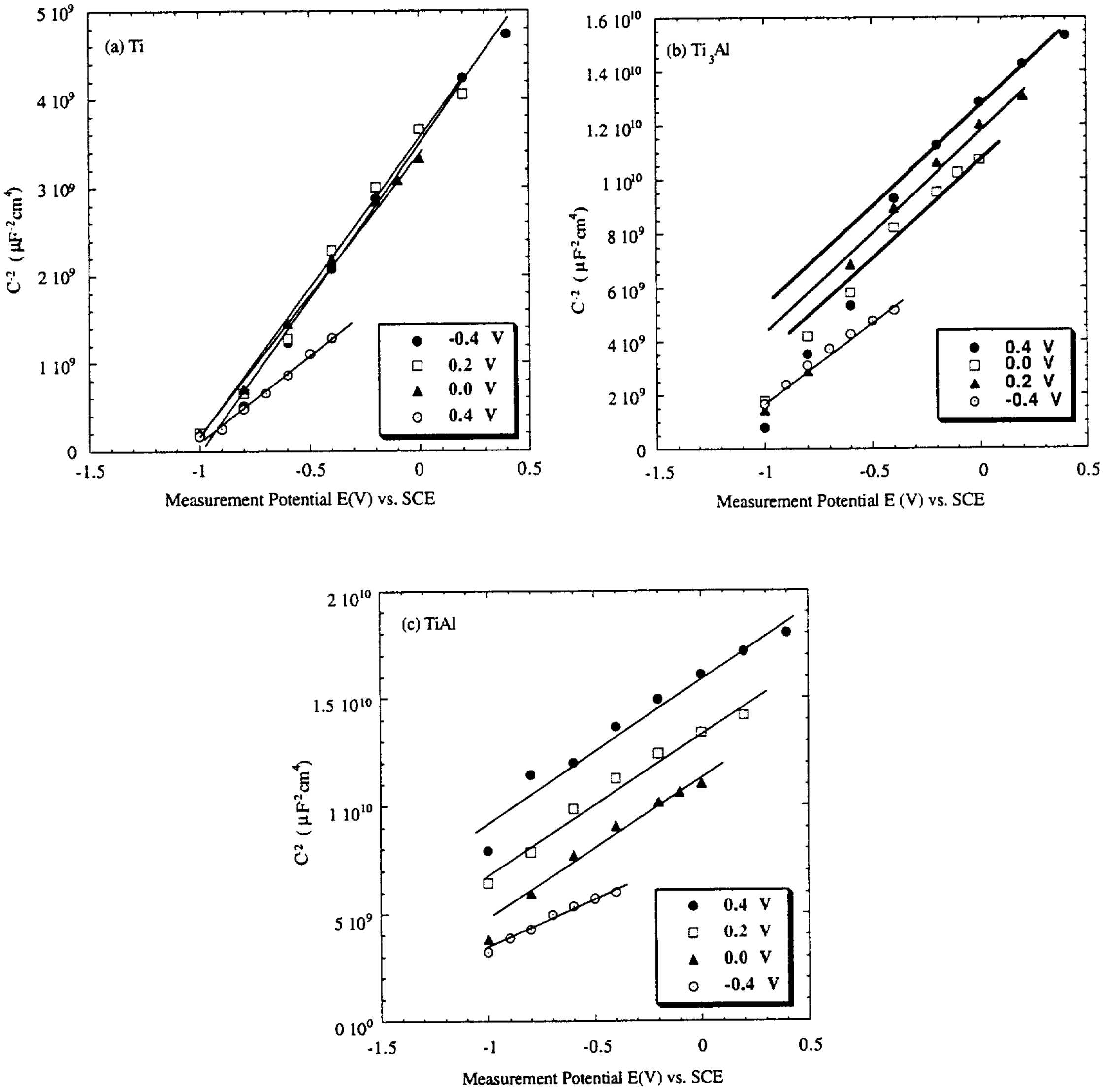

Figure 4-1-3-7. Mott-Schottky plots for passive films formed at different potentials in NaOH. (a) Ti, (b) Ti$_3$Al, (c) TiAl

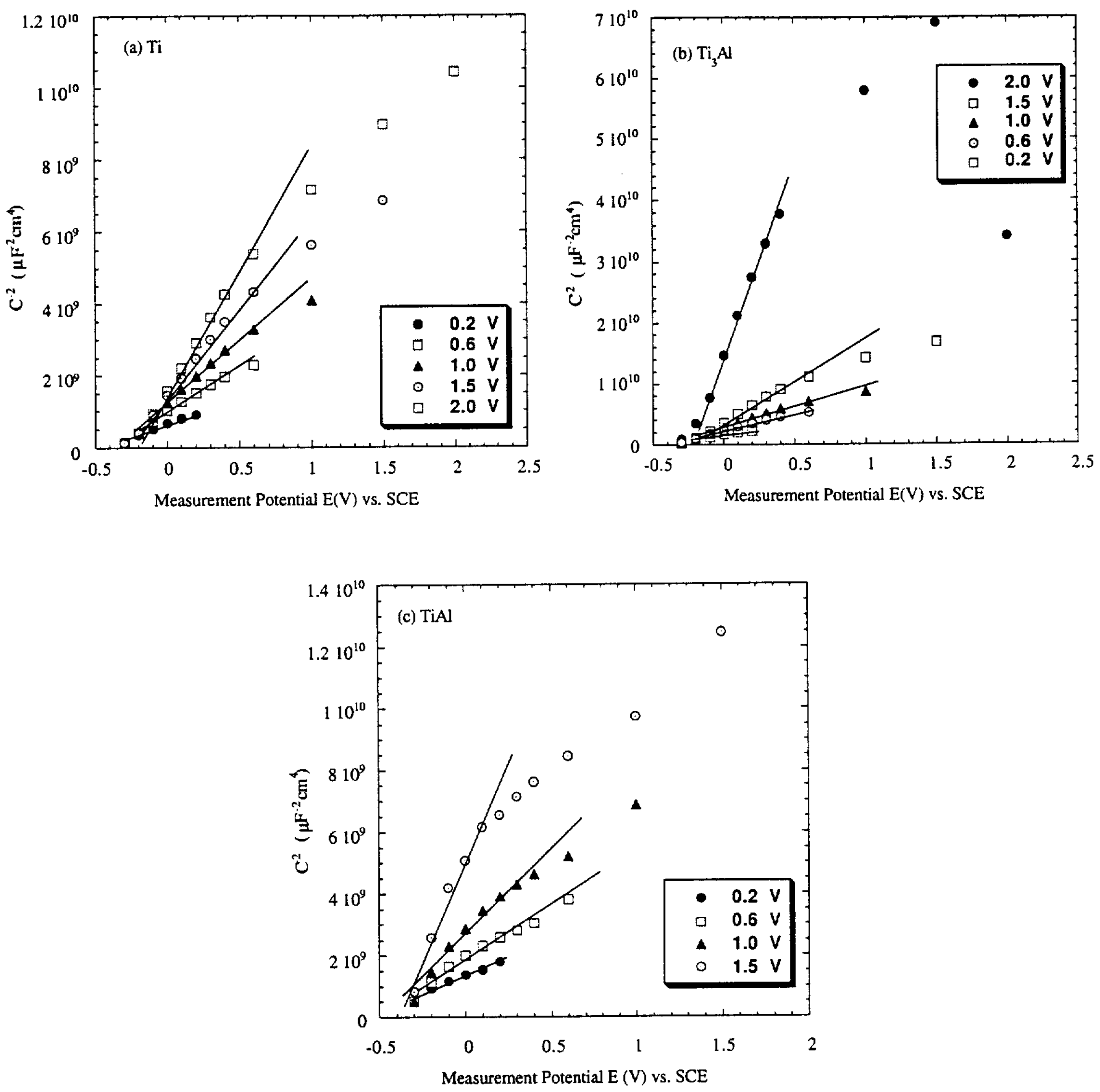

Figure 4-1-3-8. Mott-Schottky plots for passive films formed at different potentials in HNO_3. (a) Ti, (b) Ti_3Al, (c) TiAl

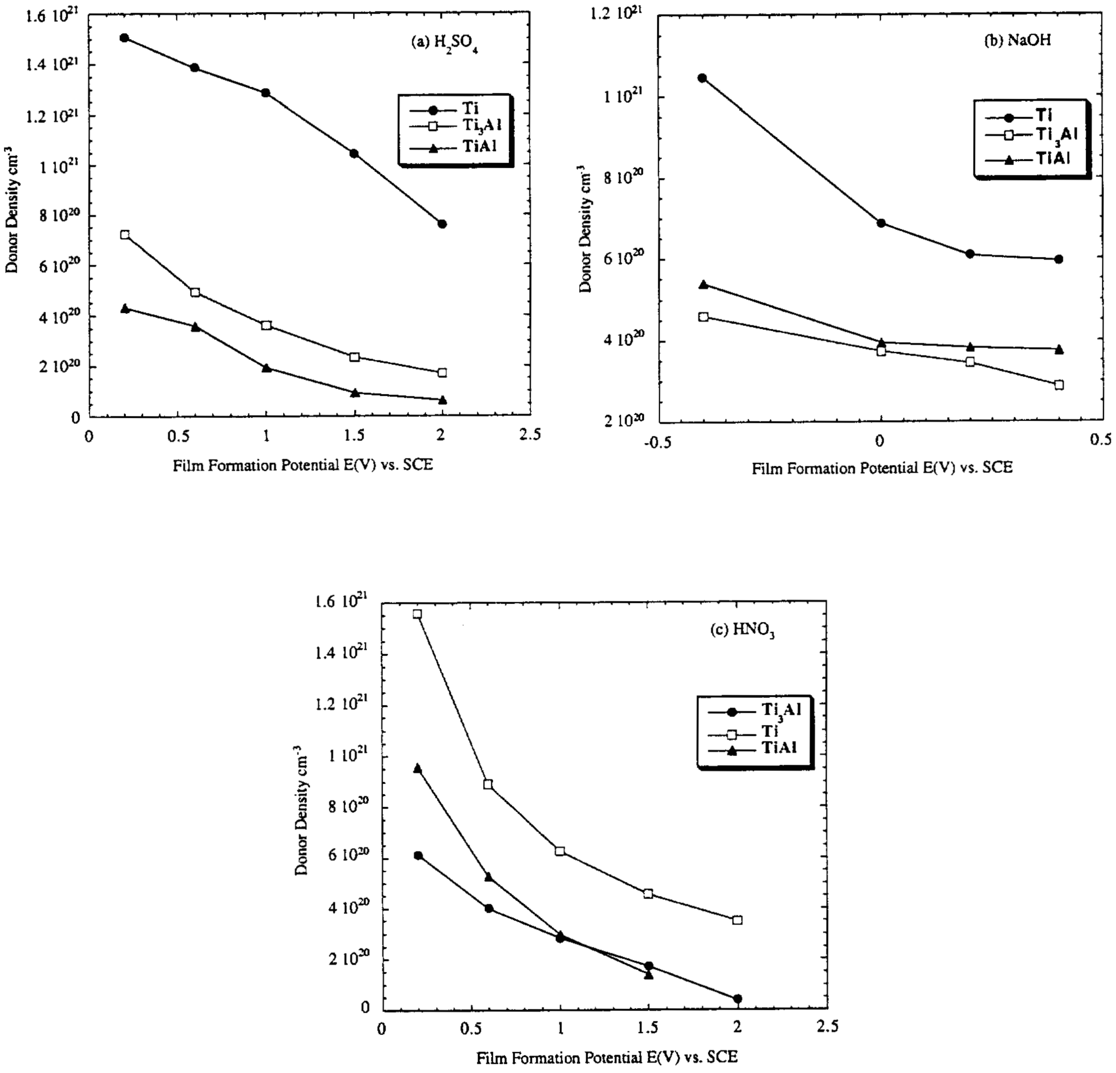

Figure 4-1-3-9. Donor densities for Ti, Ti_3Al and TiAl passive films formed in different solutions. (a) H_2SO_4, (b) NaOH and, (c) HNO_3

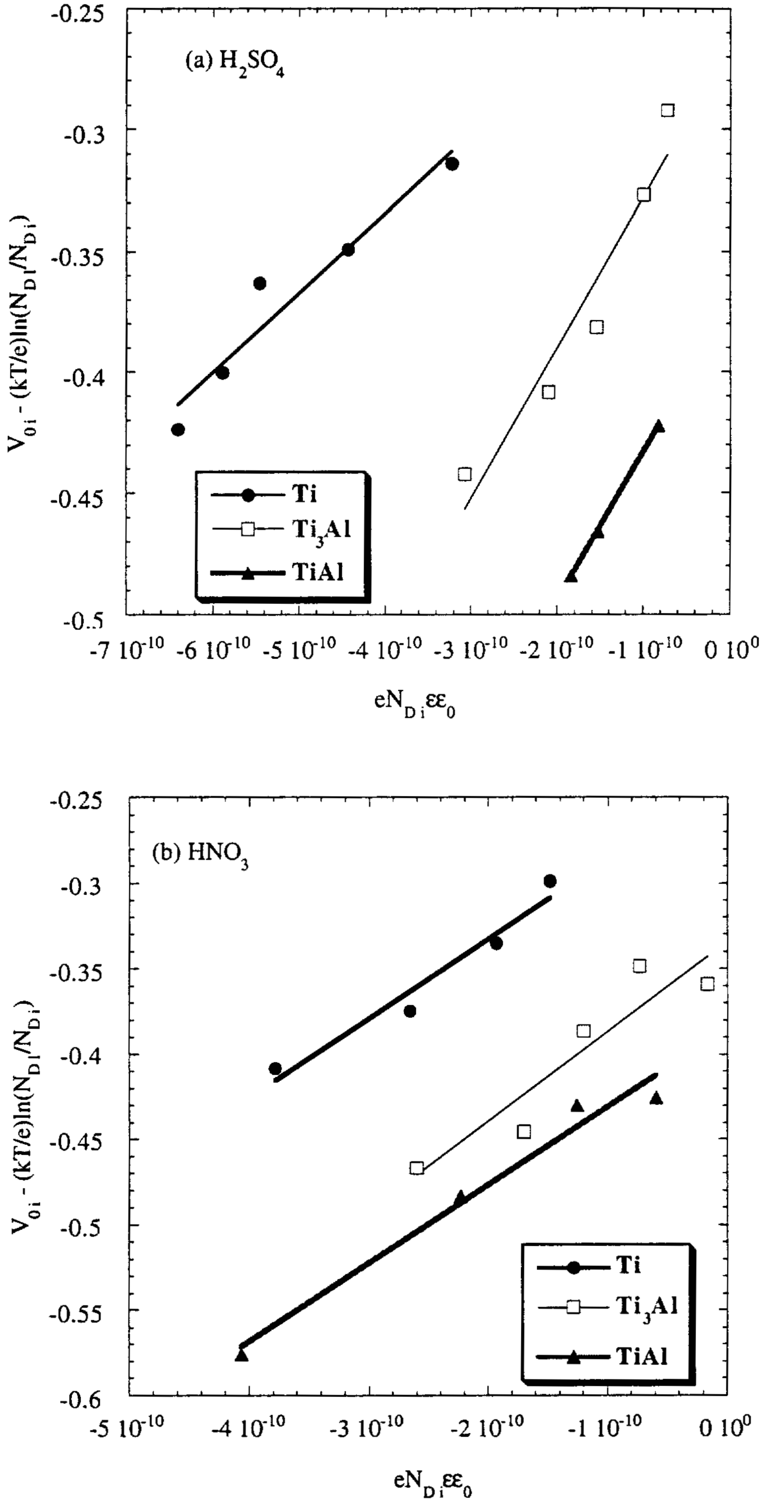

Figure 4-1-3-10. Fonseca plot for Ti, Ti_3Al and TiAl in acidic solutions.
(a) H_2SO_4 and (b) HNO_3

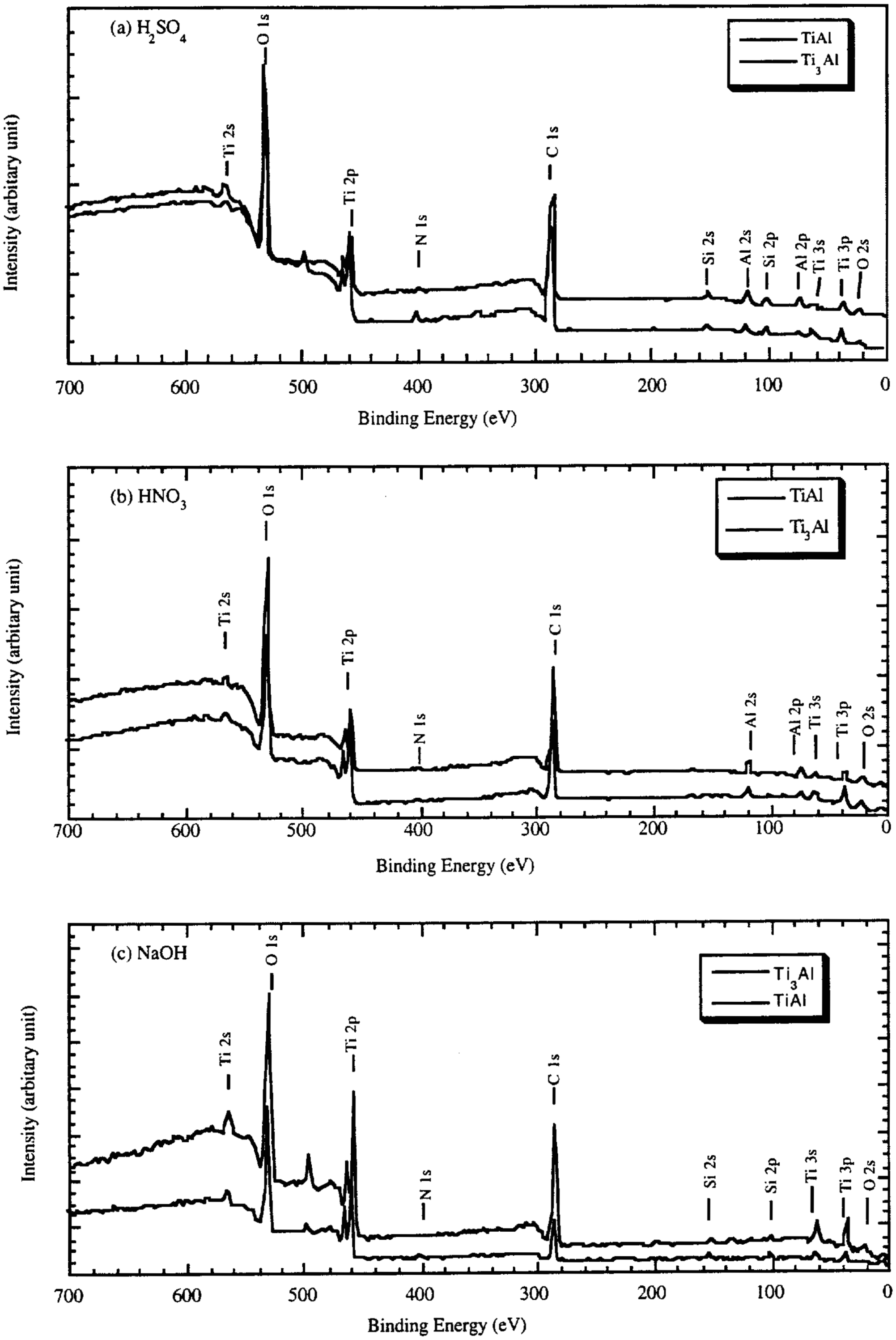

Figure 4-2-1. XPS survey spectra for Ti_3Al and TiAl in different solutions. (a) H_2SO_4, (b) HNO_3, and (c) NaOH

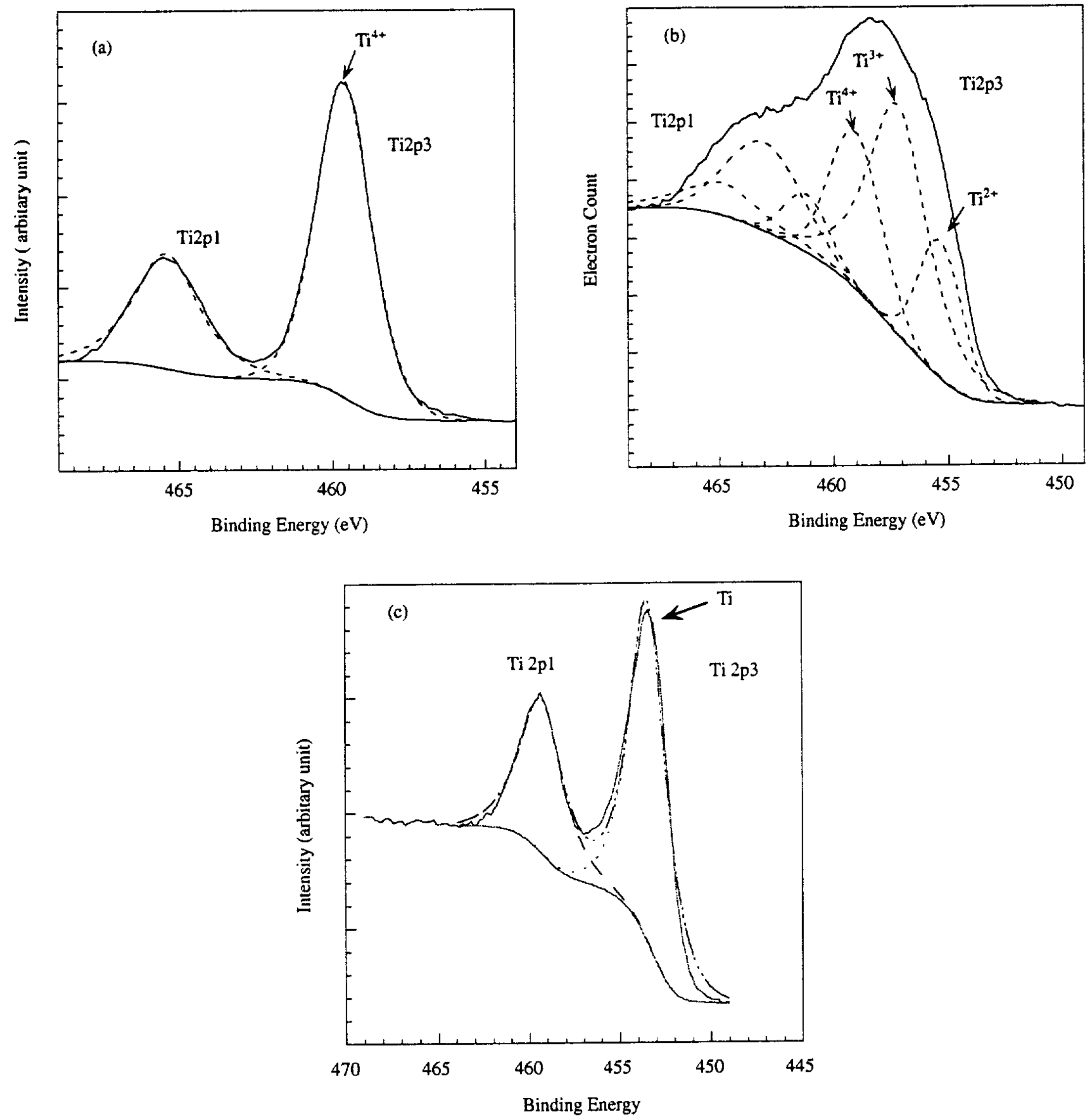

Figure 4-2-2. Typical high-resolution XPS spectra of Ti with increasing depth from the surface. (a) topmost surface, (b) after several cycles of Ar^+ sputtering, and (c) after 20 cycles of Ar^+ sputtering

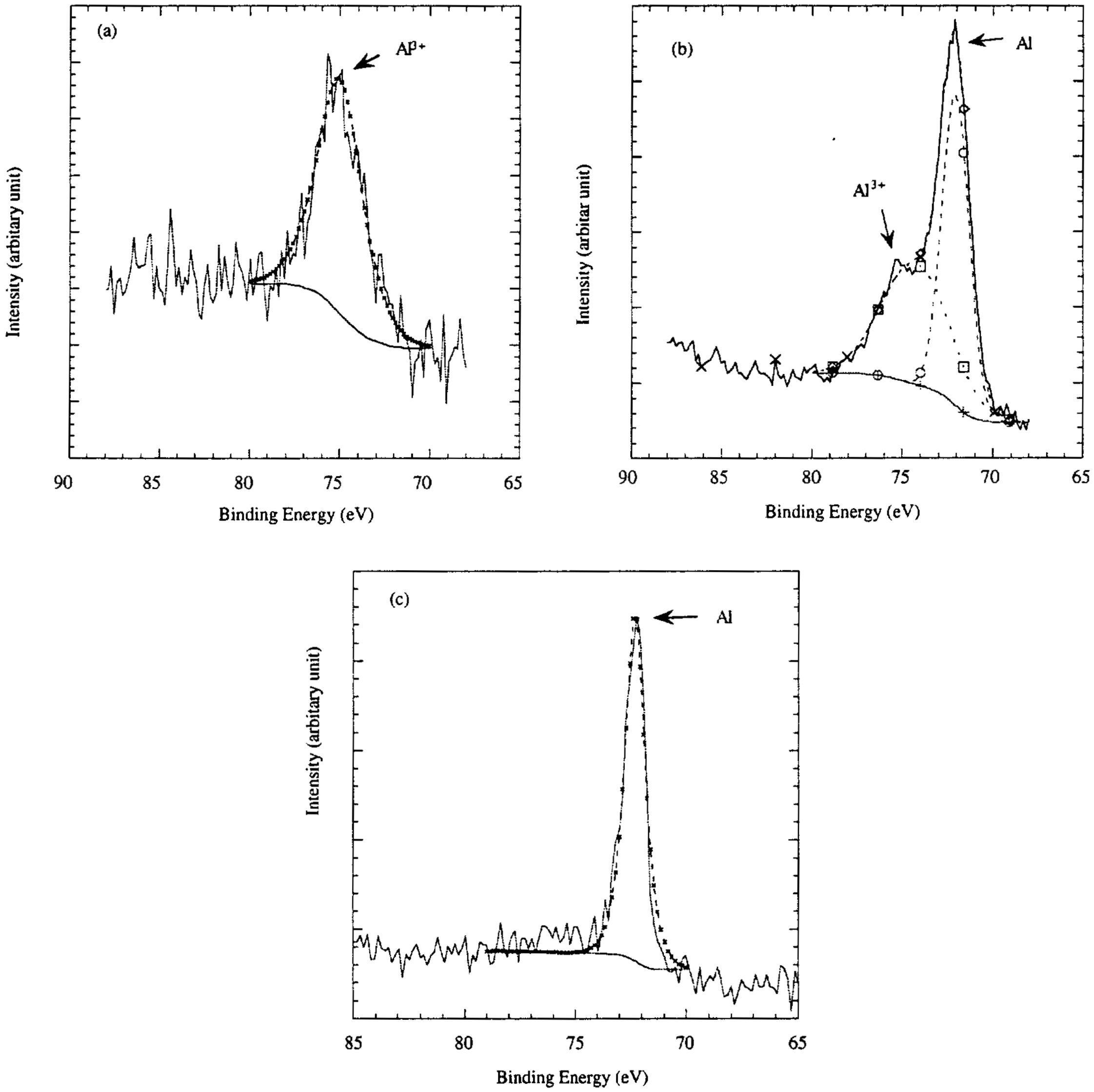

Figure 4-2-3. Typical high-resolution XPS spectra of Al with increasing depth from the surface. (a) topmost surface, (b) after several cycles of Ar^+ sputtering, and (c) after 20 cycles of Ar^+ sputtering

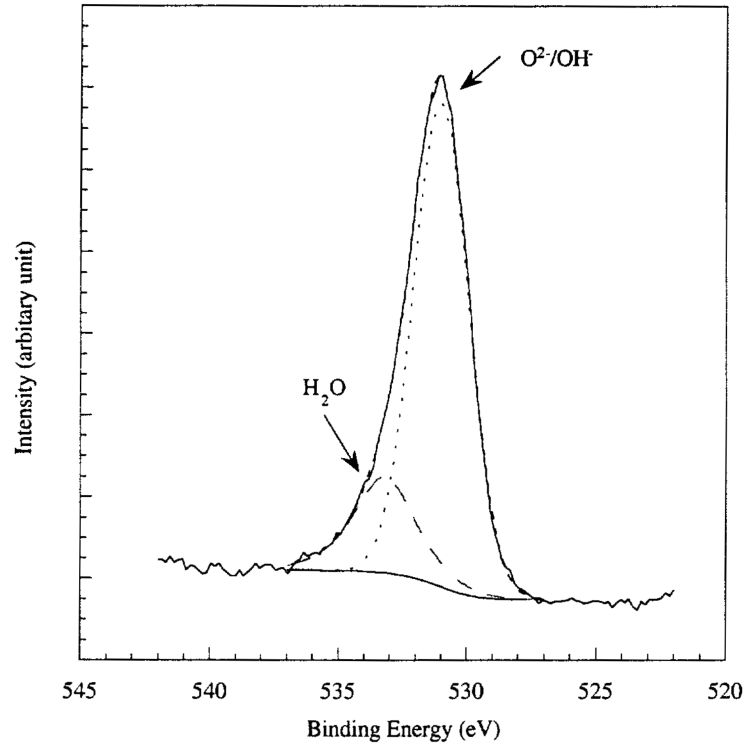

Figure 4-2-4. Typical high-resolution XPS spectra of O.

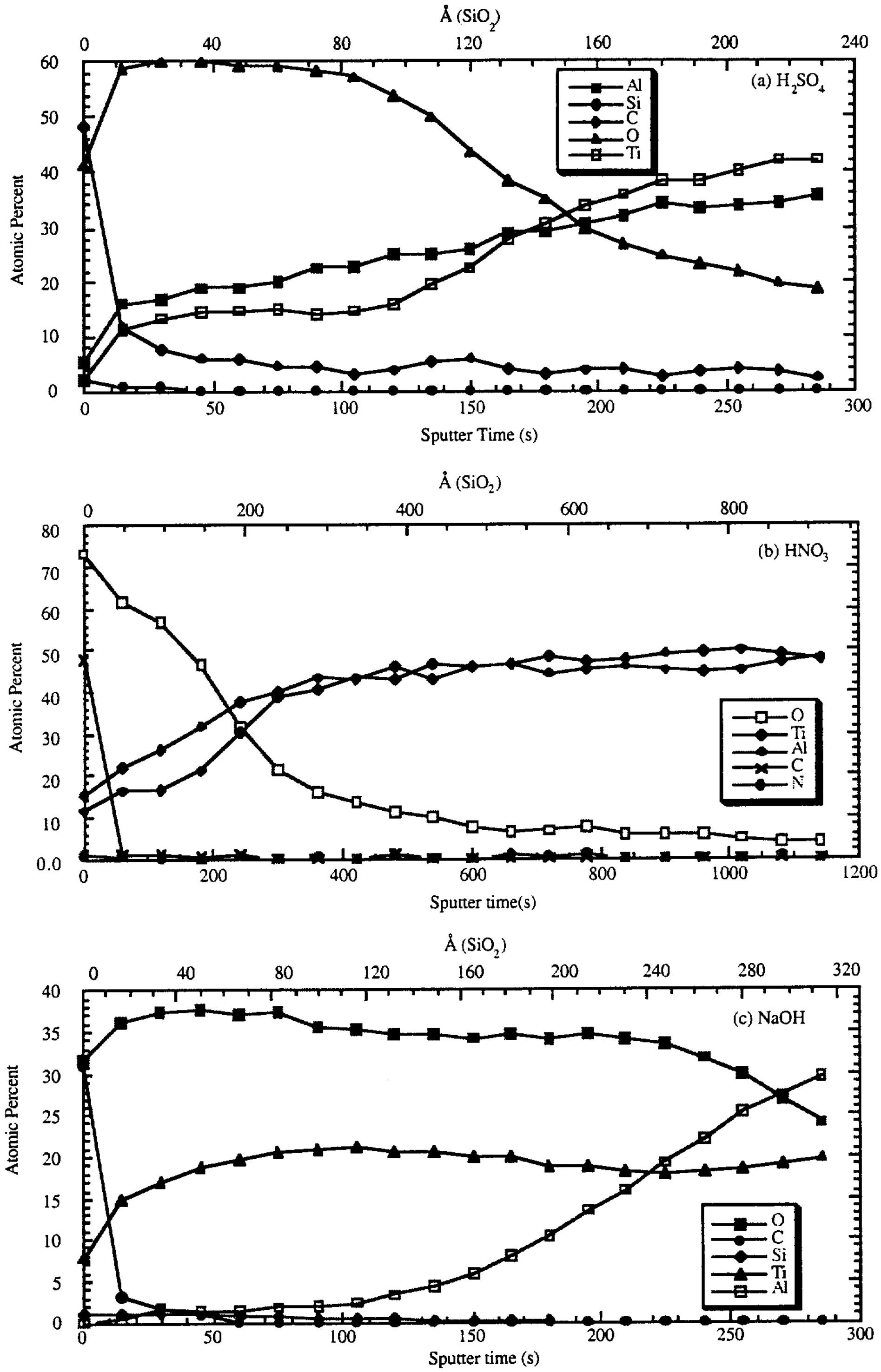

Figure 4-2-5. Original depth profiles for TiAl passive films formed in different solutions. (a) H_2SO_4, (b) HNO_3, and (c) NaOH

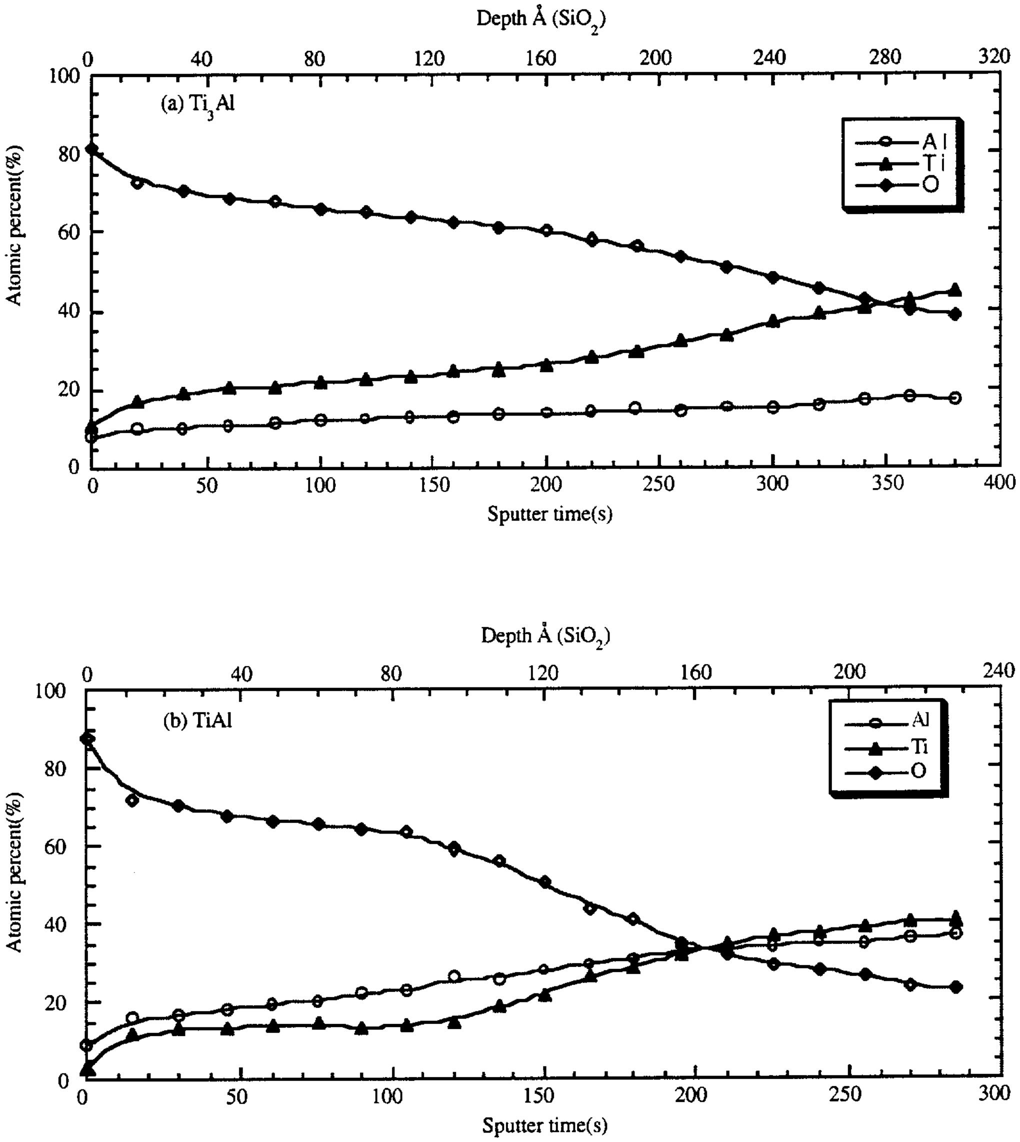

Figure 4-2-6. Depth profiles of Ti, Al and O for passive films formed in H_2SO_4.
(a) Ti_3Al and (b) TiAl

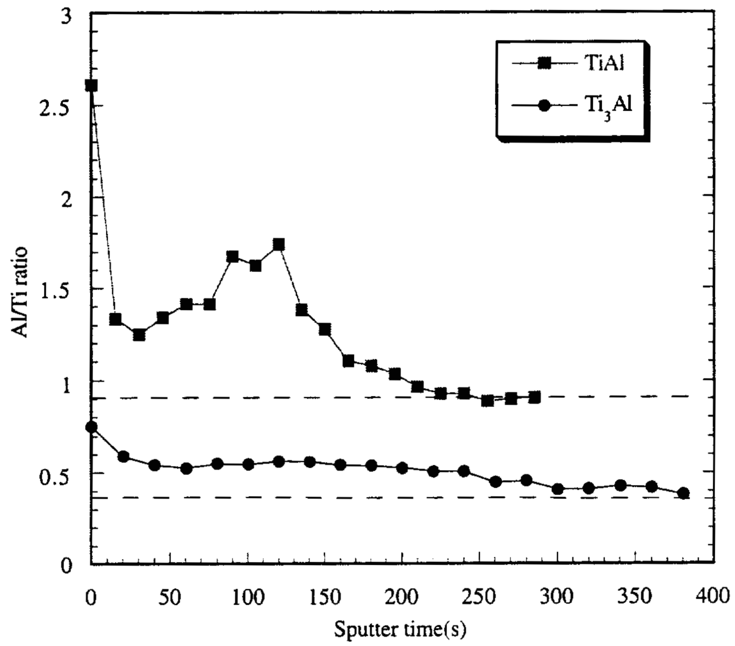

Figure 4-2-7. Depth profiles of Al/Ti ratios for Ti_3Al and TiAl in H_2SO_4.

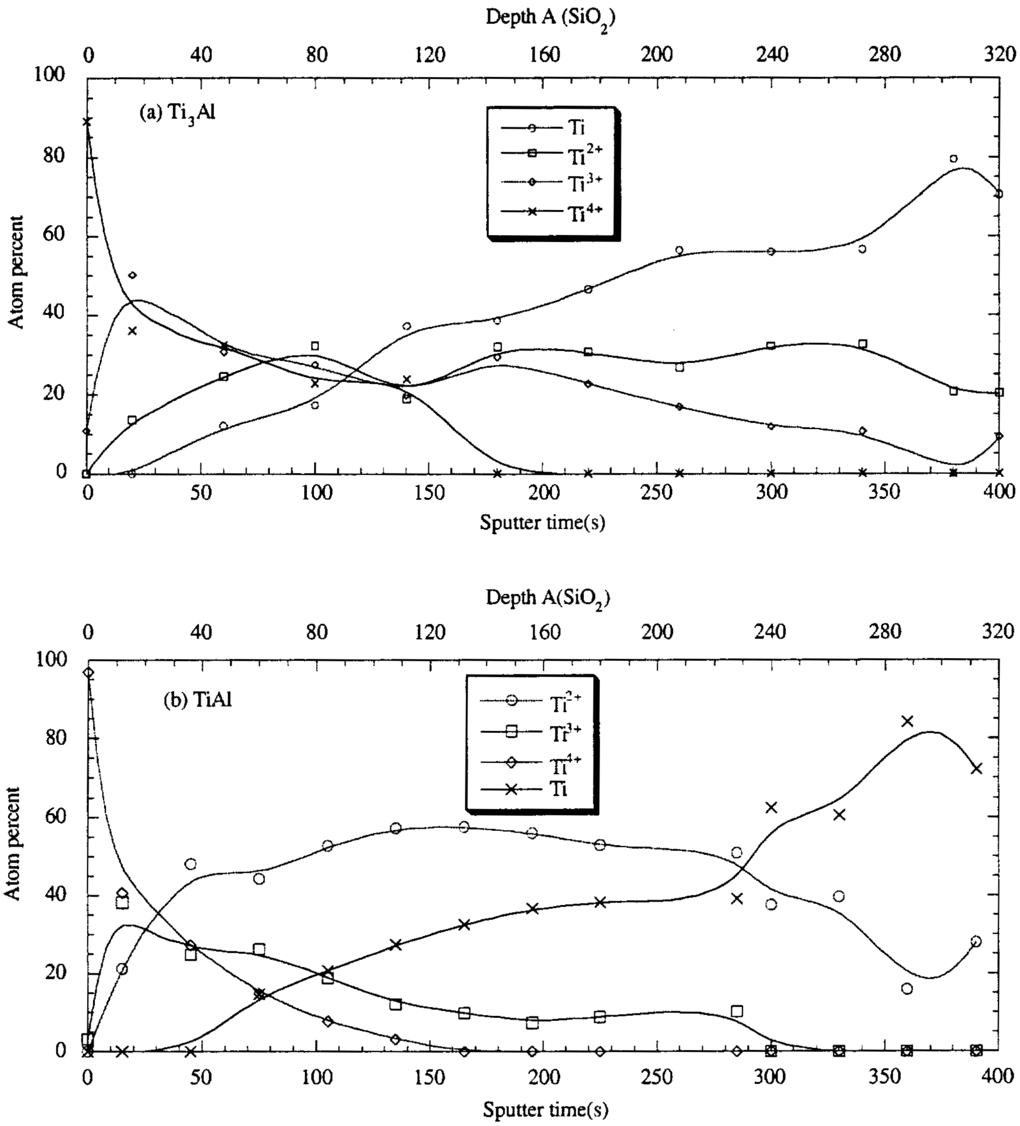

Figure 4-2-8. Depth profiles of different chemical states of Ti for passive films formed in H_2SO_4. (a) Ti_3Al and (b) TiAl

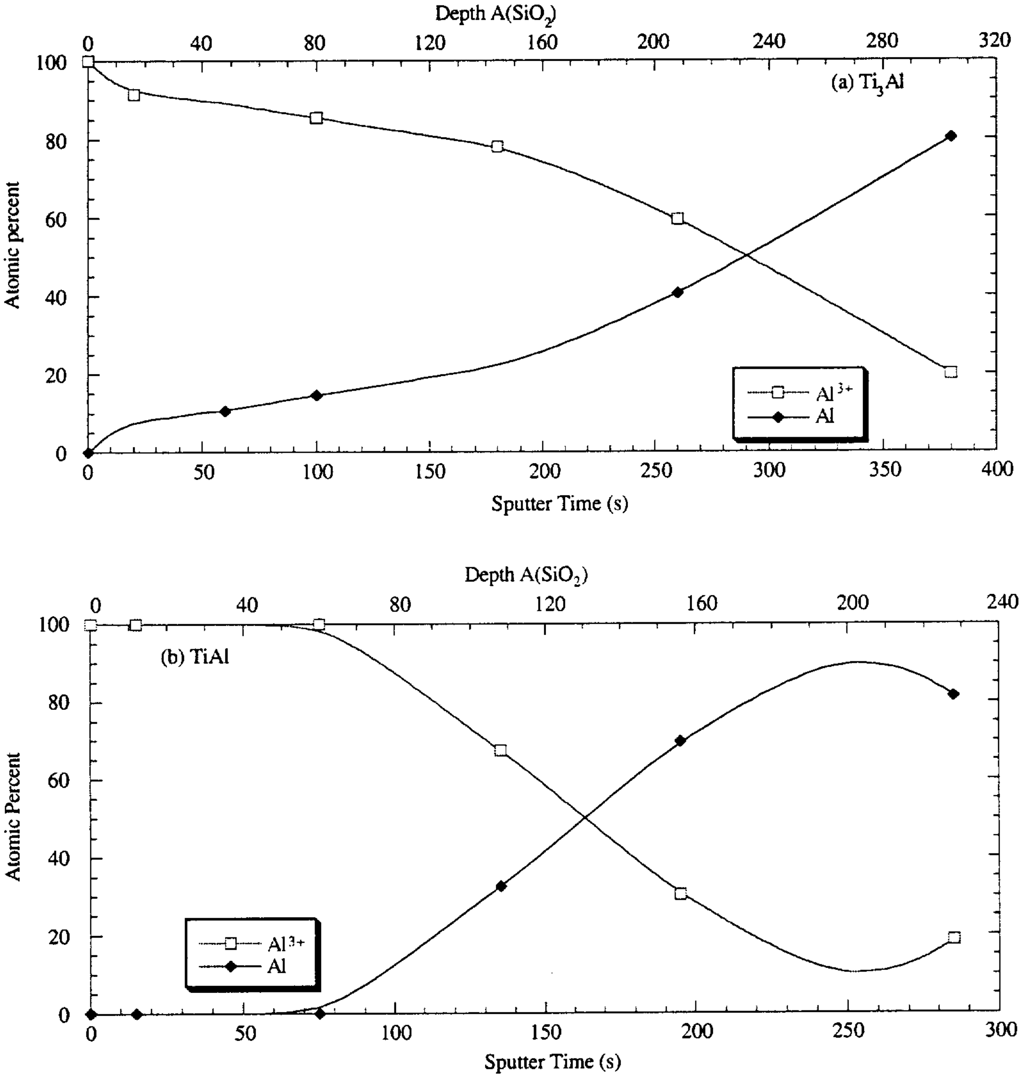

Figure 4-2-9. Depth profiles of different chemical states of Al for passive films formed in H_2SO_4. (a) Ti_3Al and (b) TiAl

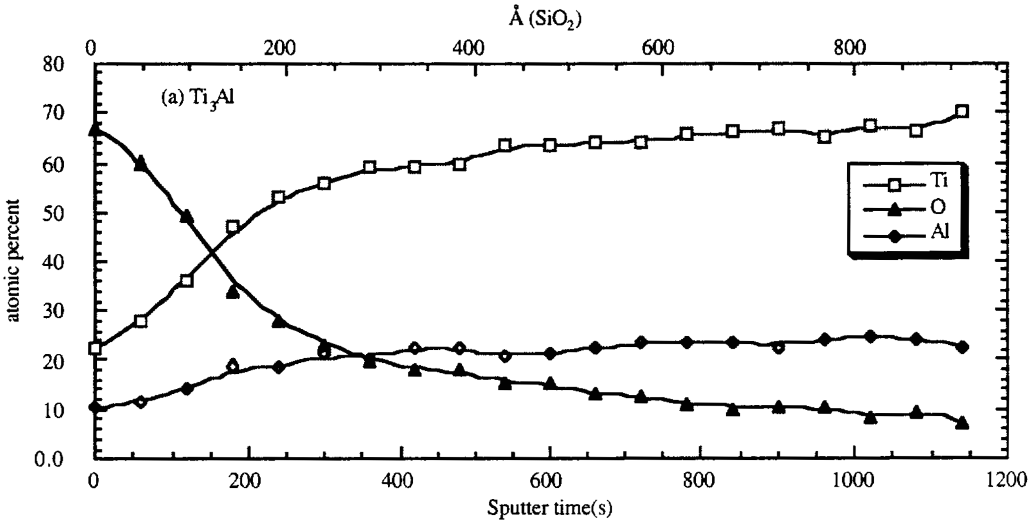

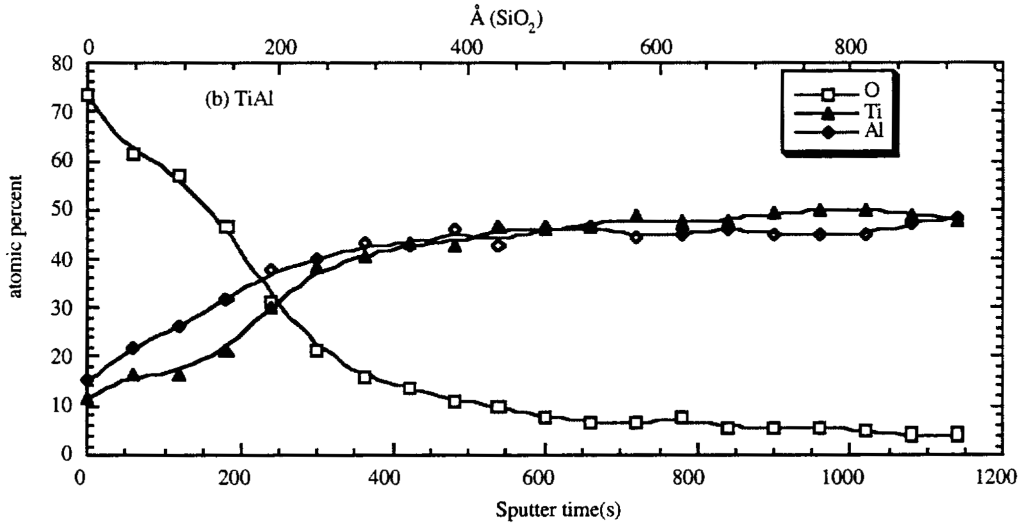

Figure 4-2-10. Depth profiles of Ti, Al and O for passive films formed in HNO_3.
(a) Ti_3Al and (b) TiAl

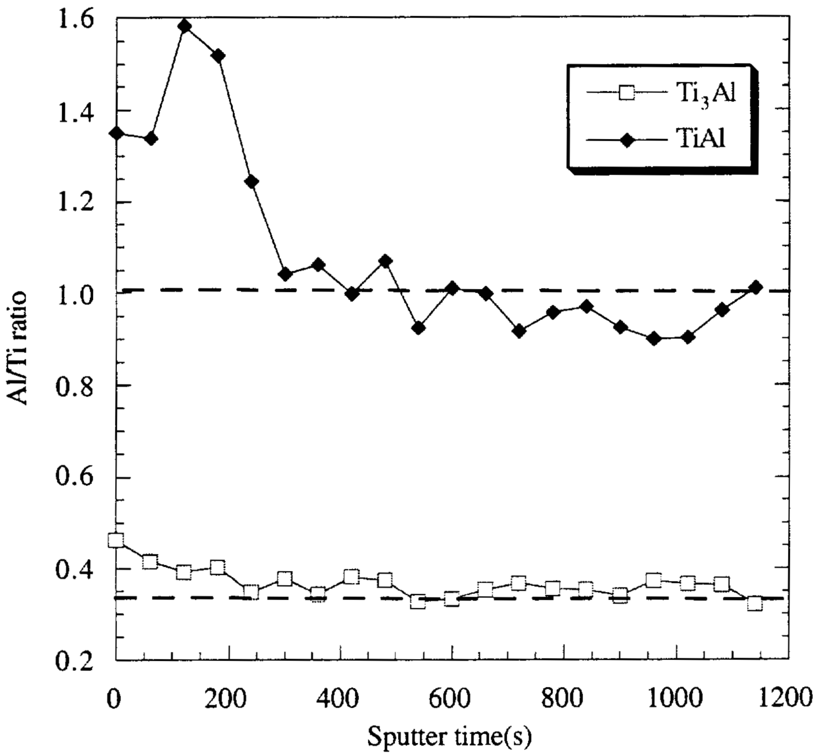

Figure 4-2-11. Depth profiles of Al/Ti ratios for Ti_3Al and TiAl in HNO_3.

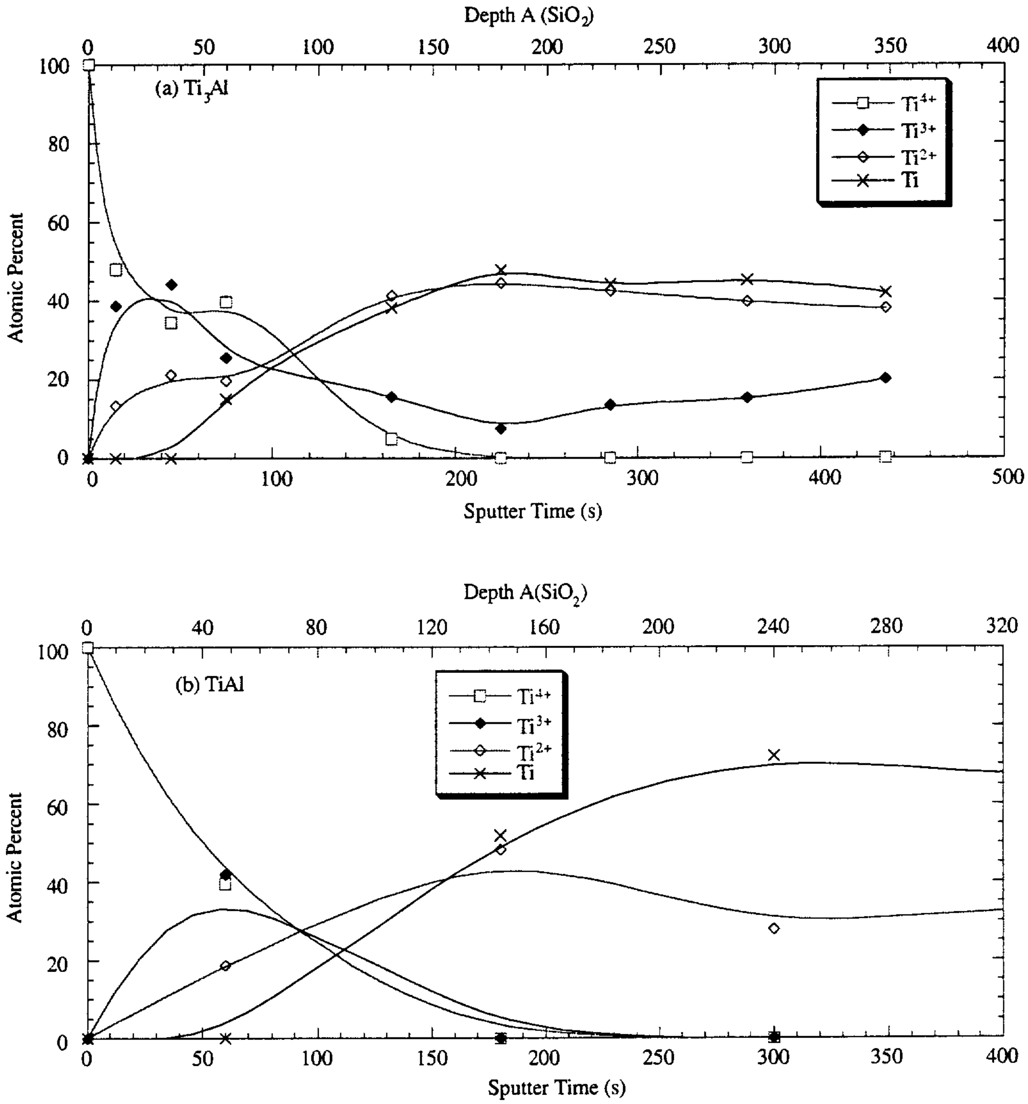

Figure 4-2-12. Depth profiles of different chemical states of Ti for passive films formed in HNO_3. (a) Ti_3Al and (b) TiAl

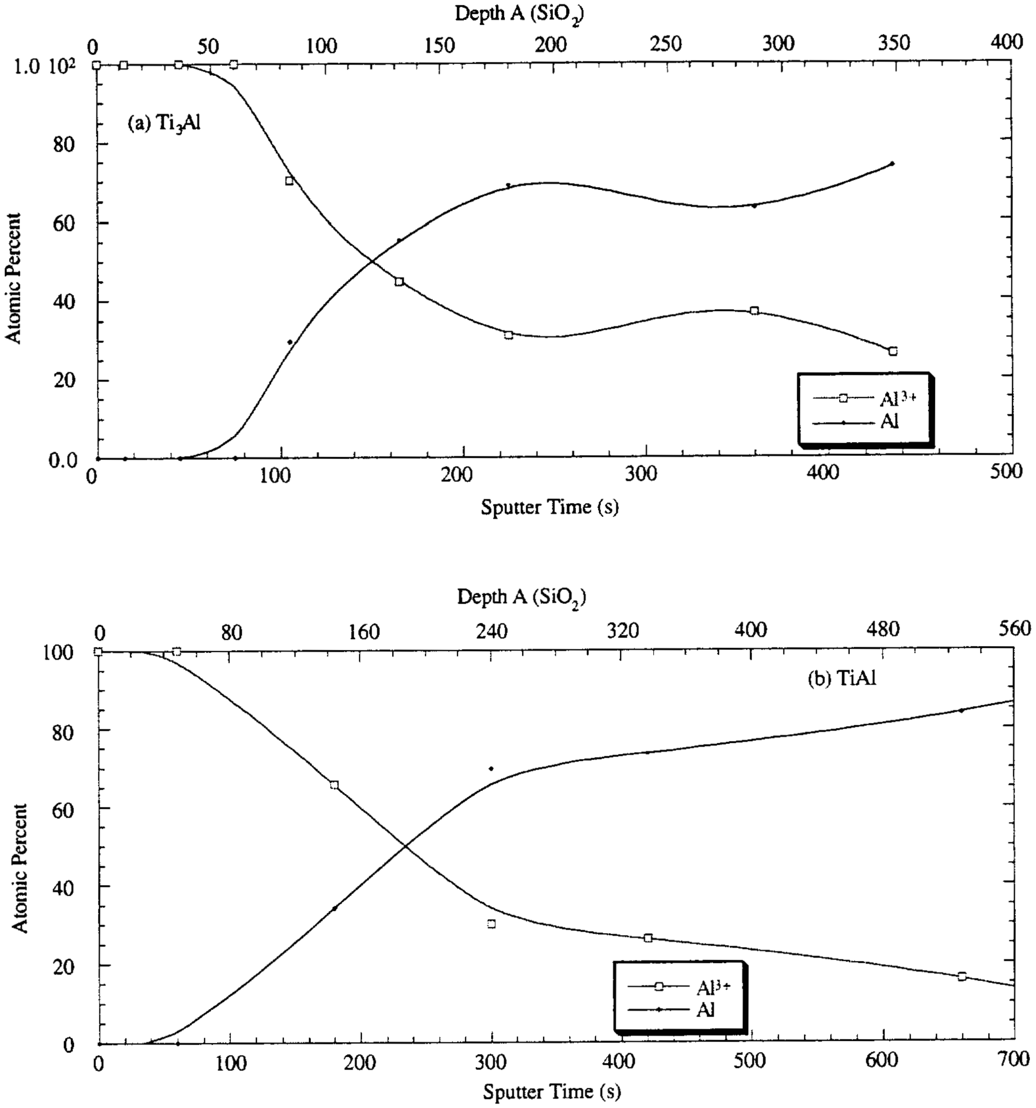

Figure 4-2-13. Depth profiles of different chemical states of Al for passive films formed in HNO_3. (a) Ti_3Al and (b) TiAl

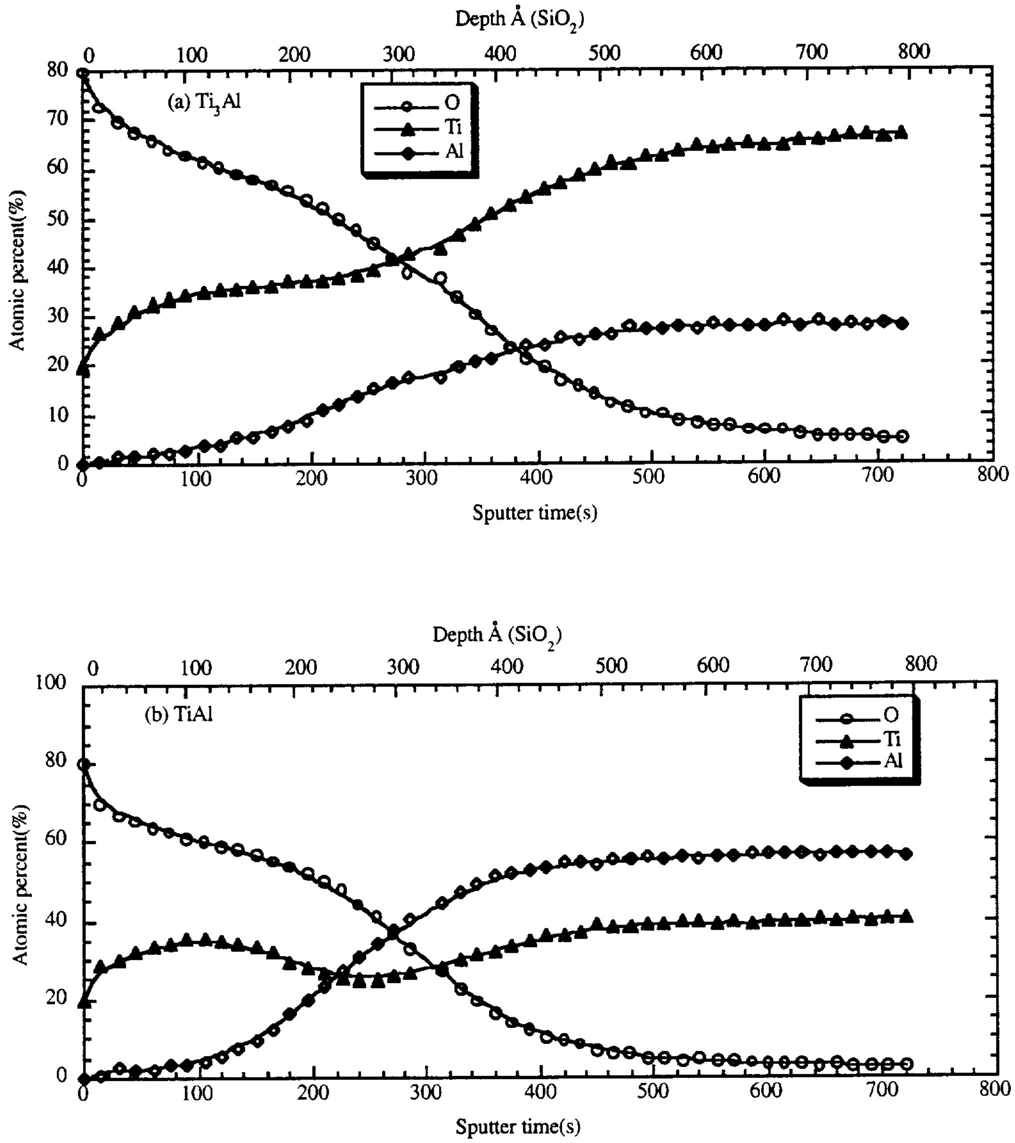

Figure 4-2-14. Depth profiles of Ti, Al and O for passive films formed in NaOH. (a) Ti_3Al and (b) TiAl

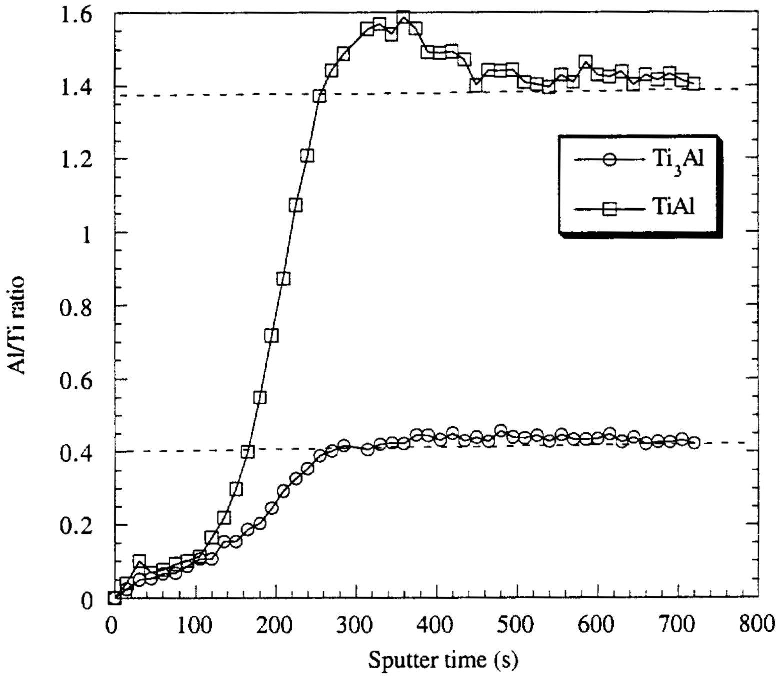

Figure 4-2-15. Depth profiles of Al/Ti ratio for Ti$_3$Al and TiAl in NaOH.

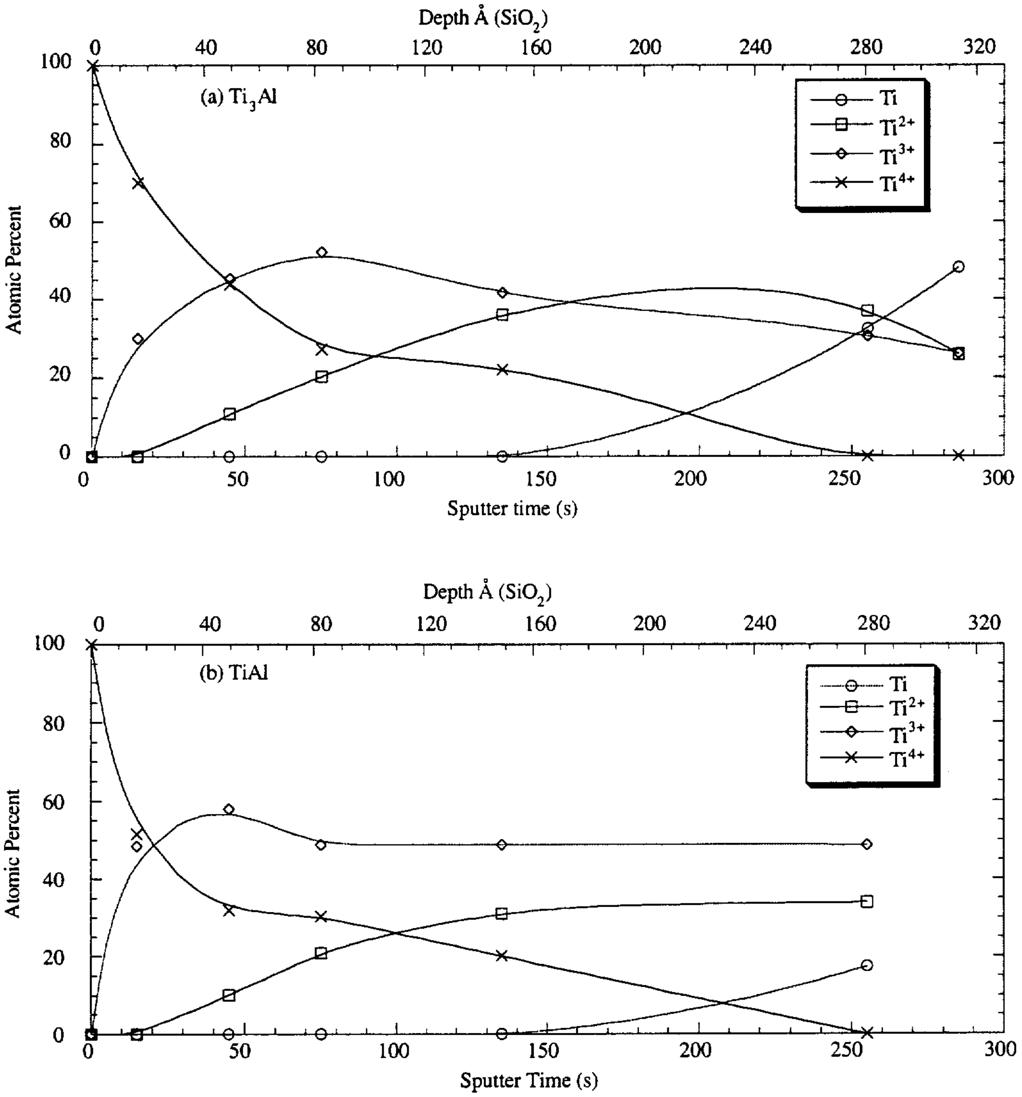

Figure 4-2-16. Depth profiles of different chemical states of Ti for passive films formed in NaOH. (a) Ti_3Al and (b) TiAl

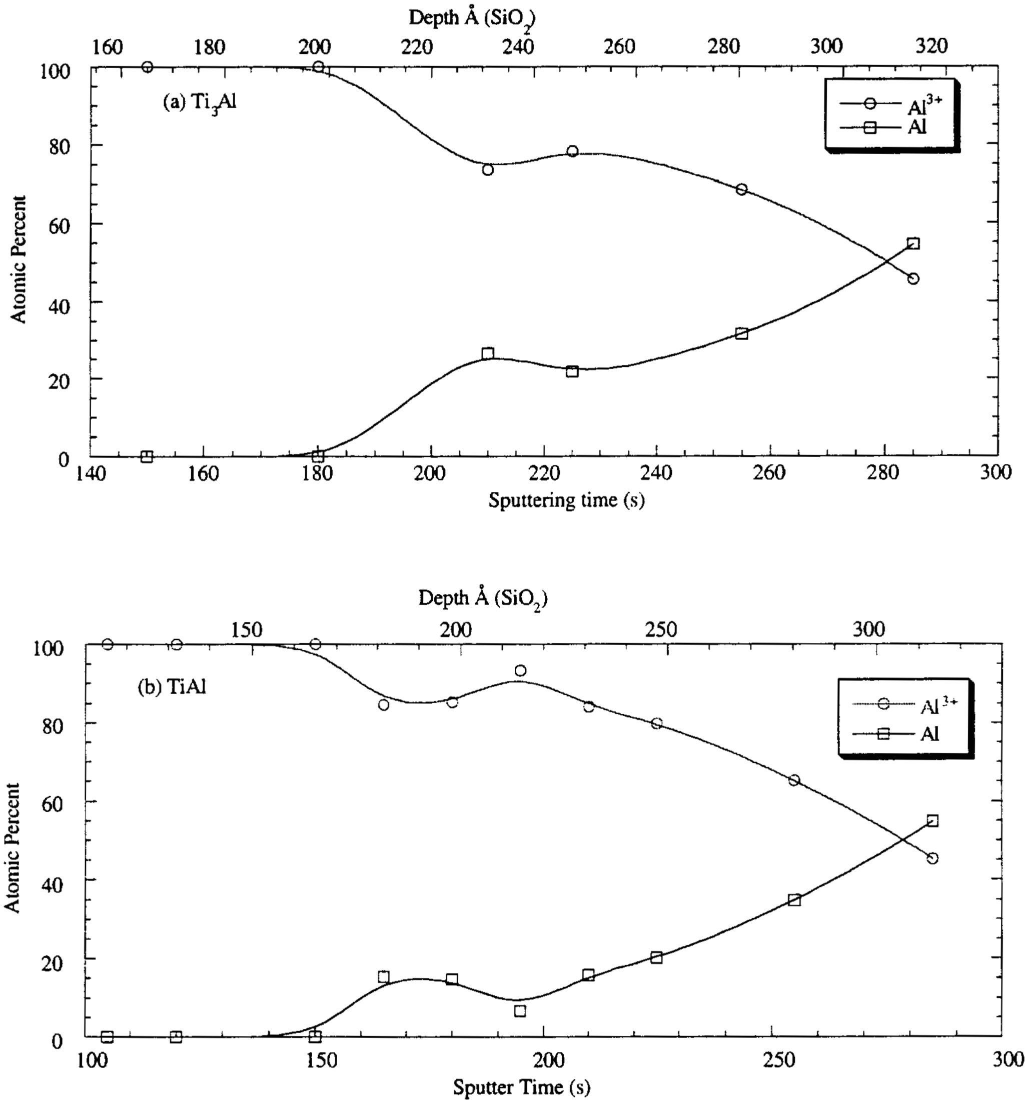

Figure 4-2-17. Depth profiles of different chemical states of Al for passive films formed in NaOH. (a) Ti_3Al and (b) TiAl

5. DISCUSSIONS

5.1 Summary of Experimental Results

Titanium aluminides were studied using scanning (potentiodynamic) and timed (potentiostatic) electrochemical methods, electrochemical impedance spectroscopy (EIS), and X-ray photoelectron spectroscopy(XPS) techniques.

The results of the potentiodynamic experiments show that titanium aluminides have similar electrochemical properties to that of titanium. Passive film breakdown was observed in solutions containing NO_3^- ion for all titanium aluminides except Ti_3Al. The breakdown potential increases with the decrease of the Al content in the materials as shown in Figure 5-1-1. According to literature, for titanium, the breakdown potential in HNO_3 is around 12.5V[74] and in H_2SO_4 the breakdown potential could exceed 80V. These values are much higher than the potentials applied in the potentiodynamic experiments for this study[13].

The passive current densities observed in the potentiostatic experiments after one hour polarization are shown in Figure 5-1-2. It shows that the current values for titanium aluminides change with the solution pH. The lowest values were found in the neutral solutions. The current values also depend upon specimen composition: the dissolution rates of Al and $TiAl_3$ are much higher than those of the other intermetallics.

Although this study presented data for $TiAl_3$, the emphasis was on the materials with high Ti content, such as TiAl and Ti_3Al. This is primarily because $TiAl_3$ is not under serious consideration for engineering applications. Therefore, in the following discussion, $TiAl_3$ will not be further discussed. As shown in Figure 5-1-3, in acidic solutions, the Steady-State Current Density (SSCD) increases with the increase of Al content. In the alkaline solutions, the SSCD values for titanium aluminides are very similar to that of Ti. In the neutral solutions, none of the specimens reached the steady state at the end of the one hour polarization. The current values for the materials in the neutral solutions are much lower than those in the acidic or alkaline solutions.

The XPS results of Ti_3Al and TiAl show that the passive film composition depend upon solution pH. In acidic solutions, the Ti/Al ratio in the passive film is similar to that of the bulk material. In the alkaline solution, there is nearly no Al in the topmost layer of the passive film. For films formed in either solution, the distribution of oxidation states in the passive film is similar: the higher oxidation states tend to exist in the topmost layers whereas the lower oxidation states tend to exist close to the metal/film interface. For Al, the only oxidation state determined on the surface by XPS is Al^{3+}. With the increase of depth, metallic Al becomes dominant. For Ti, titanium oxides are dominated by TiO_2 in the topmost layer in the passive films. With the increase of depth from the surface, Ti_2O_3 and TiO also appeared. According to the literature, ion sputtering used in XPS experiment may result in reduction of Ti^{4+} to Ti^{3+} or even lower oxidation states[93]. Therefore, the actual concentration for Ti^{4+} could be higher than those measured values. Based on the analysis above, we can see that the distributions of elements and oxidation states in the passive films for Ti_3Al and TiAl are not uniform.

Mott-Schottky plots for Ti, Ti_3Al and TiAl in H_2SO_4, NaOH and HNO_3 were derived from the Electrochemical Impedance Spectroscopy (EIS) results. The deviation from linearity was observed for all the specimens. De Gryse et al. suggested that the non-linearity of Mott-Schottky plot could be caused by the nonhomogenous donor distribution[12]. According to the literature, electrochemical behavior, passive film composition as well as electronic properties of passive films are closely related[83]. Therefore, the non-homogenous donor density distribution could be associated with the non-homogenous distribution of composition and oxidation states in the semiconducting passive film. The donor density distribution is also associated with the defect concentration in the passive film. In the following sections, a modified Mott-Schottky relation will be discussed which takes into account the nonhomogenous donor distribution of the passive film. The effect of point defect concentration on the dissolution rates of titanium aluminides will be analyzed based on the Point Defect Model[54].

5.2 Semiconductor Properties of Passive Film

Electrochemical Impedance Spectroscopy (EIS) is the most direct and most frequently used technique to measure capacitance values and, hence, characterize the electronic properties of passive film. Sometimes, however, despite the fact that EIS has produced interesting results, its use has not been pursued further because of the complexity of the data analysis[81]. TiO_2 is a typical example. Although the bulk TiO_2 is a n-type semiconductor[24], the TiO_2 passive film may behave quite different from an ideal semiconductor. The Mott-Schottky plot for an ideal semiconductor electrode normally demonstrates a linear relation between C^{-2} vs. V, where C is the depletion layer capacitance and V is the applied potential. For TiO_2 thin film, deviation from linearity is often observed[66-68,84,88]. De Gryse et al[12] suggests that this non-linear behavior could be due to the nonhomogenous donor distribution. Tomkiewicz [88] attributes this non-linearity to the existence of surface states. Schoonman et al.[84] conclude that the surface roughness effect and the occurrence of non-uniform donor distributions lead to the nonlinear Mott-Schottky plots. However, in reality, these conclusions are often difficult to compare, because the specimen preparation methods and experimental conditions might be quite different from each other. Chemical etching is the most often used method found in the literature to prepare TiO_2 passive film[66-68,84]. Other methods might involve polarizing the specimen at very high potentials[66,67] to form a stable oxide film. It is obvious, that different treatments might produce a different passive film structure, and therefore result in different conclusions.

The Mott-Schottky plot[94] describes the relation between the depletion layer capacitance and the applied potential of a semiconductor metal contact for semiconductors with homogenous donor distribution. For passive film, there is usually no distinct interface between the oxide layer and the metal substrate. The distribution of elements and oxidation states is not uniform either. As shown in the XPS results for titanium aluminides(Chap 4), there are four chemical states for titanium, two for Al, and the distribution of Ti and Al are not homogenous across the passive films.

According to classical semiconductor physics, the differential capacitance method can be used to determine the doping profile according to equation 5-2-1[94]:

$$N_D = \frac{2}{e \cdot \varepsilon\varepsilon_0}\left[-\frac{1}{d(1/C^2)/dV}\right] \qquad [5\text{-}2\text{-}1]$$

where V is the applied potential, C is the depletion layer capacitance, ε_0 is the permittivity of free space, ε is the dielectric constant of the semiconductor, e is the absolute value of the elementary charge.

As an example, the doping profile calculated using equation [5-2-1] for Ti, Ti_3Al, and TiAl passive films formed in H_2SO_4 are shown in Figure 5-2-1. Figure 5-2-1 shows that the donor density increases with the increase of the applied potential. According to the semiconductor physics, the width of the depletion layer increases with the increase of applied potential as illustrated in Figure 5-2-2[94]. Therefore, Figure 5-2-1 indicates that the donor density increases with the increase of the distance from the metal-oxide interface.

Da Fonseca et al.[83] found that for Ti passivated in H_2SO_4, the donor density decreases with the increase of Ti^{3+} concentration in the passive film. They suggest that Ti^{3+} acts as a p-type dopant for TiO_2. In this research, the XPS results of titanium aluminides show that, the higher oxidation states tend to exist in the topmost layer of the passive film, whereas the lower oxidation states become dominant at the metal-film interface. For titanium aluminide passive films, in addition to Ti^{3+}, the p-type dopant for TiO_2 also includes Al^{3+} whose concentration also decreases with the increases of depth from the surface. This implies that the donor density distribution is non-homogenous for passive films on titanium aluminides. Therefore, a modified Mott-Schottky relation is developed in the following section, based on the non-homogenous donor distribution model. For simplicity, it is assumed that the donor distribution is linearly graded as shown in Figure 5-2-2.

5.3 Mott-Schottky Relation For Linearly Graded Donor Distribution

In this section, a modified Mott-Schottky relation is derived, assuming a linearly graded donor distribution in a n-type semiconductor oxide film. The comparison of a linearly graded and a homogenous donor distribution is shown in Figure 5-3-1.

According to classical semiconductor physics, at thermal equilibrium, the Poisson equation can be expressed as[94]:

$$\frac{\partial^2 V}{\partial x^2}=\frac{\partial E}{\partial x}=\frac{\rho(x)}{\varepsilon_0\varepsilon_S}=\frac{e\cdot a\cdot x}{\varepsilon_0\varepsilon_S} \qquad [5\text{-}3\text{-}1]$$

where V is the potential, E is the electric field, ε_s is the dielectric constant of the semiconductor, $\rho(x)$ is the free electron density at location x, a is the donor density gradient, e is the absolute value of the elemental charge. By integrating equation [5-3-1] once, and with boundary conditions E(W) =0, where W is the width of the depletion layer, field distribution is derived as:

$$E(x) = -\frac{e \cdot a}{\varepsilon_0 \varepsilon_S} \frac{W^2 - x^2}{2} \qquad [5\text{-}3\text{-}2]$$

Integrating equation [5-3-2] gives the built-in potential V_{bi} as:

$$V_{bi} = \int_0^W \frac{e \cdot a}{\varepsilon_0 \varepsilon_s} \frac{W^2 - x^2}{2} dx = \frac{e \cdot a \cdot W^3}{3 \varepsilon_0 \varepsilon_S} \qquad [5\text{-}3\text{-}3]$$

or

$$W = \left(\frac{3 \varepsilon_0 \varepsilon_s \cdot V_{bi}}{e \cdot a} \right)^{1/3} \qquad [5\text{-}3\text{-}4]$$

The space charge Q_S can be expressed as:

$$Q_s = \int_0^W a \cdot e \cdot x dx = \frac{1}{2} a \cdot e \cdot W^2 \qquad [5\text{-}3\text{-}5]$$

Therefore, the capacitance C_S is given by:

$$C_S = \frac{dQ_s}{dV_{bi}} = \frac{d(1/2 \cdot a \cdot e \cdot W^2)}{d(\frac{a \cdot e \cdot W^3}{3 \varepsilon_0 \varepsilon_S})} = \frac{\varepsilon_0 \varepsilon_s}{W} = \left(\frac{e \cdot a \cdot (\varepsilon_0 \varepsilon_S)^2}{3 V_{bi}} \right)^{1/3} \qquad [5\text{-}3\text{-}6]$$

When a voltage V is applied to the junction, by definition, the total electrostatic potential variation across the junction is given by $(V_{bi} + V) = \phi_s$. Therefore, by similar calculation, C_S can be expressed as:

$$C_S = \left(\frac{e \cdot a \cdot (\varepsilon_0 \varepsilon_S)^2}{3(\phi_s - kT/e)} \right)^{1/3} \qquad [5\text{-}3\text{-}7]$$

where the correction factor kT/e comes because of the majority-carrier distribution tails[94]. To simplify the calculation, it is assumed that:

$$C_S << C_H \qquad [5\text{-}3\text{-}8]$$

where C_S and C_H are the unit area capacitance for the depletion layer of the semiconductor and the Helmholtz layer at the semiconductor surface, respectively. The potential drop over the depletion layer can be expressed as:

$$\phi_S = V - V_{fb} - kT/e - \phi_H \qquad [5\text{-}3\text{-}9]$$

where ϕ_s is the potential drop over the depletion layer, and ϕ_H the change in Helmholtz potential drop caused by the applied voltage[12]. Therefore, we have:

$$\frac{Q_S}{C_S} = \frac{a \cdot W^3}{2 \cdot \varepsilon_S} = \left(\frac{3\phi_S}{2}\right) \qquad [5\text{-}3\text{-}10]$$

or

$$\phi_S = \frac{2}{3}\frac{Q_S}{C_S} \qquad [5\text{-}3\text{-}10']$$

It is assumed that the variation of C_H as a function ϕ_H is negligible. For concentrated electrolyte solutions, this assumption implies the absence of ion adsorption[12,95]. Under the above assumption, the potential change ϕ_H can be expressed as:

$$\phi_H = Q_S/C_H = (C_S/C_H)Q_S/C_S = (3C_S/2C_H)\phi_S \qquad [5\text{-}3\text{-}11]$$

where V is the applied potential, V_{fb} is the flatband potential. Therefore, for $C_S \ll C_H$, there is $\phi_H \ll \phi_S$ based on equation [5-3-11]. For the measured capacitance C, the following equation is valid:

$$\frac{1}{C} - \frac{1}{C_H} = \frac{1}{C_S} \qquad [5\text{-}3\text{-}13]$$

Combining equation [5-3-9] and equation [5-3-11] gives:

$$V - V_{fb} - kT/e = \phi_S + \phi_H = \phi_S + \frac{3C_S}{2C_H}\phi_S \qquad [5\text{-}3\text{-}14]$$

By substituting C_S in equation [5-3-13] from equation [5-3-14], we have:

$$V - V_{fb} - kT/e = \phi_S + \phi_H = \frac{\frac{2}{C} + \frac{1}{C_H}}{2 \cdot \left(\frac{1}{C} - \frac{1}{C_H} \right)} \cdot \phi_S \qquad [5\text{-}3\text{-}15]$$

or

$$\phi_S = \frac{2 \cdot \left(\frac{1}{C} - \frac{1}{C_H} \right)}{\frac{2}{C} + \frac{1}{C_H}} \cdot (V - V_{fb} - kT/e) \qquad [5\text{-}3\text{-}16]$$

The relation between the measured capacitance C and applied potential V becomes:

$$\left(\frac{1}{C} - \frac{1}{C_H} \right)^3 = \left(\frac{3}{e \cdot a \cdot (\varepsilon_0 \varepsilon_S)^2} \right) \cdot \frac{2 \cdot \left(\frac{1}{C} - \frac{1}{C_H} \right)}{\frac{2}{C} + \frac{1}{C_H}} \cdot (V - V_{fb} - kT/e) \qquad [5\text{-}3\text{-}17]$$

or

$$\left(\frac{1}{C} + \frac{1}{2C_H} \right) \cdot \left(\frac{1}{C} - \frac{1}{C_H} \right)^2 = \left(\frac{3}{e \cdot a \cdot (\varepsilon_0 \varepsilon_S)^2} \right) \cdot (V - V_{fb} - kT/e) \qquad [5\text{-}3\text{-}18]$$

Expanding the left side of equation [5-3-18] leads to:

$$\frac{1}{C^3} - \frac{3}{2C^2 \cdot C_H} + \frac{1}{2C_H^3} = \left(\frac{3}{e \cdot a \cdot (\varepsilon_0 \varepsilon_S)^2} \right) \cdot (V - V_{fb} - kT/e) \qquad [5\text{-}3\text{-}19]$$

If $C << C_H$, equation [5-3-19] can be simplified as:

$$\left(\frac{1}{C} \right)^3 = \left(\frac{3}{e \cdot a \cdot (\varepsilon_0 \varepsilon_S)^2} \right) \cdot (V - V_{fb} - kT/e) \qquad [5\text{-}3\text{-}20]$$

Therefore, the donor density gradient ‘a’, can be derived from the slope, S, of the C^{-3} vs. V plot according to equation [5-3-20]:

$$a = \left(\frac{3}{e \cdot S \cdot (\varepsilon_0 \varepsilon_S)^2} \right) \qquad [5\text{-}3\text{-}21]$$

where S is the slope in the C^{-3} vs. V plot.

When C_H is not considerably smaller than C_S, the error of equation [5-3-21] can be relatively large. Assuming that a_1 is the donor distribution gradient calculated by equation [5-3-21](without considering C_H), a_2 is the donor distribution gradient calculated by equation [5-3-19](with the consideration of the effect of C_H), the relationship between a_1 and a_2 can be obtained as the following. By differentiating equation [5-3-19], we have:

$$\left(\frac{3}{e \cdot a_2 \cdot (\varepsilon_0 \varepsilon_S)^2} \right) = \frac{d\left(\frac{1}{C^3} - \frac{3}{2C^2 \cdot C_H} + \frac{1}{2C_H^3} \right)}{dV} = \frac{d(1/C)}{dV} \left(3C^{-2} - \frac{3}{C \cdot C_H} \right) \qquad [5\text{-}3\text{-}22]$$

Differentiating equation [5-3-21] gives:

$$\left(\frac{3}{e \cdot a_1 \cdot (\varepsilon_0 \varepsilon_S)^2} \right) = \frac{d(1/C^3)}{dV} = 3\frac{d(1/C)}{dV} C^{-2} \qquad [5\text{-}3\text{-}23]$$

By combining equation [5-3-22] and equation [5-3-23], we have:

$$\left(\frac{a_2}{a_1} \right) = \frac{3C^{-2}}{\left(3C^{-2} - \frac{3}{C \cdot C_H} \right)} = \frac{C_H}{C_H - C} \qquad [5\text{-}3\text{-}24]$$

Therefore, the error introduced by neglecting C_H is:

$$\left(\frac{a_2 - a_1}{a_2} \right) = 1 - \frac{C_H - C}{C_H} = \frac{C}{C_H} \qquad [5\text{-}3\text{-}25]$$

For example, if C_H is 10 times as large as C, then the error is approximately 10%. If C_H is the same as C_S or twice as large as C, the error could be as large as 100%.

To estimate the flatband potential shift due to the Helmholtz capacitance C_H, the effect of both the $\frac{1}{2C_H^3}$ and the $\frac{3}{2C^2 \cdot C_H}$ terms in equation [5-3-19] need to be considered. The flatband potential shift caused by C_H is:

$$\Delta V_{fb} = V_{fb} - V_{fb}^{'} = \frac{1}{S_2}\left(\frac{1}{C^3} - \frac{3}{2C^2 \cdot C_H} + \frac{1}{2C_H^3}\right) - \frac{1}{S_1}\left(\frac{1}{C^3}\right) \qquad [5\text{-}3\text{-}26]$$

According to equation [5-3-21] and [5-3-24], the ratio of S_1/S_2 is:

$$\frac{S_1}{S_2} = \frac{a_2}{a_1} = \frac{C_H}{C_H - C} \qquad [5\text{-}3\text{-}27]$$

Therefore, equation [5-3-26] can be simplified as:

$$\begin{aligned}\Delta V_{fb} = V_{fb} - V_{fb}^{'} &= \frac{C_H}{S_1(C_H - C)}\left(\frac{1}{C^3} - \frac{3}{2C^2 \cdot C_H} + \frac{1}{2C_H^3}\right) - \frac{1}{S_1}\left(\frac{1}{C^3}\right) \\ &= \frac{1}{2S_1(C_H - C)}\left(\frac{1}{C^2} - \frac{1}{C_H^2}\right)\end{aligned} \qquad [5\text{-}3\text{-}28]$$

Assuming $\varepsilon_S = 60$ for TiO_2, $a=10^{36}m^{-3}$, $C_H=0.5\ Fm^{-2}$, according to equation [5-3-28], the shift of the flatband potential is approximately -0.3V. For $C_H = 0.2Fm^{-2}$, the shift could be as large as -1.3V. Therefore, if C_H is relatively small, it may have significant effect on the estimated value of V_{fb}. Figure 5-3-3 is a simulated plot that shows the effect of C_H on the shape of the curve with $\varepsilon_S = 60$ (for TiO_2)[83], $a = 10^{36}m^{-3}$, $C_H = 0.2, 0.5, 1, 2\ Fm^{-2}$. The simulated total capacitance, C, is derived from equation [5-3-7] and [5-3-13]. The ideal values are $S_{ideal} = 66.5$, $V_{fb} = 0$. The flatband potentials are calculated based on the simulated plot using equation [5-3-27]. Results are summarized in Table 5-3-1.

As shown in Figure 5-3-3, when the C_H decreases to values close to C_{SC}, the plot becomes curved. This indicates that when C_H is very low, non-linear relation between C_H^{-3} vs. V_M can be observed.

Figure 5-3-4 to Figure 5-3-6 shows the Modified Mott-Schottky plots for Ti, Ti_3Al and TiAl in H_2SO_4, NaOH and HNO_3, respectively. In most cases, the Modified Mott-Schottky plots show a good linear relation of C^{-3} vs. V_M. This confirms our assumption that the donor distribution inside the passive films can be approximated as linearly graded. For TiAl formed in H_2SO_4, relatively large deviation from linearity was observed at high film formation potentials. As shown in Figure 4-4-3 in the previous chapter, such break in linearity was also observed in the original Mott-Schottky plot. Therefore, such anomaly may not be caused by donor distribution alone. Other factors such as specimen defects in the oxide film may also need to be considered.

Assuming that C_H is negligible, the donor density gradients for Ti, Ti_3Al and TiAl are calculated using equation [5-3-21]. The change of the donor density gradient with the film formation potential is shown in Figure 5-3-7, where the donor density gradients for Ti are the highest. The values for Ti_3Al and TiAl are very similar to each other in all the solutions. The donor density gradient decreases with the increase of film formation potential for all the investigated materials, which is similar to the results shown by the original Mott-Schottky plot as discussed in chapter 4.

By assuming a film growth rate of $2nmV^{-1}$ and an average film formation potential of 1V above the flatband potential, the donor density on the surface can be estimated by:

$$N_D = 2nm*a \qquad [5\text{-}3\text{-}29]$$

where a is the donor density gradient. Using the donor density gradient as $10^{36}m^{-3}$, the donor density on the film surface can be estimated as the order of $10^{27}m^{-3}$. This value is very close to the value calculated using the original Mott-Schottky relation which was discussed in Chapter 4.

The analysis above shows that the modified Mott-Schottky relation predicated very well the linear relation between C^{-3} vs. V. This indicates that the donor distribution inside a semiconductor passive film is not homogenous. It can be approximated by a linearly graded donor distribution. As discussed previously, the semiconductor properties of passive films come from the existence of energy states caused by ionization of vacancies. Therefore, the linearly graded donor distribution indicates that the vacancy distribution inside the passive films on titanium aluminides is not homogenous. The vacancy concentration is lower at the metal/film interface and higher in the film/solution interface.

5.4 Semiconductor Properties vs. Point Defects

According to semiconductor physics, the presence of foreign atoms in crystals may lead to an essential change in their physical and chemical properties. In semiconductor elements and in compounds of nearly stoichiometric composition, the control of their properties is realized by introducing into the crystal admixtures of either donor or acceptor character. For oxide passive films, which have the tendency to deviate from stoichiometry, the donors or acceptors in oxides are provided by both native defects and foreign atoms incorporated into the crystal lattice[96].

In oxide crystals, there are several basic types of disorder[97,98], such as Schottky disorder, Frenkel disorder, and antistructural defects. Ionic diffusion by Frenkel disorder and Schottky defects is most likely to occur and could be the rate-controlling step for oxidation of most metals[24]. Many investigators differentiate high-temperature scales that form on metals under gaseous conditions from low-temperature films that form in aqueous solution. Due to the many similarities of the two systems, and the rich amount of literature concerning high-temperature scales, in this research, some of the discussions are based on results obtained for the high temperature system which has been accepted by many researchers for low-temperature aqueous solution systems[24,50,54,75].

The symbols used in this chapter were proposed by Kroger and Vink[99,100]. In the Kroger and Vink system, all constituents of a crystal lattice are regarded as atoms, no matter if the crystal is covalent or ionic. For covalent crystals, obviously such a system is adequate. For ionic crystals, only the effective charge is important and thus writing down a normal ionic charge in all reactions is necessary[96].

As an example, for a hypothetical oxide $MO_{x/2}$, where M stands for a metal atom, O denotes oxygen, electrically neutral atomic defects are:

(1) Neutral vacancies in the sublattice M: vacancy in the sublattice M denoted by V_M^x. V_M^x indicates a neutral vacancy resulting from the removal of a M^{x+} ion from the cationic lattice site together with two electrons from the cationic sublattice.

(2) Neutral vacancies in the oxygen sublattice: V_O^x indicates a neutral vacancy resulting from the removal of a O^{2-} ion from the oxygen sublattice.

Assuming the donor and acceptor levels are completely ionized[100], the process of ionization of the donor defects in a crystal $MO_{x/2}$ can be described by the following quasi-chemical reactions[100]:

$$V_M^x <==> V_M' + h^{\circ} \qquad [5-4-1]$$

$$V_o^x <==> V_o^{\circ} + e' \qquad [5-4-2]$$

where e' denotes a quasi-free electron in the conduction band having a negative charge indicated by '; $h^{\circ}$is a positive hole in the valence band formed by the removal of an electron indicated by °; V_M' and V_o° are the singly-ionized cationic or anodic vacancy, respectively. Obviously, the singly-ionized atomic defects can undergo further ionization according to the reactions:

$V_M' <==> V_M'' + h^\circ$ [5-4-3]

$V_o^\circ <==> V_o^{\circ\circ} + e'$ [5-4-4]

The energy level diagram for crystal $MO_{x/2}$ containing cation vacancies and anion vacancies is shown in Figure 5-4-1. The assumption that the donor and acceptor levels are completely ionized could be fulfilled in practice due to the very high electric filed strength in the passive film (10^6-10^7 Vcm^{-1})[54].

Since the oxide must be electrically neutral, the combination of these different disorders must always be balanced to attain charge neutrality. In order to maintain this neutrality, electronic defects must also be accounted for in the defect structure. For truly stoichiometric crystals, the electronic defect concentration is generally negligible. In reality, few corrosion films are stoichiometric, more often they are nonstoichiometric. The deviation from stoichiometry of most corrosion films has been found to produce semiconductive behavior[24]. If the defects are only singly-ionized, the neutrality condition may be written in the form of the following equation[100]:

$n + [V_M'] = p + [V_O^\circ]$ [5-4-5]

where n is the electron concentration and p is the hole concentration, $[V_M']$ is the single-ionized cation vacancy concentration, $[V_O^\circ]$ is the single-ionized oxygen vacancy concentration. Therefore, for n-type oxide film:

$n >> p$ [5-4-6]

and

$n \approx n - p = [V_O^\circ] - [V_M']$ [5-4-7]

In the case $[V_O^\circ] >> [V_M']$, the following equation holds:

$n \approx [V_O^\circ]$ [5-4-8]

If foreign atoms are incorporated into the oxide, the general rules are: if the foreign atom F_M has fewer valence electrons than the matrix atom M, its incorporation is accompanied by the appearance of an acceptor level; if it has more valence electrons, the incorporation is accompanied by the appearance of a donor level[96]. Therefore, for passive films on titanium aluminides, the incorporation of Al^{3+} into TiO_2 results in a decrease of the donor density. The reaction can be expressed as[24]:

$$Al_2O_{3(\text{in TiO2})} + 2e' + \frac{1}{2}O_2 \rightarrow 2Al_{(Ti')}O_2 \qquad [5\text{-}4\text{-}9]$$

where e' is a free electron, $Al_{(Ti')}$ is the Al^{3+} cation in the cation site of TiO_2 and with a negative charge, O_2 is the oxygen. The $Al_{(Ti')}O_2$ oxide is a less stable oxide structure than that of TiO_2 and will further react as:

$$Al_{(Ti')}O_2 \rightarrow 2O_O + Al^{3+}{}_{(aq)} + V_{Ti}^{4+} \qquad [5\text{-}4\text{-}10]$$

where $Al^{3+}{}_{(aq)}$ is a Al^{3+} cation released into the solution, O_O is a oxygen anion in the anion site, V_{Ti}^{4+} is a Ti^{4+} cation vacancy. Therefore, the incorporation Al into the passive film not only decreases the donor density but also may increase the cation vacancy density.

5.5 Point Defect Model

The point defect model was first published in 1982 by Macdonald et al[36,50,52-54,75,101]. Macdonald et al. modeled the growth of passive film in terms of diffusion of point defects in a concentration gradient and under the influence of electric field[50,52-55]. Macdonald et al. raise two very important questions: (1) What are the point defects present in the passive films? (2) Which defect species are the mobile species? Macdonald suggests that diffusion of metal vacancies contributes to corrosion only, while the diffusion of oxygen vacancies is associated with the growth of the passive film. Thus, the growth rate of the passive film is equal to the diffusion flux of oxygen vacancies in the electrochemical potential gradient that exists in the passive film. Therefore, in order to be protective, the passive film has to function as a barrier against metal vacancy diffusion[39]. Point Defect Model is based on the following assumptions:

(1) A continuous passive film will form on the surface of the metal, whenever the external potential(V_{ext}), is more noble than the flatband potential.
(2) Passive film contains a high concentration of point defects. High temperature studies indicate that the majorities of point defects that exist in an oxide film are cation vacancy ($V_M^{\chi'}$), oxygen vacancy ($V_O^{\circ\circ}$), electrons (e'), and electron holes

(h'). The same species of point defects are expected to be present in a passive film formed at ambient temperature.

(3) The field strength is of the same order as that required for dielectric breakdown. Accordingly, the passive film behaves as an "incipient semiconductor" because it exists on the verge of dielectric breakdown.

(4) Electrons (e') and electron holes (h°) in the passive film are in equilibrium, and the electrochemical reactions involving electrons (or electron holes) are rate-controlled at either the metal/film or the film/solution interfaces. Also, the rate-controlling step for those processes is assumed to be the transport of the vacancies across the film.

According to the point defect model, there are five possible reactions that are associated with the film formation and dissolution process: Two reactions occur at the metal/film interface:

[1] $m + V_M^{\chi'} \xrightarrow{k1} V_m + M_M + \chi e'$

[2] $m \xleftrightarrow{k2} M_M + \frac{\chi}{2} V_O^{\infty} + \chi e'$

Three reactions occur at the film/solution interface:

[3] $M_M \xleftrightarrow{k3} M^{\chi+}{}_{(aq)} + V_M^{\chi'}$

[4] $V_O^{\infty} + H_2O \xleftrightarrow{k4} O_O + 2H^+$

[5] $MO_{\chi/2} + \chi H^+ \xrightarrow{k_5} M^{\chi+} + \frac{\chi}{2} H_2O$

where m = metal atom, M_M = metal cation in cation site, O_O = oxygen anion in anion site, $V_M^{\chi'}$= cation vacancy, $V_O^{\circ\circ}$ = anion vacancy, V_M = metal vacancy in the metal phase[52], k_1 to k_5 are reaction constants.

Reactions [1] and [3] account for the consumption and formation of cation vacancies at the metal/film and film/solution interfaces, respectively. Reactions [2] and [4] describe the consumption and formation of oxygen anion vacancies. Reaction [5] is included to describe the irreversible dissolution of the film at the primary film/solution interface. Furthermore, reactions [1], [3] and [4] are lattice-conservative processes: they do not result in any dimensional change in the film. On the other hand, reaction [2] creates more lattice site and reaction [5] results in the film destruction.

Questions on reaction [2] may arise because it does not conserve lattice sites at the metal/film interface. In reaction [2], a metal site expands to a metal cation and $\chi/2$ anion vacancy sites at the metal/film interface. This may not be a favorable reaction because of geometry and energy constrictions. Also, according to reaction [1], metal vacancies are produced at the metal/film interface. However, metal vacancies will never be consumed by any reaction in the point defect model. Moreover, the dissolution of passive film is not only pH dependent, but also closely related to the defect concentration in the passive films. However, according to the point defect model, the dissolution rate depends only on the pH and applied potentials; there is no direct relation between the dissolution rate of the passive film and the vacancy concentration inside the film.

To solve these problems, the point defect model is modified as shown in Figure 5-5-1. In this new model, two reactions are modified from the original model: reaction [2'] and reaction [5']. In reaction [2'], an extra metal vacancy V_M is introduced to meet the geometric constriction. Therefore, there is no extra lattice site produced in reaction[2']. Also, the metal vacancies produced by reaction [1] could be consumed by reaction [2']. This eliminated the problem that the metal vacancies are only being generated but not consumed. Reaction [5'] is the basic Schottky pair reaction[39,102]. It is responsible for the film destruction as demonstrated in the following paragraphs. The reaction rate for reaction [5'] is directly related to the vacancy concentrations and the electric field strength inside the film. Therefore, the dissolution rate of the passive film is also closely related to the vacancy concentrations and the electric field strength.

In the new model, the film dissolution occur based on the following step:

$$MO_{\chi/2} + \chi H^+ \longleftrightarrow M_M + \chi/2\, O_O + \chi H^+ \qquad [5\text{-}5\text{-}1]$$

$$M_M + \chi/2\, O_O + \chi H^+ \xleftrightarrow{[3,4]} M^{\chi+}{}_{(aq)} + V_M^{\chi'} + \chi/2\, V_O^{\infty} + \chi H_2O \qquad [5\text{-}5\text{-}2]$$

$$M^{\chi+}{}_{(aq)} + V_M^{\chi'} + \chi/2\, V_O^{\infty} + \chi H_2O \xleftrightarrow{[5']} M^{\chi+}{}_{(aq)} + \chi H_2O \qquad [5\text{-}5\text{-}3]$$

By combining reaction [5-5-1], [5-5-3], and [5-5-3], reaction [5-5-4] can be derived which is the same as the film dissolution reaction (reaction [5]) in the original point defect model:

$$MO_{\chi/2} + \chi H^+ \xrightarrow{\text{surface}} M^{\chi+}{}_{(aq)} + \chi/2\, H_2O \qquad [5\text{-}5\text{-}4]$$

From reaction [1] and reaction [2'], a reaction is derived that converts cation vacancies to anion vacancies:

$$\mathrm{M}+{}^{\chi}\!/_{2}(\mathrm{M}+\mathrm{V}_{\mathrm{M}}^{\chi'})\xrightarrow{[1]}\mathrm{M}+{}^{\chi}\!/_{2}(\mathrm{M}_{\mathrm{M}}+\mathrm{V}_{\mathrm{M}}+\chi\mathrm{e}') \qquad [5\text{-}5\text{-}5]$$

$$\mathrm{M}+{}^{\chi}\!/_{2}(\mathrm{M}_{\mathrm{M}}+\mathrm{V}_{\mathrm{M}}+\chi\mathrm{e}')\xrightarrow{[2']}(1+{}^{\chi}\!/_{2})\mathrm{M}_{\mathrm{M}}+{}^{\chi}\!/_{2}\,\mathrm{V}_{\mathrm{O}}^{\infty}+(1+{}^{\chi}\!/_{2}){}^{\chi}\!/_{2}\,\mathrm{e}' \qquad [5\text{-}5\text{-}6]$$

Combining reaction [5-5-7] and [5-5-8] gives:

$$\mathrm{M}+{}^{\chi}\!/_{2}(\mathrm{M}+\mathrm{V}_{M}^{\chi'})\xrightarrow{[1,2']}(1+{}^{\chi}\!/_{2})\mathrm{M}_{M}+{}^{\chi}\!/_{2}\,\mathrm{V}_{O}^{\infty}+(1+{}^{\chi}\!/_{2}){}^{\chi}\!/_{2}\,\mathrm{e}' \qquad [5\text{-}5\text{-}7]$$

Reaction [5-5-7] shows that metal cation vacancies are consumed and oxygen anion vacancies are generated at the metal/film interface. This is a possible reaction suggested by Macdonald that converts cation vacancies to anion vacancies[53].

Similar to the original point defect model, our new model also includes two reactions that are not conservative to lattice sites which are reaction [2'] and reaction [5']. Reaction [2'] accounts for the generation of oxygen vacancies and the consumption of metal vacancies. Reaction [2'] is not lattice-conservative in the sense that it converts metal vacancies to anion vacancies. However, no extra lattice sites are generated during this reaction. Reaction [5'] accounts for passive film dissolution: cation vacancies and anion vacancies are annihilated at the film/solution interface through this reaction. Different from the original model, in this modified point defect model, the film dissolution rate is controlled by the Schottky pair reaction [5']. The reaction rate depends on both the defect concentration and electric field strength inside the oxide film.

In the following paragraphs, the dissolution behavior of titanium aluminides based on this modified point defect model will be discussed. The passive film is consider primarily consisted of TiO_2. Al^{3+} and the lower oxidation states of Ti are treated as dopants. This simplification is based on our experiment results that the dissolution behavior of Ti_3Al and TiAl is similar to that of Ti. Also, Ti is the major element in the materials that accounts for more than 84wt% in Ti_3Al and 61wt% in TiAl.

The modified point defect model for TiO_2 passive film is shown in Figure 5-5-2. As shown in Figure 5-5-2, the steady state involves two non-conservative reactions: film generation and film dissolution (only one non-conservative reaction would result in monotonic growth or thinning of the film). The dissolution rate, therefore, can be calculated using the following equations. The cation vacancies flux J_3 is generated in reaction [3] as:

$$J_3 = \frac{k_3}{[V_{Ti}^{4'}][Ti^{4+}]} \qquad [5\text{-}5\text{-}8]$$

where k_3 is the reaction constant. At the steady state, the cation vacancies could be consumed by two reactions: [1] and [5']. To simplify the calculation, it is assumed that the concentration gradients for the Ti^{4+}_{aq} cations in the electrolyte are negligible and therefore the concentrations of the cations at the surface of the passive film can be equated with the bulk solution values. This condition is expected to hold if convective transport in the electrolyte is fast compared with rates of the reactions that generate or consume the ions at the film/solution interface[52]. Therefore, equation [5-5-8] can be simplified as:

$$J_3 = \frac{k'_3}{[V_{Ti}^{4'}]} \qquad [5\text{-}5\text{-}9]$$

where k'_3 is a constant. Because the very strong electric field (10^6-10^7 Vcm^{-1}) exists across the passive film[53], the Nernst-Planck equation governs the transport of these defects in a concentration and electric field[39]. It is also assumed that the cation vacancy transport controls the reaction rate for reaction [1]. Therefore, the cation vacancy transport can be expressed as[39]:

$$J_{V_{Ti}^{4'}} = M[V_{Ti}^{4'}](\frac{\partial u}{\partial x} + \varepsilon q) \qquad [5\text{-}5\text{-}10]$$

where M is the mobility of the cation vacancy, $[V_{Ti}^{4'}]$ is the concentration of Ti^{4+} cation vacancy on the passive film surface, u is the chemical potential of the cation vacancy, ε is the electric field, and q is the charge. Assuming that the electric field, ε, and chemical potential, u, are constants inside the passive film, equation [5-5-10] can be simplified as:

$$J_{V_{Ti}^{4'}} = k_7[V_{Ti}^{4'}] \qquad [5\text{-}5\text{-}11]$$

where $k_7 = M(\frac{\partial u}{\partial x} + \varepsilon q)$ is a constant. At the steady state, the cation vacancies transported to the metal/film interface are converted to anion vacancies. Therefore, the flux of the cation vacancy is equal to the flux of anion vacancy as shown in equation [5-5-12]:

$$J_{V_O^{\cdot\cdot}} = J_{V_{Ti}^{4'}} = k_7[V_{Ti}^{4'}] \tag*{[5-5-12]}$$

The analysis above shows that the cation vacancies generated by reaction [3] are consumed by two reactions: reaction [2'] at the metal/film interface, and the reaction [5'] at the film/solution interface. At the steady state, reaction [4] must be in equilibrium which means that the thickness of the oxide film is a constant. Therefore, the anion vacancies transported to the film/solution interface are equal to the anion vacancies consumed by reaction [5']. According to reaction [5'], for every cation vacancy annihilated in this reaction, there are two anion vacancies consumed. Therefore, the cation vacancy flux generated in reaction [3] can be expressed as:

$$J_3 = J_{V_{Ti}^{4'}} + \frac{1}{2}J_{V_O^{\cdot\cdot}} = \frac{3}{2}J_{V_{Ti}^{4'}} \tag*{[5-5-13]}$$

By solving equation [5-5-8] to [5-5-13], the following equation can be derived:

$$\frac{k'_3}{[V_{Ti}^{4'}]} = \frac{3}{2}k_7[V_{Ti}^{4'}] \tag*{[5-5-14]}$$

By solving equation [5-5-8], J_3 is derived as:

$$J_3 = \left(\frac{3}{2}k_7k'_3\right)^{1/2} \tag*{[5-5-15]}$$

At the steady state, the flux J_3 is equal to the cation dissolution rate as well as the film growth rate. Therefore, the steady state current density can be expressed as:

$$I_{SS} = q \cdot J_3 = q \cdot \left(\frac{3}{2}k_7k'_3\right)^{1/2} \tag*{[5-5-16]}$$

or

$$I_{SS} = q \cdot J_3 = q \cdot \left(\frac{3}{2}M\left(\frac{\partial u}{\partial x} + \varepsilon q\right)k'_3\right)^{1/2} \tag*{[5-5-17]}$$

where I_{SS} is the steady state current density. Equation [5-5-17] shows that the dissolution rate of a passive film is associated with the mobility M of cation vacancy. According to Nernst-Einstein equation, M can be expressed from[103]:

$$M = D/kT \tag*{[5-5-18]}$$

where D is the diffusion coefficient of the cations. D can be calculated as[103]:

$$D = a_0{}^2 N_v w \qquad [5\text{-}5\text{-}19]$$

where N_v is the fraction of sites vacant, w is the jump frequency, and a_0 is a constant. Substituting equation [5-5-19] into equation [5-5-17] gives:

$$I_{SS} = q \cdot \left(a_0^2 N_V w (\frac{\partial u}{\partial x} + \varepsilon q) \frac{3k'_3}{2kT} \right)^{1/2} \qquad [5\text{-}5\text{-}20]$$

Equation [5-5-20] shows that the steady state current increases with the increase of cation vacancy density N_V. As discussed in previous sections, the increase of Al content in the materials will result in an increase in the cation vacancy density for passive films of titanium aluminides. Therefore, the increase of Al content in passive films of titanium aluminides will result in the increase of dissolution rate. This equation can explain our results of potentiostatic experiments in the acidic solutions.

In the alkaline solutions, the dissolution rates of titanium aluminides are very similar to that of Ti and nearly independent of their Al content. This indicates that the mechanism is more complex for dissolution behavior of titanium aluminides in alkaline solutions than that in the acidic solutions.

According to our XPS results, passive films for titanium aluminides formed in NaOH show that Al was depleted from the outmost layer. This Al depleted layer has composition similar to that of titanium. As shown in Figure 5-1-2, the dissolution rate of Al in acidic solutions is two magnitude lower than that in alkaline solutions. Therefore, this Al depleted outmost layer may result from the preferential dissolution of Al from the passive film. The preferential dissolution of Al causes the formation of the Al depleted topmost layer in the film which results in low cation vacancy concentration. According to equation [5-5-20], the low cation vacancy concentration will result in low dissolution rate of the passive film. This provides another barrier for the metal dissolution as illustrated in Figure 5-5-3. Therefore, the similar dissolution rate for titanium aluminides in alkaline solutions is closely related to the formation of the Al depleted topmost layer in the passive film.

Therefore, in the acidic solutions, with the increase of Al content in the passive film, the cation vacancy concentration also increases, which results in the increase of the dissolution rate. In the alkaline solutions, the preferential dissolution of Al from the passive film results in a TiO_2 dominant topmost layer in the passive film. This layer may have cation vacancy density similar to that of Ti and therefore results in a low dissolution rate of the passive film. The compositions in the topmost layer of the passive films formed in

NaOH, are not much affected by their bulk composition. Therefore, all the specimens show anodic current similar to that of Ti in NaOH.

Table 5-3-1. Effect of C_H on the calculated values of slope and flatband potential

C_H	C	S_1	S_2'	V_{fb}' (V)	$\Delta V_{fb}'$(V)	V_{fb} (V)
2	0.25	77	67	-0.045	0.058	0.013
1	0.20	87	69	-0.11	0.15	0.04
0.5	0.18	108	69	-0.32	0.38	0.06
0.2	0.12	181	72	-1.33	1.5	0.17

C: capacitance value selected from the linear region of the plot in Figure 5-3-3

S_1: slope of the plot in Figure 5-3-3

S_2': calculated slope from equation [5-3-27]

V_{fb}': flat band potential directly derived from the Figure 5-3-3

V_{fb}: flatband potential corrected with addition of $\Delta V_{fb}'$

$\Delta V_{fb}'$: shift of flatband potential calculated by equation [5-3-28]

* $\varepsilon_S = 60$, $S_{ideal}=66.5$, $V_{fb} = 0$

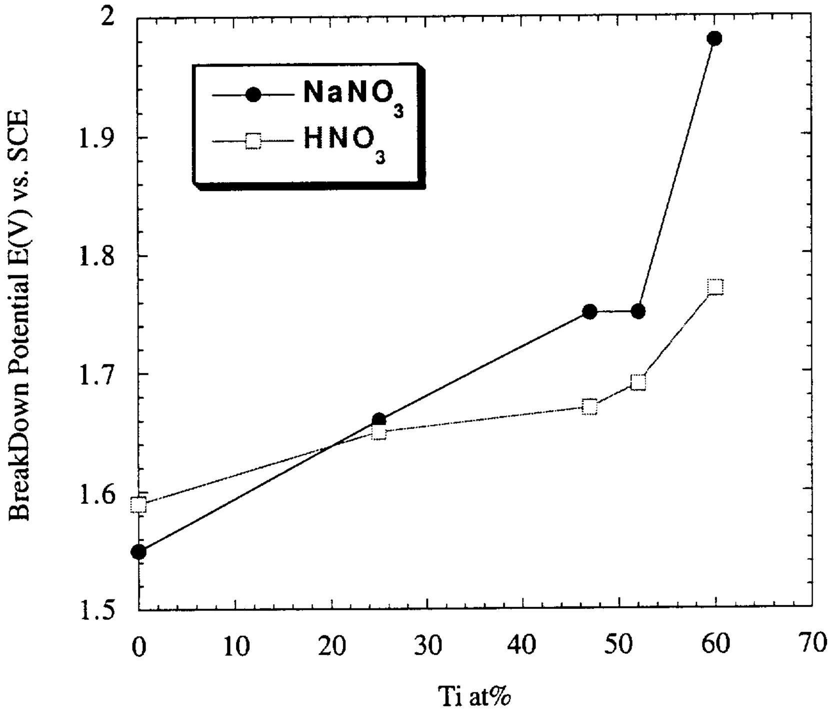

Figure 5-1-1. Passive film breakdown potentials for titanium aluminides in HNO_3 and $NaNO_3$.

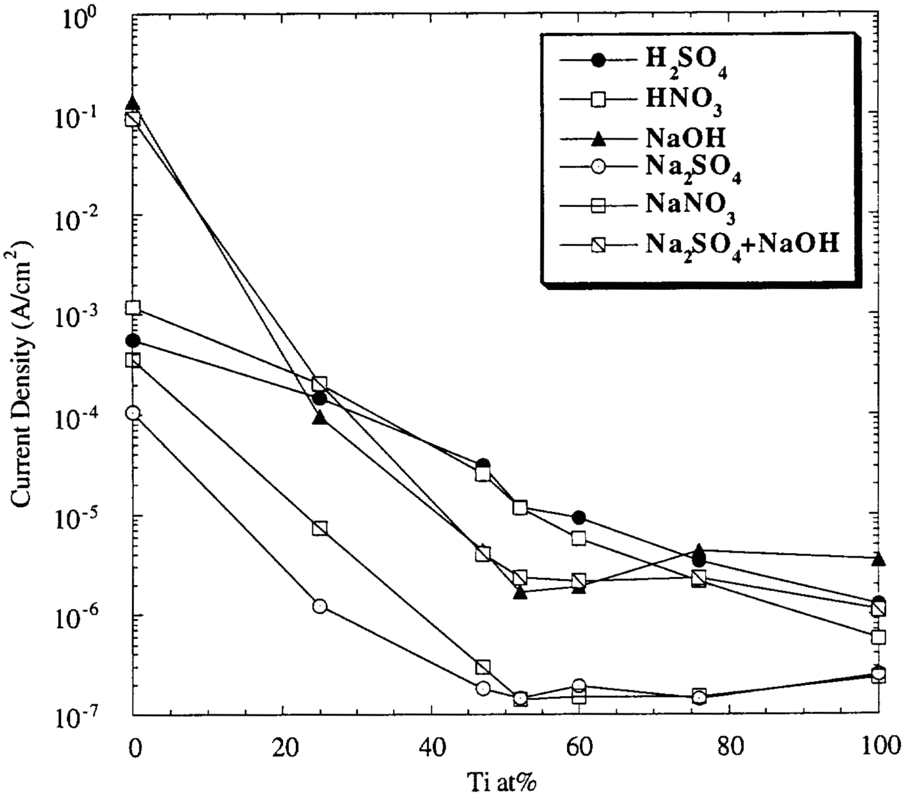

Figure 5-1-2. Current densities at the end of one hour potentiostatic polarization in different solutions.

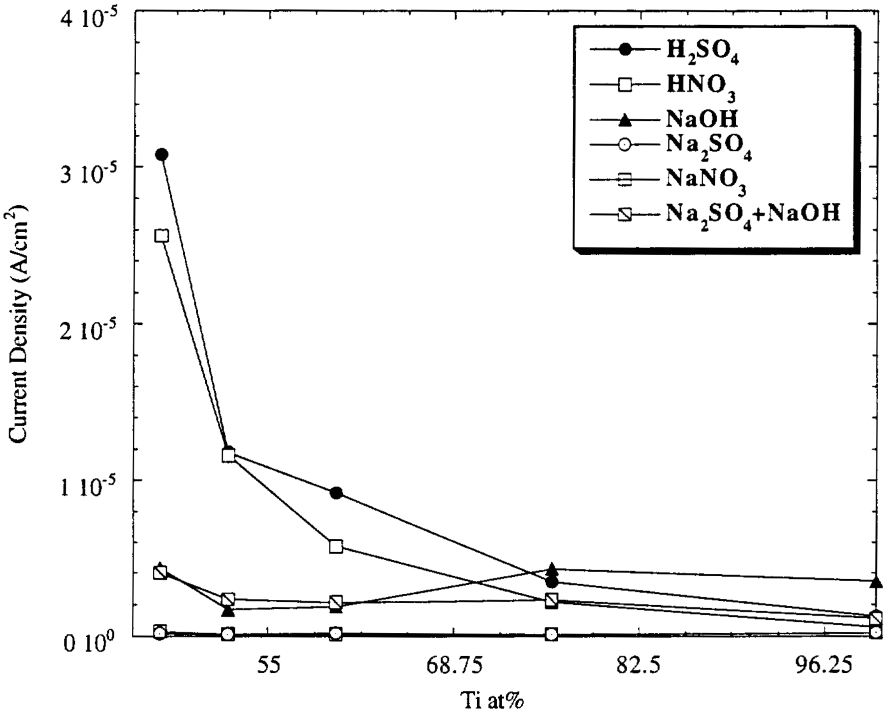

Figure 5-1-3. Current densities at the end of one hour potentiostatic polarization in different solutions for specimens with high Ti concentration.

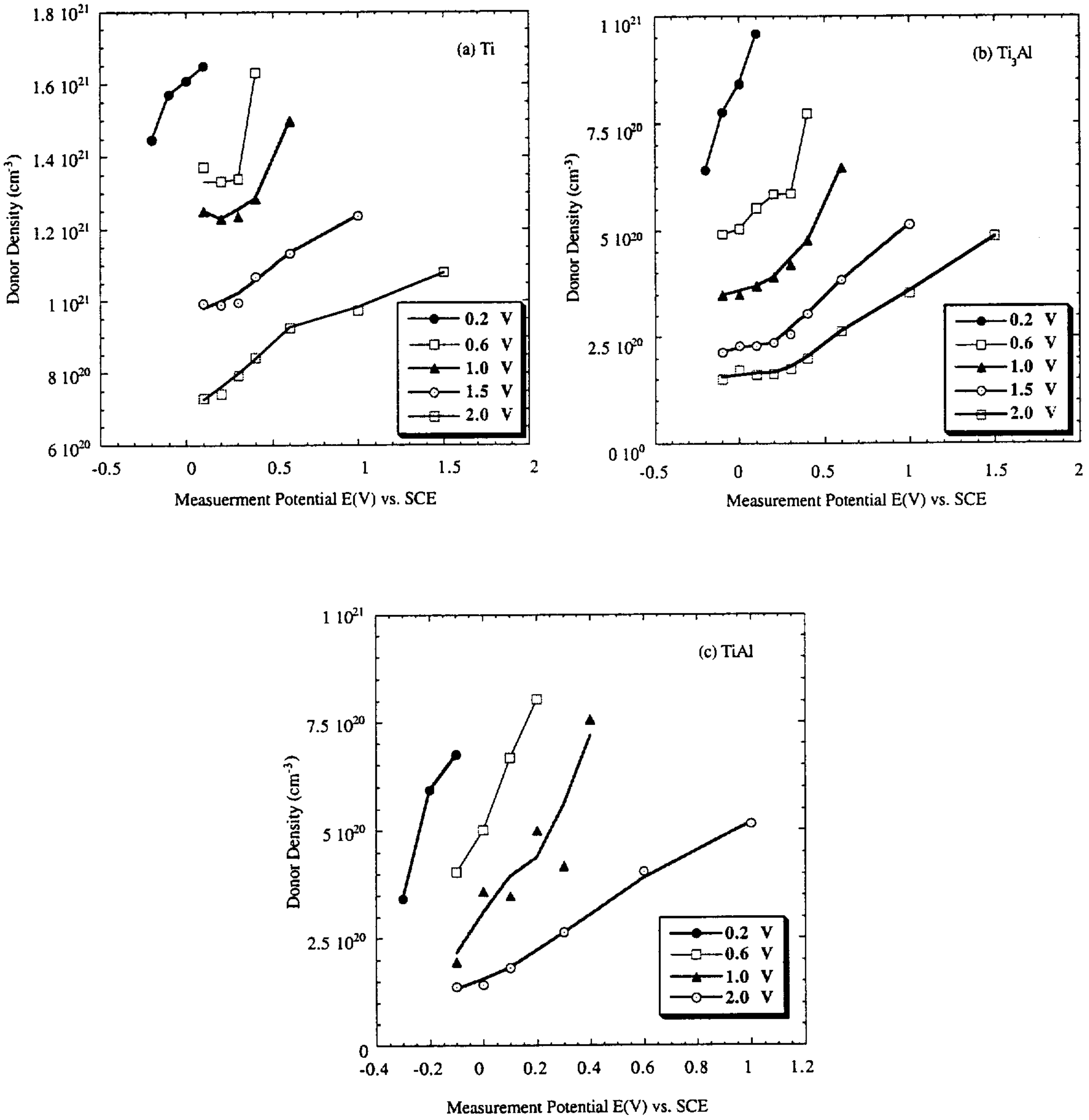

Figure 5-2-1. Doping profiles for passive films formed in H_2SO_4 at different film formation potentials. (a) Ti, (b) Ti_3Al and (c) TiAl

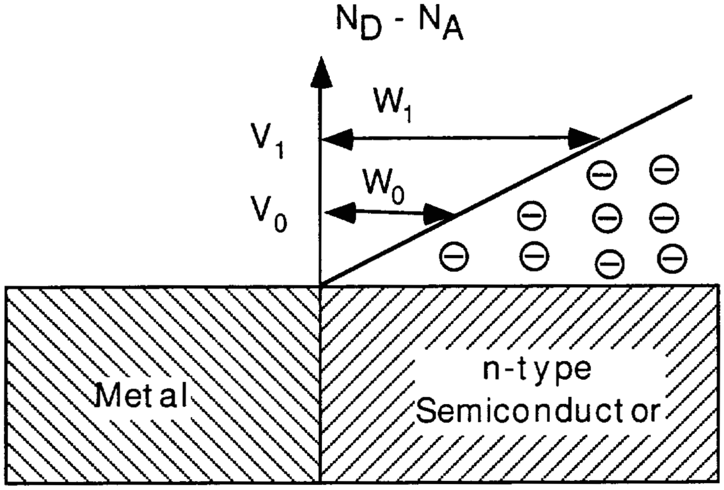

Figure 5-2-2. Relation between the width of the depletion layer and the applied potential where V_0 and V_1 are applied potentials, W_0 and W_1 are the corresponding width of the depletion layer, $V_0 < V_1$, $W_0 < W_1$.

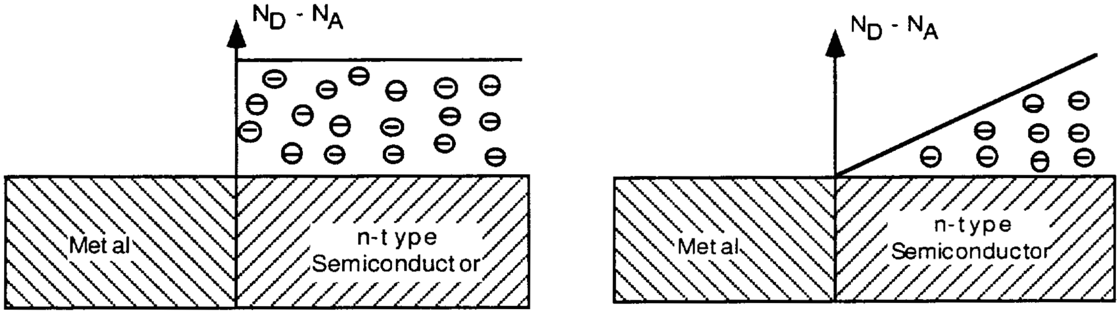

Homogenous Donor Distribution

Linearly Graded Donor Distribution

Figure 5-3-1. Metal and n-type semiconductor contact with homogenous or linearly graded donor distribution.

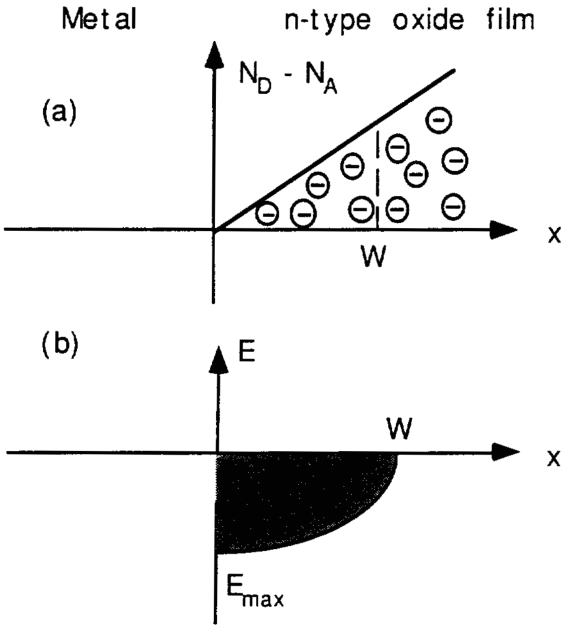

Figure 5-3-2. Linearly graded semiconductor-metal contact.
(a) Space-charge distribution (b) Electric field distribution

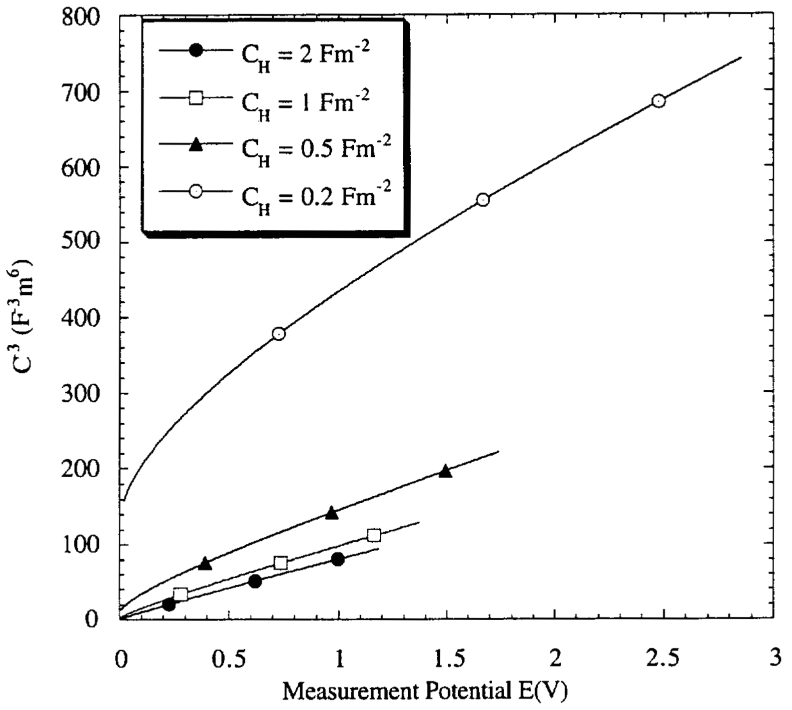

Figure 5-3-3. Effect of C_H on the modified Mott-Schottky plot where $\varepsilon_S = 60$ (TiO_2), $a=10^{36}m^{-3}$, $V_{fb} = 0V$.

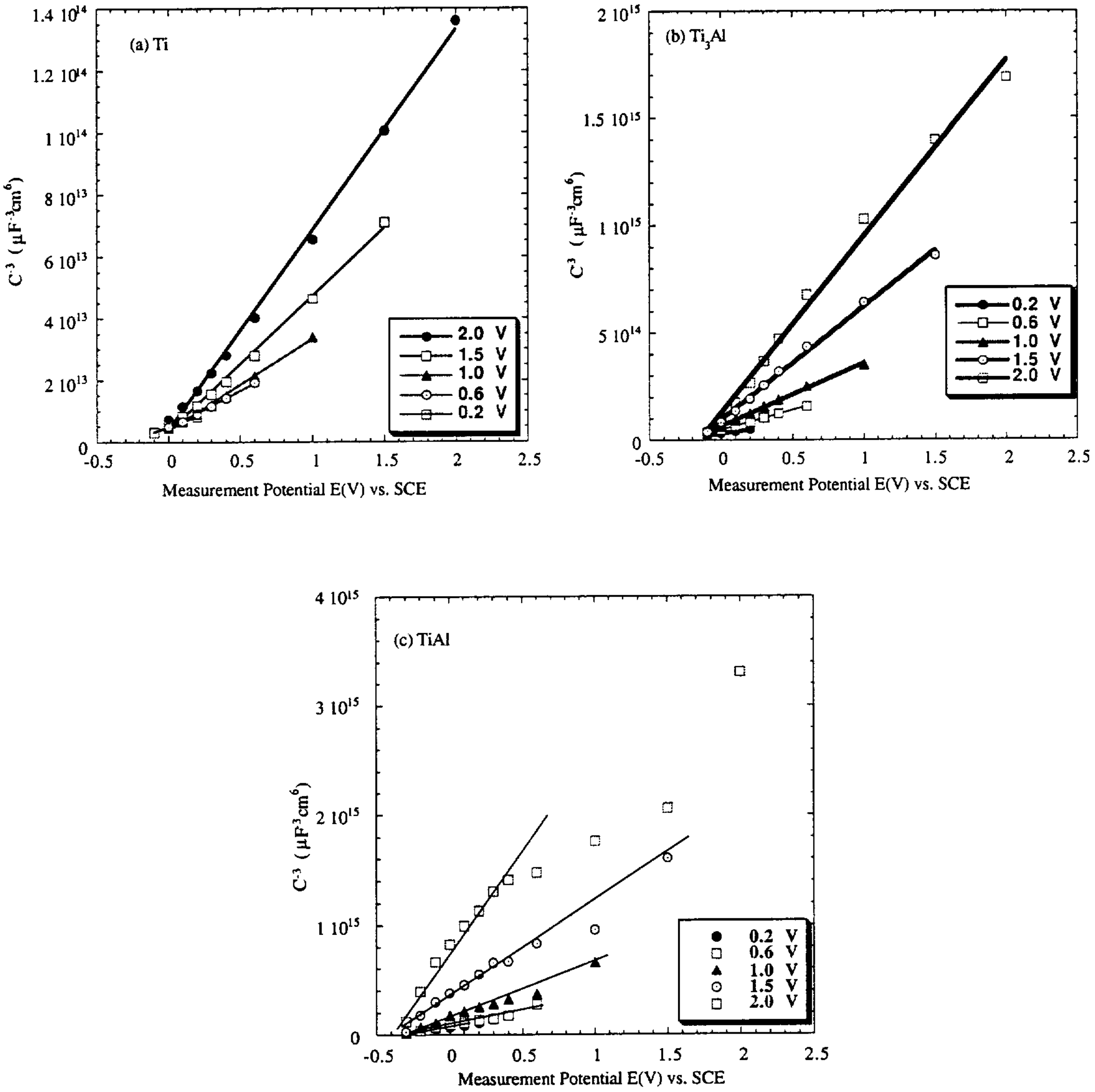

Figure 5-3-4. Modified Mott-Schottky plots for passive films formed in H_2SO_4.
(a) Ti, (b) Ti_3Al, and (c) TiAl

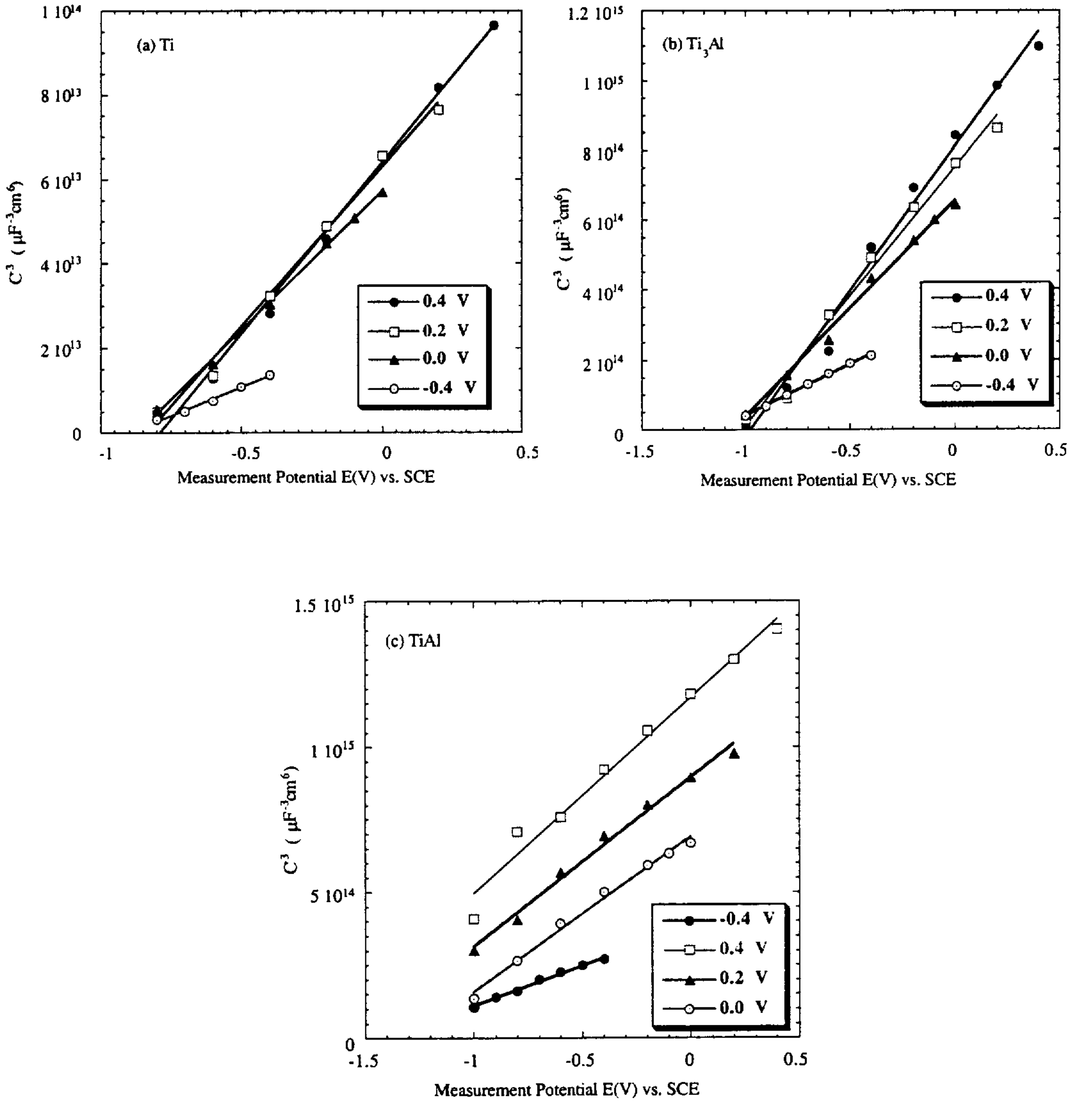

Figure 5-3-5. Modified Mott-Schottky plots for passive films formed in NaOH. (a) Ti, (b) Ti_3Al, and (c) TiAl

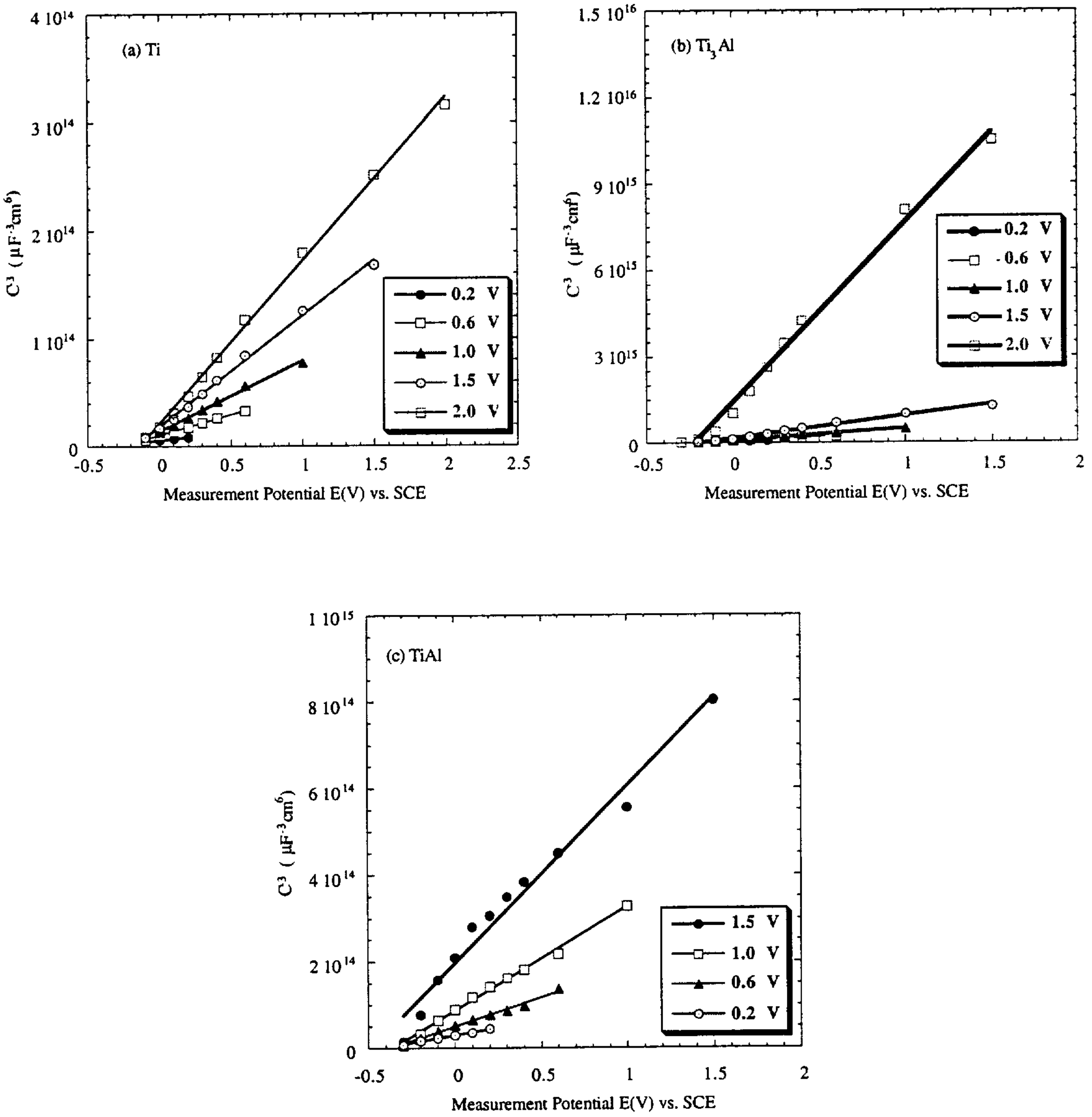

Figure 5-3-6. Modified Mott-Schottky plots for passive films formed in HNO_3.
(a) Ti, (b) Ti_3Al, and (c) TiAl

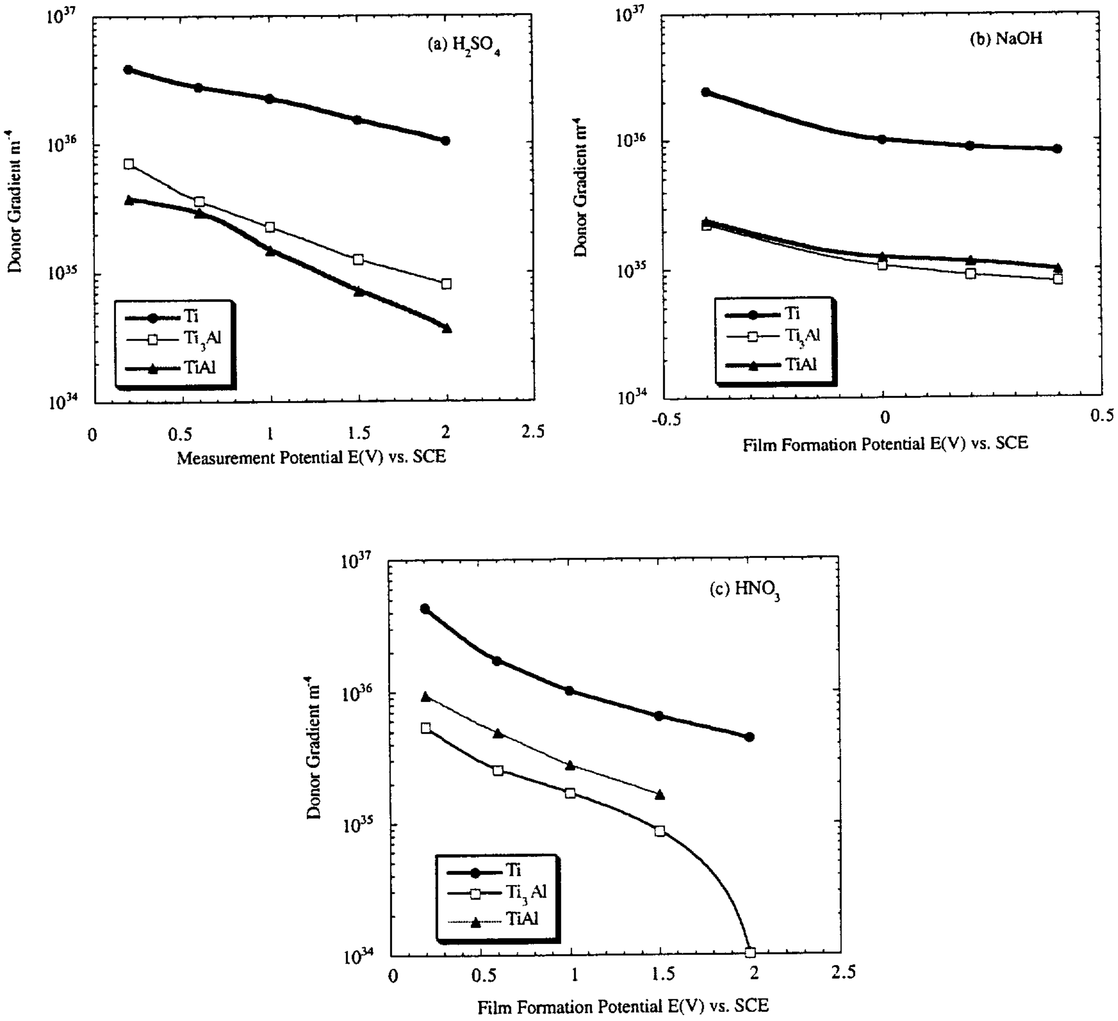

Figure 5-3-7. Donor density gradient for Ti, Ti_3Al and TiAl passive films formed in different solutions. (a) H_2SO_4 (b) NaOH (c) HNO_3

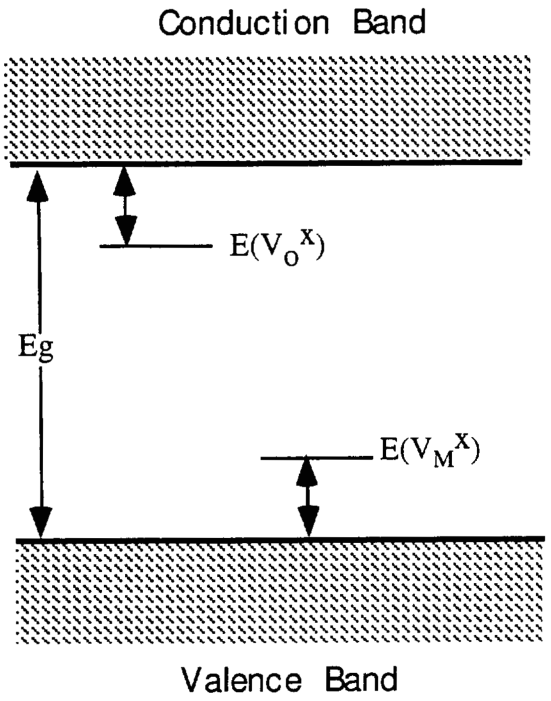

Figure 5-4-1. Energy diagram of a crystal MO containing cation and anion vacancies.

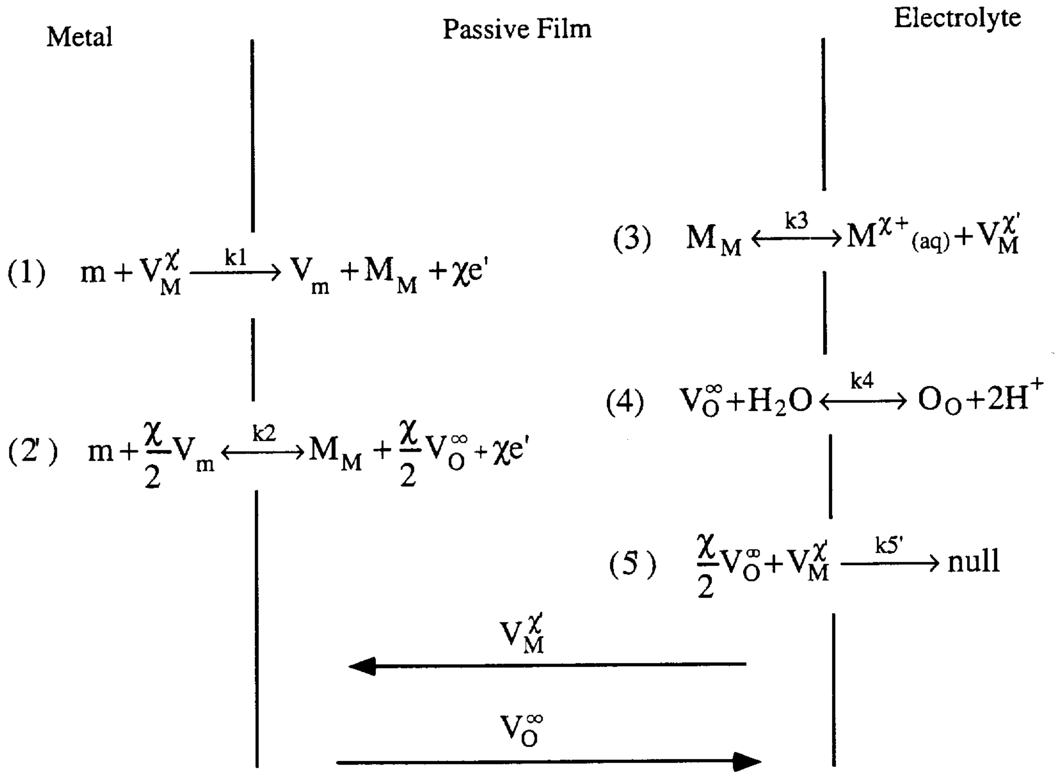

Figure 5-5-1. Modified point defect model for vacancy generation and annihilation reactions inside a passive film.

m = metal atom, M_m = metal cation in cation site, O_O = oxygen anion in anion site

$V_M^{\chi'}$ = cation vacancy, $V_O^{\circ\circ}$ = anion vacancy, V_M = metal vacancy in the metal phase

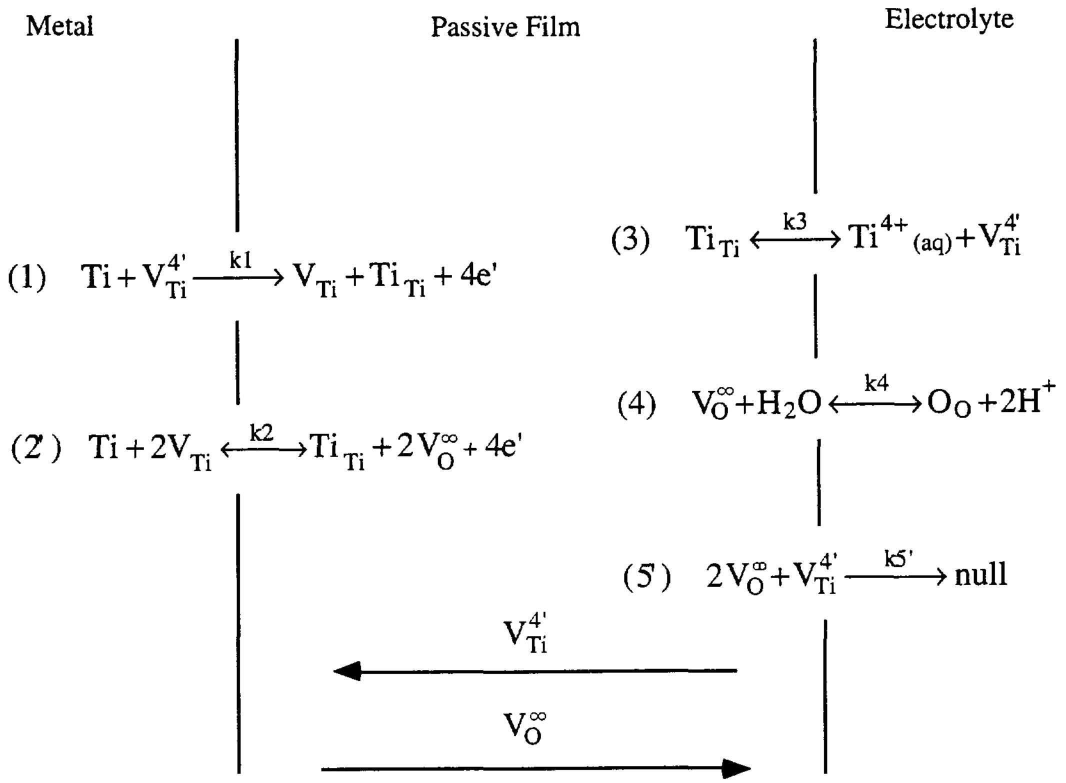

Figure5-5-2. Modified point defect model for vacancy generation and annihilation inside TiO_2 passive film.

Ti = metallic Ti atom, Ti_{Ti} = Ti cation in cation site, O_O = oxygen ion in anion site

$V_{Ti}^{4'}$= Ti^{4+} cation vacancy, $V_O^{\circ\circ}$ = oxygen anion vacancy, V_{Ti} = Ti metal vacancy

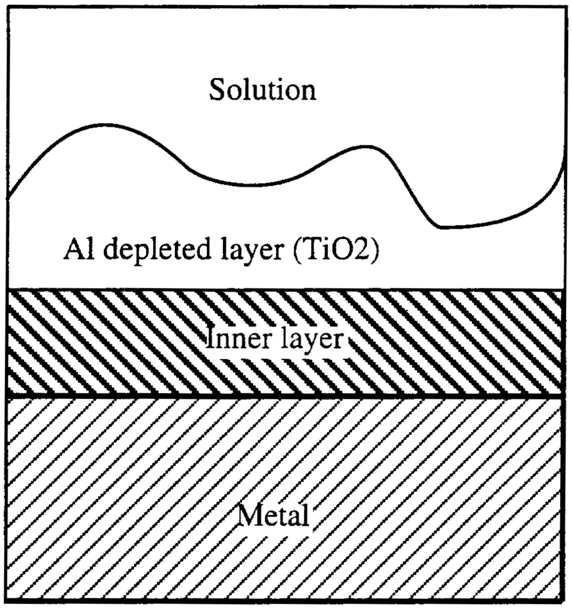

Figure 5-5-3. Double layered film structure for passive film formed in NaOH.

6. CONCLUSIONS

Passivation behavior of Titanium aluminides was studied using electrochemical and surface analysis techniques. In this investigation it is found:

1. In acidic solutions, the steady state current density increases with the increase of Al content. The ratio of Al/Ti in the passive films is similar to that in the bulk materials. In alkaline solutions, the quasi-steady state current density is nearly independent of the Al content. The passive film contains primarily TiO_2 oxide in the outmost layer. In neutral solutions, the dissolution rates is much lower than those in acidic as well as alkaline solutions.
2. Titanium aluminides are susceptible to pitting corrosion in solutions containing NO_3^- ions. The pitting potential increases with decreasing Al content in the materials.
3. Results of Electrochemical Impedance Spectroscopy (EIS) experiments show that passive films of titanium aluminides have n-type semiconductor properties. The donor distribution for titanium aluminides is non-homogenous and a modified Mott-Schottky equation was developed based on a linear gradient distribution.
4. A modified point defect model was developed to explain the dissolution behavior for titanium aluminides in acidic and alkaline solutions. In acidic solutions, the increase of Al content results in higher cation vacancy concentration which causes the increase of dissolution rates. In alkaline solutions, due to the high dissolution rate of Al in alkaline solutions, a TiO_2 outer layer was formed in the passive film. This TiO_2 outer layer results in low dissolution rate for titanium aluminides in alkaline solution.

This study shows that the composition, dissolution rate, and semiconductor properties of a passive film are closely related. The complexity of the passivation phenomenon is associated with both the ion transfer and electron transfer processes inside a passive film. Both transportation processes are closely related to the concentrations as well as the defect species in the passive film. The modified Mott-Schottky relation developed in this study shows that donor distribution inside the thin passive film is not homogenous. Such information is very important to understand the defect distribution inside passive films. The modified point defect model demonstrates how the alloying element may affect the properties of passive film. This model also shows that the composition, dissolution rate, and semiconductor properties of a passive film are closely related to the generation and annihilation of point defects inside passive films.

REFERENCES

1. P. Bartolotta, et al, The Use of Cast Ti-48Al-2Cr-2Nb in Jet Engines, *JOM,* **49**(5), p. 48-50, 1997.

2. Y. W. Kim, Technology Transfer: Gamma Alloys Appear Ready for Aerospace and Automotive Markets, *JOM,* **46**(7), 1994.

3. Y. W. Kim, Ordered Intermetallic Alloys, Part III: Gamma Titanium Aluminides, *JOM*, **46**(7), p. 30-39, 1994.

4. W. Su, M. Ziomek-Moroz, and J. B.S. Covino. Study of Passive Films on Alpha2 and Gamma Titanium Aluminides, in *30th Annual IMS Convention*, Seattle, Washington, in press, 1997.

5. M. Ziomek-Moroz. Passivity and Passivity Breakdown in Intermetallic-Based Alloys, in *Environmental Effects on High Technology Materials*, Zakopane, Poland, p. 249-261, 1997.

6. T. L. Lievestro, Electrochemical machining, in *ASM Handbook*, p. 533-541, ASM International, 1990.

7. B. S. Covino and S. C. Rhoads. Corrosion Behavior of Advanced Intermetallic Materials, in *First International Symposium on Environmental Effects on Advanced Materials*, p. 16-1,16-9, 1991.

8. A. N. Kamkin, A. D. Davydov, and L. A. Fishgoit, The Effects of the Composition of Titanium-Aluminum Alloy and Anodic Oxide Film on the Breakdown Potential in Chloride and Bromide Solutions, *Protection of Metals*, **32**(3), p. 214-216, 1996.

9. Z. Yao and M. Marek, NaCl-induced hot corrosion of a titanium aluminide alloy, *Materials Science and Engineering*, **A 192/193**, p. 994-1000, 1995.

10. H. Saffarian, et al, Corrosion Behavior of Binary Titanium Aluminide Intermetallics, *Corrosion*, **52**(8), p. 626-633, 1996.

11. H. M. Saffarian, et al. Aqueous Corrosion Behavior of Titanium Aluminides, in *Control of Interfaces in Metal and Ceramics Composites*, p. 345-354, 1993.

12. R. De Gryse, et al, On the Interpretation of Mott-Schottky Plots Determined at Semiconductor/Electrolyte Systems, *J. Electrochem. Soc.*, **122**, p. 771-712, 1975.

13. R. W. Schutz and D. E. Thomas, *Corrosion of Titanium and Titanium Alloys*, ASM Handbook, Vol. **13**, ASM International, 1985.

14. H. Froes, C. Suryanarayana, and D. Eliezer, Production, Characteristics, and Commercialization of Titanium Aluminides, *ISIJ International*, **31**(10), p. 1235-1298, 1991.

15. F. H. Froes, C. Suryanarayana, and D. Eliezer, Synthesis, properties and applications of titanium aluminides, *Journal of Materials Science*, **27**, p. 5113-5140, 1992.

16. T. B. Massalski, *Binary Alloy Phase Diagrams*, , Vol. **1**, ASM International, 1990.

17. J. Ding, *Structure-Property Relationships of Advanced High Temperature Materials*, Ph. D. Thesis, Oregon Graduate Institute of Science and Technology, 1995.

18. N. D. Tomashov and P. M. Altovskii, *Corrosion and Protection of Titanium*, 1963.

19. V. V. Andreeva, Behavior and Nature of Thin Oxide Films on Some Metals in Gaseous Media and in Electrolyte Solutions, *Corrosion*, **20**(2), p. 35-46, 1964.

20. R. W. Schutz, J. S. Grauman, and J. A. Hall. Effect of Solid Solution Iron on the Corrosion Behavior of Titanium, in *Titanium Science and Technology*, , p. 2617-2634, 1985.

21. L. C. Covington and R. W. Schutz. Effect of Oxide Films on the Corrosion Resistance of Titanium, in *Corrosion/81*, Toronto, Canada, p. 16, National Assoc. of Corrosion Engineers, 1981.

22. Z. Szklarska-Smialowska and M. Janik-Czachor, Analysis of Electrochemical Methods for the Determination of Characteristic Potentials of Pitting Corrosion, *Corrosion Science*, **11**, p. 901-914, 1971.

23. M. Pourbaix, *Atlas of Electrochemical Equilibria in Aqueous Solutions*, Aluminum, p 221, National Association of Corrosion Engineers, 1974.

24. B. D. Craig, *Fundamental Aspects of Corrosion Films in Corrosion Science*, Plenum Press, 1991.

25. E. H. Hollingsworth and H. Y. Hunsicker, Corrosion of Aluminum and Aluminum Alloys, in *Metals Handbook*, p. 583, American Society for Metals, 1985.

26. P. Janavicius and J. H. Payer, The Dissolution Behavior of Iron Aluminides., in *Environmental Effects on Advanced Materials.*, p. 199-213, The Minerals, Metals & Materials Society, 1991.

27. T. Ohtsuka, J. Guo, and N. Sato, Raman Spectra of the Anodic Oxide Film on Titanium in Acidic Sulfate and Neutral Phosphate Solutions, *J. Electrochem. Soc.*, **133**(12), p. 2473-2476, 1986.

28. L. D. Arsov, C. Kormann, and W. Plieth, In Situ Raman spectra of anodically formed titanium dioxide layers in solutions of H2SO4, KOH, and HNO3, *J. Electrochem. Soc.*, **138**(10), p. 2964-2970, 1991.

29. T. Shibata and Y. C. Zhu, The Effect of Temperature on the Growth of Anodic Oxide Film on Titanium, *Corrosion Science*, **37**(1), p. 133-145, 1995.

30. E. Sergent and Y. Roques, The Role of Water on the Repassivation Behavior of Ti-6Al-4V and Zircaloy-4 alloys in Halide-Containing hydro-organic Solutions, *Corrosion Science*, **36**, p. 653-667, 1994.

31. T. Shibata and Y. C. Zhu, The Effect of Film Formation Conditions on the Structure and Composition of Anodic Oxide Films on Titanium., *Corrosion Science*, **37**(2), p. 253-270, 1995.

32. J. F. McAleer and L. M. Peter, Instability of Anodic Oxide Films On Titanium, *J. Electrochem. Soc.*, **129**(6), p. 1252-1259, 1982.

33. A. R. Prusi and L. D. Arsov, The Growth Kinetics and Optical Properties of Films Formed Under Open Circuit Conditions On a Titanium Surface in Potassium Hydroxide Solutions, *Corrosion Science*, **33**(1), p. 1153-167, 1992.

34. G. O. H. Whillock and G. T. Burstein, The Dissolution and Repassivation of New Titanium Surfaces in Alkaline Methanolic Solution, *J. Electrochem. Soc.*, **136**(5), p. 1320-1327, 1989.

35. T. Ohtsuka, M. Masuda, and N. Sato, Cathodic Reduction of Anodic Oxide Film Formed on Titanium, *J. Electrochem. Soc.*, **134**(10), p. 2406-2410, 1987.

36. D. D. Macdonald, M. Ben-Haim, and J. Pallix, Segregation of Alloying Elements Into Passive Films, *J. Electrochem. Soc.*, **136**(11), p. 3269-3273, 1989.

37. G. D. Davis, et al, Passive Film Structure of Supersaturated Al-Mo Alloys, *J. Electrochem. Soc.*, **138**(11), p. 3194-3199, 1991.

38. D. G. Kolman and J. R. Scully, Electrochemistry And Passivity of a Ti-15Mo-3Nb-3Al Beta-titanium Alloy In Ambient Temperature Aqueous Chloride Solutions, *J. Electrochem. Soc.*, **140**(10), p. 2771-2779, 1993.

39. M. J. Kloppers, F. Bellucci, and R. M. Latanision, Electronic Properties and Defect Structure of Fe and Fe-Cr Passive Films, *Corrosion*, **48**(3), p. 229-238, 1992.

40. N. Sato, An Overview on the Passivity of Metals, *Corrosion Science*, **31**, p. 1-19, 1990.

41. J. S. L. Leach and B. R. Pearson, Crystallization in Anodic Oxide Films, *Corros. Sci.*, **28**(1), p. 43-56, 1988.

42. T. Shibata and Y.-C. Zhu, The Effect of Film Formation Potential on the Stochastic Processes of Pit Generation on Anodized Titanium, *Corrosion Science*, **30**(1), p. 153-166, 1993.

43. N. Casillas, et al, Pitting Corrosion of Titanium, *J. Electrochem. Soc.*, **141**(3), p. 635-643, 1994.

44. D. A. Jones, *Principles and Prevention of Corrosion*, p. 47, Prentice-Hall, Inc., 1996.

45. R. P. Frankenthal, Passivation Of Fe In Borate Buffer Solution, *Electrochimica Acta*, **16**, p. 1845-1857, 1971.

46. H. W. Pickering and R. P. Frankenthal, Mechanism of Localized Corrosion of Fe and Stainless Steel. Pt. 1.--Electrochemical Studies, *J. Electrochem. Soc.*, **119**(10), p. 1297-1304, 1972.

47. M. G. Fontana, *Corrosion Engineering*, p. 556, McGraw-Hill, 1986.

48. M. Keddam, Anodic Dissolution, in *Corrosion Mechanisms in Theory and Practice*, p. 55, Marcel Dekker, 1995.

49. N. Sato and T. Noda, Ion Migration in Anodic Barrier Oxide Films on Fe in Acidic Phosphate Solutions, *Electrochimica Acta*, **22**(8), p. 839-843, 1977.

50. C. Y. Chao, L. F. Lin, and D. D. Macdonald, A Point Defect Model for Anodic Passive Films, *J. Electrochem. Soc.*, **128**(6), p. 1187-1198, 1981.

51. M. Janik-Czachor, Electrochemical and Microscopic Study Of Pitting Corrosion Of Ultra-Pure Fe, *Brit. Corrosion J.*, **6**(2), p. 57-60, 1971.

52. D. D. Macdonald and M. U. Macdonald, Theory of Steady-state Passive Films, *J. Electrochem. Soc.*, **137**(8), p. 2395-2402, 1990.

53. D. D. Macdonald, The Point Defect Model for the Passive State, *J. Electrochem. Soc.*, **139**(12), p. 3434-3449, 1992.

54. D. D. Macdonald, S. R. Biaggio, and H. Song, Steady-State Passive Films, *J. Electrochem. Soc.*, **139**(1), p. 170-177, 1992.

55. D. D. Macdonald, On the Formation of Voids in Anodic Oxide Films on Aluminum, *J. Electrochem. Soc.*, **140**(3), p. L27-L30, 1993.

56. J. S. L. Leach and B. R. Pearson, Crystallization in Anodic Oxide Films, *Corrosion Science*, **28**(1), p. 43-56, 1988.

57. P. Schmuki and S. Virtanen, Experimental Modeling of Passivity, *Electrochemical Society Interface*, **6**(2), p. 38-42, 1997.

58. M. Sakashita and N. Sato, Ion Selectivity of Precipitate Films Affecting Passivation and Corrosion of Metals, *Corrosion*, **35**(8), p. 351-355, 1979.

59. A. Pinkowski, About a Critical Thickness of the Passive Layer on Iron at the Flade Potential, *Werkst. Korros.*, **37**(10), p. 526-531, 1986.

60. B. D. Cahan and C. T. Chen, Questions on the Kinetics of Oxygen Evolution on Oxide-Covered Metals, *J. Electrochem. Soc.*, **129**(4), p. 700-705, 1982.

61. B. D. Cahan and C. T. Chen, The Nature of the Passive Film on Iron. II.--A.C. Impedance Studies, *J. Electrochem. Soc.*, **129**(3), p. 474-480, 1982.

62. B. D. Cahan and C. T. Chen, The Nature of the Passive Film on Iron. III.--The Chemi-Conductor Model and Further Supporting Evidence, *J. Electrochem. Soc.*, **129**(5), p. 921-925, 1982.

63. C. T. Chen and B. D. Cahan, The Nature of the Passive Film on Iron. I.--Automatic Ellipsometric Spectroscopy Studies, *J. Electrochem. Soc.*, **129**(1), p. 17-26, 1982.

64. S. R. Morrison, *Electrochemistry at Semiconductor and Oxidized Metals Electrodes*, Plenum Press, 1980.

65. K. Azumi, T. Ohtsuka, and N. Sato, Mott--Schottky Plot of the Passive Film Formed on Iron in Neutral Borate and Phosphate Solutions, *J. Electrochem. Soc.*, **134**(6), p. 1352-1357, 1987.

66. A. G. G. Allah and A. A. Mazhar, Impedance Behavior of Titanium in Acid, Alkaline, and Neutral Media, *Corrosion*, **46**(4), p. 306-311, 1990.

67. A. G. G. Allah and A. A. Mazhar, Impedance Studies on the Anodic Passivity of Titanium in Aqueous Media of Different pH, *Corrosion*, **45**(5), p. 381-386, 1989.

68. K. Leitner, J. W. Schultze, and U. Stimming, Photoelectrochemical Investigations of Passive Films on Titanium Electrodes, *J. Electrochem. Soc.*, **133**(8), p. 1561-1568, 1986.

69. R. van de Krol, A. Goossens, and J. Schoonman, Mott-Schottky Analysis of Nanometer-Scale Thin-Film Anatase TiO2, *J. Electrochem. Soc.*, **144**(5), p. 1723-1727, 1997.

70. Y.-W. Kim, Intermetallic Alloys Based on Gamma Titanium Aluminide, *JOM*, **41**(7), p. 24-30, 1989.

71. M. Pourbaix, *Atlas of Electrochemical Equilibria in Aqueous Solutions*, Titanium, p 215, National Association of Corrosion Engineers, 1974.

72. D. A. Shirley, High-Resolution X-Ray Photoemission Spectrum of the Valence Bands of Au, *Phys. Rev. B, Solid State*, **5**(12), p. 4709-4714, 1972.

73. N. R. Armstrong and R. Quinn, Auger and X-Ray Photo-Electron Spectroscopic and Electrochemical Characterization of Ti Thin Film Electrodes, *Surf. Sci.*, **67**(2), p. 451-468, 1977.

74. A. Felske, W. A. Badawy, and W. J. Plieth, The Electrochemical and Photoelectrochemical Behavior of Passivated Ti in Nitric Acid solutions, *J. Electrochem. Soc.*, **137**(6), p. 1805-1809, 1990.

75. L. F. Lin, C. Y. Chao, and D. D. Macdonald, A Point Defect Model for Anodic Passive Films(2), *J. Electrochem. Soc.*, **128**(6), p. 1194-1198, 1981.

76. T. Hurlen and S. Hornkjol, Anodic Growth of Passive Films on Titanium, *Electrochimica Acta*, **36**(1), p. 189-195, 1991.

77. E. J. Kelly, Anodic Dissolution of Titanium in Acidic Sulfate Solutions, *J. Electrochem. Soc.*, **123**(1), p. 162, 1976.

78. W. Wilhelmsen and T. Hurlen, Passive Behaviour of Titanium in Alkaline Solution, *Electrochim. Acta*, **32**(1), p. 85-89, 1987.

79. T. Hurlen and W. Wilhelmsen, Passive Behaviour of Titanium, *Electrochimica Acta*, **31**(9), p. 1139-1146, 1986.

80. D. D. Macdonald, Some Advantages and Pitfalls of Electrochemical Impedance Spectroscopy, *J. Electrochem. Soc.*, **46**(3), p. 229-242, 1990.

81. F. Mansfeld, et al, Analysis of EIS Data for Common Corrosion Processes, in *Electrochemical Impedance: Analysis and Interpretation*, p. 37-53, 1993.

82. G. Nogami, Some Aspects of Large Frequency Dispersion of Mott-Schottky Plots in TiO2 Electrodes, *J. Electrochem. Soc.*, **32**(1), p. 76-81, 1985.

83. C. D. Fonseca and M. D. C. Belo, A Characterization of Titanium Passivation Films by In-Situ AC Impedance Measurements and XPS Analysis, *Materials Science Forum (Switzerland)*, **192-194**(1), p. 177-184, 1995.

84. J. Schoonman, K. Vos, and G. Blasse, Donor Densities in TiO2 Photoelectrodes, *J. Electrochem. Soc.*, **128**(5), p. 1154-1157, 1981.

85. W. A. Badawy, Corrosion and Passivation of Titanium in Nitric Acid Solutions as Revealed From Impedance and Photoelectrochemical Measurements, *Indian Journal of Technology*, **29**, p. 235-240, 1991.

86. J. M. Dona and J. Herrero, Dependence of Electro-optical Properties on the Deposition Conditions of Chemical Bath Deposited CdS Thin Films, *J. Electrochem. Soc.*, **144**(11), p. 4091-4098, 1997.

87. R. A. Fredlein and A. J. Bard, Semiconductor Electrodes, *J. Electrochem. Soc.*, **126**(11), p. 1892-1898, 1979.

88. M. Tomkiewicz, The Potential distribution at the TiO2 Aqueous Electrolyte Interface, *J. Electrochem. Soc.*, **126**(9), p. 1505-1510, 1979.

89. J. H. Kennedy and J. Karl W. Frese, Flatband Potentials and Donor Densities of Polycrystalline α-Fe2O3 Determined from Mott-Schottky Plots, *J. Electrochem. Soc.*, **125**(5), p. 723-726, 1978.

90. K. Asami, et al, The Surface Characterization of Titanium and Titanium-Nickel Alloys in Sulfuric Acid, *Corrosion Science*, **35**(1-4), p. 43-49, 1993.

91. J. Chastain, *Handbook of X-ray Photoelectron Spectroscopy*, p. 232, Perkin-Elmer Corp., Physical Electronics Division, Eden Prairie MN, 1992.

92. J. Lausmaa, et al, Multi-Technique Surface Characterization of Oxide Films on Electropolished and Anodically Oxidized Titanium, *Applied Surface Science*, **45**(3), p. 189-200, 1990.

93. D. E. Bullard and D. C. Lynch, Reduction of Titanium Dioxide In a Nonequilibrium Hydrogen Plasma, *Metallurgical and Materials Transactions*, **28B**(6), p. 1069-1080, 1997.

94. S. M. Sze, *Physics of Semiconductor Devices*, John Wiley & Sons, 1981.

95. J. O'M. Bockris and A. K. N. Reddy, Modern Electrochemistry, p. 753-756, Plenum Press, 1970.

96. Z. M. Jarzebski, *Oxide Semiconductors*, p. 98-117, Pergamon Press, 1973.

97. R. A. Swalin, *Thermodynamics of Solids*, Wiley, 1962.

98. Z. M. Jarzebski, *Oxide Semiconductors*, p 105, Pergamon Press, 1973.

99. F. A. Kroger and H. J. Vink, *Solid State Physics*, p. 307, Academic Press, 1956.

100. Z. M. Jarzebski, *Oxide Semiconductors*, p. 98, Pergamon Press, 1973.

101. D. D. Macdonald, E. Sikora, and J. Sikora. The Point Defect Model vs. High Field Model for Describing the Growth of Passive Films, in *Proceeding of the Seventh International Symposium on Oxide Films on Metals and Alloys*, Miami Beach, Fla., p. 139-151, 1994.

102. M. Urquidi-Macdonald and D. D. Macdonald, Theoretical Distribution Functions for the Breakdown of Passive Films, *J. Electrochem. Soc.*, **134**(1), p. 41-46, 1987.

103. P. G. Shewmon, *Diffusion in Solids*, p. 70-105, McGraw-Hill Book Company, 1963.

VITA

The author was born on June 30, 1968, in Beijing, China. He attended Beijing University of Science and Technology in Beijing where he received his Bachelor of Science degree in Materials Physics.

After graduation the author worked as a Software Engineer with Japan Process Development Inc. in Beijing, China from 1991 to 1993, and in Hitachi City, Japan from 1993 to 1994.

He started his graduate study by joining the Department of Materials Science and Engineer at Oregon Graduate Institute of Science and Technology in September 1994 and has finished all the requirement for a Ph.D. degree in materials science by July 1998.